UNIVERSIDAD NACIONAL DEL LITORAL

DOCTORADO EN INGENIERÍA

Desarrollo de dispositivos electroforéticos basados en papel para análisis cuantitativos

Nicolás Franck

FICH
FACULTAD DE INGENIERÍA Y CIENCIAS HÍDRICAS

INTEC
INSTITUTO DE DESARROLLO TECNOLÓGICO PARA LA INDUSTRIA QUÍMICA

CIMEC
CENTRO DE INVESTIGACIÓN EN MÉTODOS COMPUTACIONALES

sinc(i)
INSTITUTO DE INVESTIGACIÓN EN SEÑALES, SISTEMAS E INTELIGENCIA COMPUTACIONAL

Tesis de Doctorado **2025**

UNIVERSIDAD NACIONAL DEL LITORAL

Facultad de Ingeniería y Ciencias Hídricas

Instituto de Desarrollo Tecnológico para la Industria Química

Centro de Investigación en Métodos Computacionales

Instituto de Investigación en Señales, Sistemas e Inteligencia Computacional

DESARROLLO DE DISPOSITIVOS ELECTROFORÉTICOS BASADOS EN PAPEL PARA ANÁLISIS CUANTITATIVOS

Nicolás Franck

Tesis remitida al Comité Académico del Doctorado

como parte de los requisitos para la obtención

del grado de

DOCTOR EN INGENIERÍA

Mención Mecánica Computacional

de la

UNIVERSIDAD NACIONAL DEL LITORAL

2025

UNIVERSIDAD NACIONAL DEL LITORAL

Facultad de Ingeniería y Ciencias Hídricas

Instituto de Desarrollo Tecnológico para la Industria Química

Centro de Investigación en Métodos Computacionales

Instituto de Investigación en Señales, Sistemas e Inteligencia Computacional

DESARROLLO DE DISPOSITIVOS ELECTROFORÉTICOS BASADOS EN PAPEL PARA ANÁLISIS CUANTITATIVOS

Nicolás Franck

Lugar de Trabajo:

CIMEC (UNL–CONICET)

Centro de Investigación en Métodos Computacionales

Facultad de Ingeniería y Ciencias Hídricas

Universidad Nacional del Litoral

Director:

Dr. Pablo Alejandro Kler — CIMEC (UNL–CONICET)

Co-director:

Dr. Raul Urteaga — IFIS (UNL–CONICET)

Jurado Evaluador:

Dr. Pablo Alfredo Caron — (FRH, UTN)

Dr. Leonardo Gagliardi — (UNLP – CONICET)

Dr. Gastón Miño — (IBB, UNER-CONICET)

2025

Certificación

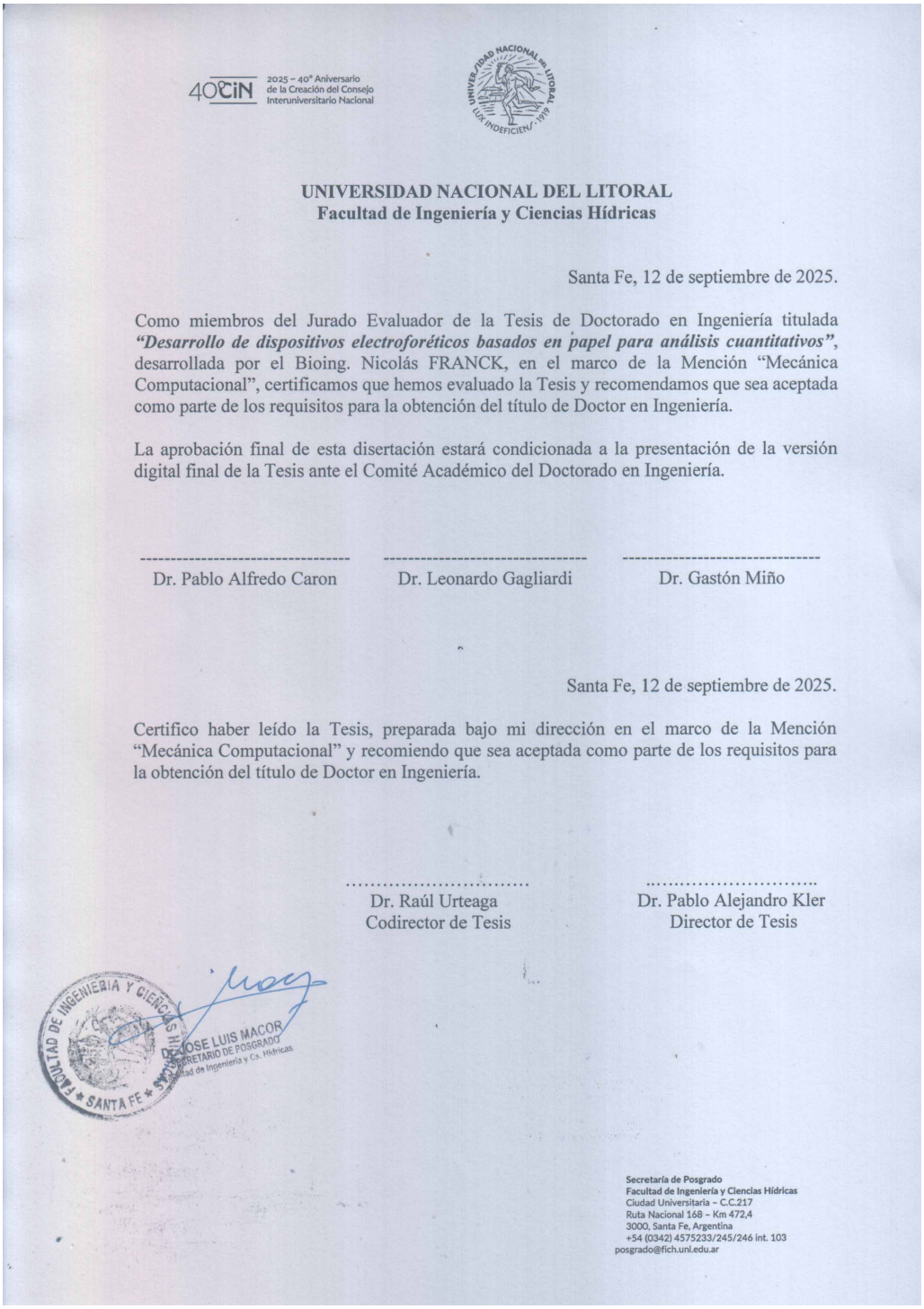

2025 – 40° Aniversario de la Creación del Consejo Interuniversitario Nacional

UNIVERSIDAD NACIONAL DEL LITORAL
Facultad de Ingeniería y Ciencias Hídricas

Santa Fe, 12 de septiembre de 2025.

Como miembros del Jurado Evaluador de la Tesis de Doctorado en Ingeniería titulada ***"Desarrollo de dispositivos electroforéticos basados en papel para análisis cuantitativos"***, desarrollada por el Bioing. Nicolás FRANCK, en el marco de la Mención "Mecánica Computacional", certificamos que hemos evaluado la Tesis y recomendamos que sea aceptada como parte de los requisitos para la obtención del título de Doctor en Ingeniería.

La aprobación final de esta disertación estará condicionada a la presentación de la versión digital final de la Tesis ante el Comité Académico del Doctorado en Ingeniería.

Dr. Pablo Alfredo Caron	Dr. Leonardo Gagliardi	Dr. Gastón Miño

Santa Fe, 12 de septiembre de 2025.

Certifico haber leído la Tesis, preparada bajo mi dirección en el marco de la Mención "Mecánica Computacional" y recomiendo que sea aceptada como parte de los requisitos para la obtención del título de Doctor en Ingeniería.

Dr. Raúl Urteaga Codirector de Tesis	Dr. Pablo Alejandro Kler Director de Tesis

FACULTAD DE INGENIERÍA Y CIENCIAS HÍDRICAS ★ SANTA FE ★ — DR. JOSE LUIS MACOR, SECRETARIO DE POSGRADO, Facultad de Ingeniería y Cs. Hídricas

Secretaría de Posgrado
Facultad de Ingeniería y Ciencias Hídricas
Ciudad Universitaria – C.C.217
Ruta Nacional 168 – Km 472,4
3000, Santa Fe, Argentina
+54 (0342) 4575233/245/246 int. 103
posgrado@fich.unl.edu.ar

Declaración legal del autor

Esta disertación ha sido remitida como parte de los requisitos para la obtención del grado académico de Doctor/a en Ingeniería ante la Universidad Nacional del Litoral y ha sido depositada en Repositorio Institucional de Acceso Abierto -RIAA- de la Facultad de Ingeniería y Ciencias Hídricas para que esté disponible a sus lectores bajo las condiciones estipuladas. Citaciones breves de esta disertación son permitidas sin la necesidad de un permiso especial, en la suposición de que la fuente sea correctamente citada. Solicitudes de permiso para una citación extendida o para la reproducción parcial o total de este manuscrito serán concedidas por el portador legal del derecho de propiedad intelectual de la obra.

Nicolás Franck

Aclaración

La presente tesis se encuentra organizada bajo el formato de Tesis por Compilación, aprobado en la resolución Nº 255/17 (Expte. Nº 888317-17) por el Comité Académico de la Carrera de Doctorado en Ingeniería, Facultad de Ingeniería y Ciencias Hídricas, Universidad Nacional del Litoral. Dicha resolución estipula:

"En el caso de optar por la Tesis por Compilación, ésta consistirá en una descripción técnica de al menos 30 páginas, redactada en español e incluyendo todas las investigaciones abordadas en la tesis. Se deberán incluir las secciones habituales indicadas a continuación en la Sección Contenidos de la Tesis. Los artículos científicos publicados por el autor, en el idioma original de las publicaciones, deberán incluirse en un Anexo con el formato unificado al estilo general de la Tesis indicado en la Sección Formato. El Anexo deberá estar encabezado por una sección donde el tesista detalle para cada una de las publicaciones cuál ha sido su contribución. Esta sección deberá estar avalada por su director de Tesis. El documento central de la Tesis debe incluir referencias explícitas a todas las publicaciones anexadas y presentar una conclusión que muestre la coherencia de dichos trabajos con el hilo conceptual y metodológico de la tesis. Los artículos presentados en los anexos podrán ser artículos publicados, aceptados para publicación (en prensa) o en revisión."

Este trabajo nace de la pasión por encontrar la belleza y el orden donde prima el caos y la entropía, por descubrir los secretos que todo fenómeno esconde, y del gozo profundo del proceso de aprendizaje.

Agradecimientos

Este doctorado ha sido un proceso de constante cambio y aprendizaje. Empecé con ímpetu y muchas ganas de superarme, y hoy, al cerrar esta etapa, valoro el conocimiento y la experiencia acumulados, sabiendo que el aprendizaje nunca se detiene.

No tengo más que palabras de agradecimiento para las instituciones que hicieron posible este recorrido. A mi querida Facultad de Ingeniería de la UNER, por brindarme una formación sólida, tanto académica como humana. Al CONICET, que allá por 2020 confió en mí y me otorgó la beca que permitió materializar este trabajo. Al CIMEC y al IFIS, por abrirme sus puertas y hacerme sentir parte desde el primer día. Y también a la UNL y la UTN, pilares de una educación pública y de calidad que debemos defender y valorar siempre.

También quiero agradecer a Alemania y a las universidades que me recibieron durante mi estancia en el exterior, por darme la oportunidad de aplicar y expandir mis conocimientos en un entorno académico distinto.

A lo largo de este viaje viví experiencias inolvidables, potenciadas por la maravillosa gente que me rodeó. A mis colegas y amigos de la oficina 66 —la mejor del mundo—, por las charlas de cada tarde y el intercambio intelectual. A Pablo y Cuchu, por su apoyo incondicional en cada una de mis ideas, por más descabelladas que fueran. A mi familia, por estar siempre, con palabras de aliento incluso en los momentos difíciles. Y, por supuesto, a todas aquellas personas que, de una u otra forma, se cruzaron en mi camino durante estos años: también a ustedes les agradezco y les dedico este logro.

Este doctorado fue un viaje de transformación constante. Me despido de esta etapa con gratitud por todo lo que me hizo evolucionar, y sigo adelante con entusiasmo, rumbo a nuevos desafíos.

Índice general

Lista de acrónimos VI

Lista de símbolos VIII

Índice de figuras XIII

Índice de tablas XV

1. Introducción **1**

1.1. Objetivos 2

1.1.1. Objetivo general 2

1.1.2. Objetivos específicos 3

1.2. Organización de la tesis 3

1.3. Antecedentes 3

1.3.1. Flujo electroosmótico en medios porosos 4

1.3.2. Modelo multifísico de transporte 6

1.3.3. Movilidad electroforética en medios porosos 8

1.3.4. Detección de glifosato en un e-μPAD 10

2. Metodología **13**

2.1. Flujo electroosmótico en medios porosos 14

2.1.1. Montaje experimental 14

2.1.2. Principio de medición 15

2.1.3. Calibración del sistema 15

2.1.4. Procesamiento de datos 16

2.2. Modelo multifísico de transporte 16

2.2.1. Modelo hidrodinámico 17

2.2.2. Modelo de imbibición capilar 17

2.2.3. Modelo eléctrico 18

2.2.4. Modelo de flujo electroosmótico 19

2.2.5. Diseño Experimental 19

2.3. Movilidad electroforética en medios porosos 21
2.3.1. Modelo matemático 21
2.3.2. Electroforesis capilar 21
2.3.3. Electroforesis en papel 22
2.3.4. Funcionamiento del dispositivo 22
2.3.5. Herramientas computacionales 23
2.4. Detección de glifosato en un e-μPAD 24
2.4.1. Optimización de la detección colorimétrica 24
2.4.2. Análisis por electroforesis capilar acoplada a espectrometría de masas (CE-MS) 25
2.4.3. Herramientas computacionales 25
2.4.4. Electroforesis en papel 25

3. Resultados principales **29**
3.1. Flujo electroosmótico en medios porosos 29
3.1.1. Cálculo de ${\mu_{EOF}}^0$ y ζ_p 29
3.1.2. Desviaciones del modelo lineal 31
3.2. Modelo multifísico de transporte 32
3.2.1. Resultados experimentales 32
3.2.2. Distribución del tamaño de poro 33
3.2.3. Comparación entre diferentes modelos 35
3.3. Movilidad electroforética en medios porosos 36
3.3.1. Prototipo asistido numéricamente 36
3.3.2. Electroforesis en papel 37
3.3.3. Validación del modelo 38
3.4. Detección de glifosato en un e-μPAD 40
3.4.1. Optimización de la detección colorimétrica 40
3.4.2. Optimización numérica del electrolito para isotacoforesis (ITP) 40
3.4.3. Verificación de la separación mediante ITP-ultravioleta (UV) 41
3.4.4. Electroforesis sobre papel 42

4. Conclusiones **47**
4.1. Publicaciones y presentaciones realizadas vinculadas a la tesis 49
4.2. Trabajos a futuro 50

Bibliografía **53**

Anexos **65**

A. Precise electroosmotic flow measurements on paper substrates **67**

A.1. Introduction . . . 70

A.2. Materials and methods . . . 72

A.2.1. Buffer solutions . . . 72

A.2.2. Experimental setup . . . 73

A.2.3. Measuring principle . . . 74

A.2.4. Calibration . . . 75

A.2.5. Data processing . . . 76

A.3. Results and discussion . . . 77

A.3.1. Electroosmotic flow measurements . . . 77

A.3.2. K_{eo} and zeta potential calculations . . . 77

A.3.3. Deviations from linear model . . . 80

A.4. Concluding remarks . . . 82

References . . . 83

B. Multiphysics approach for fluid and charge transport in paper-based microfluidics **85**

B.1. Introduction . . . 88

B.2. Model formulation . . . 91

B.2.1. Hydrodynamic model . . . 92

B.2.2. Capillary imbibition model . . . 92

B.2.3. Electric Model . . . 94

B.2.4. Electroosmotic flow model . . . 94

B.3. Experimental . . . 95

B.3.1. Materials . . . 95

B.3.2. Hydrostatic pressure-driven flow experiments . . . 96

B.3.3. Capillary imbibition experiments . . . 98

B.3.4. Electrical resistance experiments . . . 99

B.4. Results and discussion . . . 99

B.4.1. Experimental results . . . 99

B.4.2. Pore size distribution . . . 101

B.4.3. Comparison between different models . . . 104

B.5. Conclusions . . . 105

References . . . 107

C. A simple method for the assessment of electrophoretic mobility in porous media 113

C.1. Introduction . . . 116

C.2. Mathematical model . . . 118

C.3. Materials and Methods . . . 119

C.3.1. Chemicals . . . 119

C.3.2. Capillary electrophoresis . . . 120

C.3.3. Paper-based electrophoresis . . . 120

C.3.4. Device operation . . . 121

C.3.5. Computational tools . . . 122

C.4. Results and discussion . . . 123

C.4.1. Numerically assisted prototype design . . . 123

C.4.2. Paper-based electrophoresis . . . 125

C.4.3. Model validation . . . 127

C.5. Conclusions . . . 129

References . . . 130

D. Paper-based isotachophoretic preconcentration technique for low-cost determination of glyphosate 135

D.1. Introduction . . . 138

D.2. Materials and Methods . . . 140

D.2.1. Chemicals . . . 140

D.2.2. Optimization of the colorimetric detection . . . 140

D.2.3. CE-MS analysis . . . 141

D.2.4. Computational Tools . . . 142

D.2.5. Paper-based electrophoresis . . . 142

D.3. Results and discussion . . . 144

D.3.1. Optimization of the colorimetric detection . . . 144

D.3.2. Numerical electrolyte optimization for ITP . . . 146

D.3.3. Verification of the separation by ITP-UV analysis . . . 149

D.3.4. Paper-based electrophoresis . . . 150

D.4. Conclusions . . . 154

References . . . 156

Lista de acrónimos

[GLP] Cu^{2+}-GlyP

[PV] Cu^{2+}-PV

µPADs dispositivos analíticos microfluídicos basados en papel

e-µPADs dispositivos analíticos microfluídicos electroforéticos basados en papel

BGE electrolito de fondo

CE electroforesis capilar

CE-MS electroforesis capilar acoplada a espectrometría de masas

CI contraión

EOF flujo electroosmótico

GlyP glifosato

ITP isotacoforesis

LC-MS cromatografía líquida acoplada a espectrometría de masas

LE electrolito líder

LED diodo emisor de luz

LOD límite de detección

pCE electroforesis capilar en papel

PDF función de densidad de probabilidad

PV violeta de pirocatecol

PVP polivinilpirrolidona

RGB rojo-verde-azul

SIM monitoreo de iones seleccionados

TE electrolito terminal

UV ultravioleta

Lista de símbolos

Símbolo	Descripción
ϕ	porosidad
τ	tortuosidad
K	permeabilidad
r_{eff}	radio efectivo de poro
C	factor de constricción
N_p	número de tubos paralelos con constricciones
$< R^n >$	momento estadistico de orden n
$R(x)$	radio del tubo en función de la distancia
R_H	radio hidráulico equivalente
η	viscosidad dinámica
ρ_m	densidad
γ	tensión superficial
θ	ángulo de contacto
s	coeficiente de dispersión
D	coeficiente de Washburn
L_l	posición del frente de fluido en imbibición capilar
t_{fill}	tiempo de llenado capilar
R_C	radio capilar equivalente
Q_h	caudal de un poro
Q_H	caudal total
ϵ	permitividad eléctrica
ρ_e	resistividad eléctrica
σ_p	conductividad eléctrica del papel
Ω_p	resistencia eléctrica del papel
$\Delta\Phi$	diferencia de potencial eléctrico

Símbolo	**Descripción**
E	campo eléctrico
I	fuerza iónica
F	constante de Faraday
ζ	potencial zeta
ζ_p	potencial zeta asociado al papel
μ_{EOF}	movilidad electroosmótica
u_{EOF}	velocidad electroosmótica
Q_{eof}	caudal en un poro debido al EOF
Q_{EOF}	caudal total debido al EOF
μ_e	movilidad electroforética en flujo libre
μ_p	movilidad electroforética en papel
μ_p^{eff}	movilidad electroforética efectiva en papel
R_f	factor de retardo
z_j	valencia del ión j
q^j	carga del ión j
C^j	concentración del ión j
r_s^j	radio hidrodinámico del ión j
L	longitud
x	distancia
t	tiempo
A	sección transversal
w	ancho del papel
h	espesor del papel
m	masa
g	aceleración gravitatoria
ΔP	diferencia de presión
L_{cm}	distancia entre centros de masas de reservorios
R_s	lectura de fuerza de la balanza
d_s	distancia entre punto de apoyo fijo y balanza
h'	coeficiente de transferencia de calor convectivo
α	coeficiente de absorción óptica

Índice de figuras

2.1. Montaje experimental para la medición del flujo electroosmótico (EOF) en papel. 14

2.2. Esquema simplificado de un tubo con constricción. 16

2.3. Esquemas experimentales: flujo hidrostático, imbibición capilar y conducción eléctrica. 20

2.4. Dispositivo de electroforesis en papel para medición de movilidades electroforéticas. 22

2.5. Dispositivo e-µPAD para preconcentrar y detectar glifosato (GlyP). 26

3.1. Valores de $\zeta_p(pH)$ para distintos sustratos 30

3.2. Funciones de densidad de probabilidad (PDFs) utilizadas en el modelado y comparación con datos experimentales. 33

3.3. Mapa de contorno de una función de mérito M, usando una distribución log-normal para distintos sustratos. 34

3.4. Validación del diseño: comparación entre experimentos y simulaciones. 37

3.5. Electroforesis de Tartrazina en papel, con resultados experimentales y numéricos. 38

3.6. Validación experimental del modelo de movilidades electroforéticas en sustratos porosos. 39

3.7. Simulaciones numéricas para optimizar combinaciones de electrolitos en isotacoforesis (ITP) en papel. 41

3.8. Resultados de detección de GlyP en un e-µPAD mediante ITP y analisis colorimétrico. 43

A.1. Experimental setup used to measure EOF on paper substrates. A scale and a fixed support holds the paper strip. Minus (black) and plus (red) signs indicate a possible configuration for applying electric potential at reservoirs R_1 and R_2, respectively, generating EOF in the direction indicated by the blue arrow. This direction is alternated over the experiments as it is described in section A.2.5. 74

A.2. Scale lecture (A), and electrical resistance (B) as function of time for Tris-Acetic, $pH = 4.78$, $\Delta\Phi = \pm$ 300 [V] and $\Delta t = 50s$, for Whatman #1 . The linear fit for averaged mass signal is shown in the inset. 77

A.3. Measured electroosmotic velocity (A) and electroosmotic mobility (B) for different electric potentials using buffer solutions with variable pH in Whatman #1. Data fit corresponds to eq (A.11), where K_{eo} is modeled using the non-linear model described in section A.3.3.2.Uncertainty values represent the 95 % confidence intervals on the mean using a Student-t distribution. 78

A.4. Zeta potential values for different substrates 79

B.1. Simplified scheme of the proposed configuration for a single constricted tube. The structure randomly repeats N_p times, without interconnections between neighbor tubes. 91

B.2. Experimental setups of three different measurements: hydrostatic pressure-driven flow (a, b), capillary-driven flow (c), and electric current through the saturated paper (d). 96

B.3. Calibration process (blue line), determining ΔM^A and ΔM^B variations when known volume droplets are placed in reservoirs A and B respectively. This procedure can be used to obtain amplification factors of the system. Stabilized region (black dots) can be used to measure the flow rate through the paper strip. 98

B.4. Fluid front position as a function of square root of time, for the capillary filling of Whatman #1 and Munktell 00A papers along the machine direction. Different slopes indicate typical variations of R_C and D values obtained in identical paper strips (Eqs. (B.8) and (B.9), respectively). 100

B.5. Calculated free flow conductance as a function of the electric conductance in Whatman #1 substrate. Constriction factor (C) can be obtained from the slope of the linear fit, according to Eq. (B.10). 101

B.6. PDFs explored in modeling: (a) plots of probability densities as a function of radius, (b) schematic representations of pore shapes and characteristic radii, (c) performance of each PDF to describe experimental data from two different substrates, as characterized by the χ^2 test. 102

B.7. Contour map values of M using the log-normal distribution for Whatman #1 (a) and Munktell 00A (b). Solid lines indicate the values for which the parameter combination of PDF reproduces the experimental results of R_H (orange line), R_C (red line), and C (green line). The colored (blue) region corresponds to $M < 3.84$, which represents the 95% confidence region for the predicted parameters. The insets on the left show the optimal log-normal PDF that produce the minimum value of M. 103

C.1. Paper-based electrophoretic device. The device geometry defines three regions: input, detection, and output. Initially, the dye is introduced through the input zone and is conducted towards the pumping region while the buffer is incorporated on both sides of the detection zone. Then, an inversion of the flow is induced in the input region, which allows the generation of a thin line of dye in the detection region. Finally, high voltage is applied between the ends of the detection region where electrophoresis occurs. The lamination region prevents evaporation during experiments. 121

C.2. Stages of validation of the proposed design. Experimental (A) vs numerical (C) results of the injection stage. In the focusing stage, we also compare the laboratory prototype (B) vs the simulated results (D). 124

C.3. Experimental and numerical results for the electrophoretic run of Tartrazine. a) Device operating at $t = 300$ s; b) Processed data curves for $t = 0$ s (blue) and $t = 300$ s (yellow). Marked points denote the spatial position, determined with the H-Cut method. c) 2D reconstruction of the processed information (position vs. time). The dashed line indicates the time when the image in a) was taken. d) Numerical counterpart of c). 126

C.4. Paper-based chromatography of multiple dyes a) Screenshot of the chromatography experiment for selected dyes at t=180 s and pH=5.5. 1-2 are control strips, filled with buffer. 3-5 Tartrazine, 6-7 Brillant Blue, 8-9 Methyl Orange, 10-11 Fast Green, and 12-13 Red Ponceau. b) Linear fit of Tartrazine and buffer front positions. The slope of this line is the retardation factor R_f. 127

C.5. Experimental validation of the electrophoretic mobilities model in porous substrates (eq. (C.3)). Open channel and paper mobilities were measured for different dyes at two pH values. Squares correspond to values measured at pH=5.5 and circles to pH=9.0. The dashed line is the least-squares linear fit to all the data with a single free parameter. 128

D.1. **(a)** Schematic of the low-cost e-µPAD device, featuring a 3D-printed housing with platinum electrodes and nitrocellulose strips bridging the anode and cathode reservoirs. **(b)** Configuration after filling reservoirs and before starting electrophoretic migration. **(c)** Glyphosate preconcentration and color change upon applying an electric field for some minutes. 144

D.2. Colorimetric GLY analysis in solution: **(a)** UV/Vis spectra of PV (30 µM) in the presence of two equivalents Cu^{2+} at pH 6.5 (aqueous MES buffer) with increasing concentration of GLY **(b)** absorbance at 625 nm in MES buffer at pH 6.5 depending on the GLY concentration. 145

D.3. Investigation of solid supports after applying solutions of [PV] complex and GLY. **(a)** Cellulose filter paper did not show a visible color change at high GLY concentrations. **(b)** Nitrocellulose shows a color change but suffers from the coffee ring effect. **(c)** The yellow color of RP-18 W TLC plates after the addition of [PV] indicates the decomposition of [PV] complexes. 146

D.4. Results of numerical simulations for optimizing electrolyte combinations in paper-based ITP. **(a)** Glyphosate sample and electrolyte arrangement (Combination 3 in Table D.1) at 900 s for counter-ions TRIS and ε-aminocaproic acid and TE HEPES. **(b)** Preconcentration factors for different combinations of counter-ions and terminating electrolytes (see Table D.1) depending on the time used for preconcentration. **(c)** Matrix effects with glycine, oxalic and citric acid. HCl in the LE was replaced by 26 mM methylsulfonic acid. 148

D.5. ITP-UV measurement of [PV] (596 nm) and free PV (444 nm) in a commercial CE instrument. Measurements were conducted in a capillary with 50 µm inner diameter at a separation voltage of −10 kV and 40 mbar with a LE consisting of 26 mM ε-aminocaproic acid, 26 mM HCl, 26.3 mM TRIS and 175 µM [PV]. The TE consisted of 2.5 mM HEPES, 5 mM ε-aminocaproic acid and 1 and 2 µM GLY. 149

D.6. Initial setup and results of paper-based capillary electrophoresis (pCE) using MES buffer (pH 6.5) and PV complex for GLY detection. **(a)** Configuration of the nitrocellulose strip with [PV], BGE, and GLY solutions before voltage application. **(b)** Experiment photograph at t=8 min upon electric field application, with GLY having reached the [PV] band **(c)** Absorbance changes indicating GLY concentration with a detection range from 100 µM to 400 µM. 150

D.7. Results of GLY detection with an e-µPAD by ITP technique with colorimetric detection. **(a)** Initial and 15-minute photographs with the analysis area marked in red. **(b)** Time-space matrix showing the system's dynamics. The dotted line contains information from the vertically averaged photograph (a), at t=15 min **(c)** ΔABS values integrated along the spatial coordinate, for each channel over time. **(d)** Calibration curve for multiple GLY concentrations (1, 2, 5 and 25 µM) of integrated absorption difference index (Ψ). 152

D.8. Results of the validation of the preconcentration: **(a)** Calibration of the extraction solution with an efficiency of $\sim$ 50% **(b)** Nitrocellulose zones analyzed by CE-MS with a preconcentration factor of 180 for GLY in paper-based ITP. 154

Índice de tablas

3.1. Valores de potencial zeta en papel y movilidades electroosmóticas obtenidas para distintas soluciones buffer y tipos de sustrato. 30
3.2. Parámetros para cada modelo físico y sus radios estadísticos correspondientes. . . 35
3.3. Movilidades electroforéticas en canal abierto y sustratos de papel. Factor de retardo de distintos colorantes a dos valores de pH. 39

A.1. ζ_p potentials and K_{eo0} obtained for different buffer solutions and types of substrates used. Uncertainty values were calculated by using 95 % confidence bounds in fit process by using eq. A.11 78

B.1. Parameters for single-physics models related to different radii statics 105

C.1. Electrophoretic mobilities, in open channel and paper substrates, and retention factor of different dyes at two pH values. 129

D.1. Electrolyte combinations used in numerical simulations, displaying the concentrations, pH values, and preconcentration factors (C/C_i), calculated as the ratio between GLY concentration at 900 s (C) and the initial concentration (C_i). 147

Resumen

Los dispositivos analíticos microfluídicos electroforéticos basados en papel (e-μPADs) constituyen una plataforma emergente para el análisis cuantitativo de especies iónicas, combinando bajo costo, portabilidad y la posibilidad de operar con volúmenes mínimos de muestra, entre otras ventajas. La implementación en medios porosos como el papel presenta desafíos particulares, relacionados con la modelización de la heterogeneidad y anisotropía del sustrato, el transporte de especies y la variabilidad experimental asociada.

Esta tesis aborda el diseño y caracterización de este tipo de sistemas mediante un enfoque integrado de modelado computacional y validación experimental.

Se desarrollaron técnicas experimentales innovadoras para caracterizar fenómenos clave como el flujo electroosmótico (EOF), cuya comprensión fue fundamental para el desarrollo de e-μPADs. Mediante un enfoque de tubos constrictos, se describieron de forma precisa los principales mecanismos de transporte involucrados en estos dispositivos: conducción eléctrica, flujo electroosmótico e hidrodinámico e imbibición capilar.

Este marco teórico-experimental permitió avanzar hacia el diseño de plataformas orientadas tanto a la caracterización de propiedades electroforéticas de especies cargadas como a la detección de analitos de interés. En particular, se propuso un método sencillo y reproducible para estimar la movilidad electroforética de colorantes en condiciones de operación reales. Asimismo, se desarrolló un dispositivo para la detección de glifosato en muestras de aguas residuales, basado en una técnica de preconcentración isotacoforética. Ambos sistemas fueron concebidos y optimizados mediante simulaciones numéricas, las cuales guiaron el diseño experimental y permitieron mejorar su desempeño. Estas aplicaciones ilustran el potencial del diseño asistido por modelos computacionales como herramienta clave para el desarrollo racional de tecnologías analíticas portátiles, sensibles y de bajo costo.

Los modelos, dispositivos y técnicas experimentales desarrollados constituyen un aporte original significativo a la comunidad científico-tecnológica dedicada a esta temática, lo cual se ve reflejado en las publicaciones con referato que compila esta tesis.

Abstract

Electrophoretic microfluidic paper-based analytical devices (e-μPADs) constitute an emerging platform for the quantitative analysis of ionic species, combining low cost, portability, and the capability to operate with minimal sample volumes, among other advantages. Implementation in porous media such as paper presents particular challenges related to modeling the heterogeneity and anisotropy of the substrate, species transport, and associated experimental variability.

This thesis addresses the design and characterization of these systems through an integrated approach combining computational modeling and experimental validation.

Innovative experimental techniques were developed to characterize key phenomena such as electroosmotic flow, whose understanding was fundamental to developing e-μPADs. Using a constricted tube approach, the main transport mechanisms involved in these devices were precisely described: electric conductivity electroosmotic and hydrodynamic flows, and capillary imbibition.

This theoretical-experimental framework enabled progress towards the design of platforms aimed at both the characterization of electrophoretic properties of charged species and the detection of analytes of interest. In particular, a simple and reproducible method was proposed to estimate the electrophoretic mobility of dyes under realistic operating conditions. Furthermore, a device was developed for detecting glyphosate in wastewater samples based on an isotachophoretic preconcentration technique. Both systems were conceived and optimized through numerical simulations that guided the experimental design and improved performance. These applications illustrate the potential of simulation-assisted design as a key tool for rationally developing portable, sensitive, and low-cost analytical technologies.

The models, devices, and experimental techniques developed constitute a significant original contribution to the scientific and technological community dedicated to this field, as reflected in the peer-reviewed publications compiled in this thesis.

Capítulo 1

Introducción

La microfluídica es una disciplina que estudia y desarrolla tecnologías para controlar y manipular pequeñas cantidades de fluidos, generalmente en volúmenes del orden de los microlitros, dentro de dispositivos fabricados artificialmente. Dado que aborda tanto cuestiones teóricas como aplicaciones prácticas de varias ramas de la ciencia, se trata de un campo intrínsecamente multidisciplinario. En los últimos años, los dispositivos analíticos microfluídicos basados en papel (µPADs) han emergido como una alternativa versátil y de bajo costo para el desarrollo de sistemas de diagnóstico y monitoreo en el punto de aplicación. Estos dispositivos explotan las propiedades capilares del papel como medio poroso para transportar fluidos sin la necesidad de bombas o equipos auxiliares, lo que los convierte en plataformas altamente accesibles y compatibles con criterios establecidos por la Organización Mundial de la Salud [Su et al., 2015].

En este contexto, la integración de técnicas electroforéticas ha dado lugar a una subcategoría conocida como e-µPADs, que permiten realizar separaciones de analitos, asi como su concentración y detección con mayor sensibilidad y especificidad que los µPAD normalmente utilizados. Las aplicaciones de los µPADs y e-µPADs son múltiples. Abarcan el ámbito clínico para el diagnóstico de enfermedades infecciosas, anemia y detección de variantes de hemoglobina, detección de glucosa y monitoreo de biomarcadores tumorales, siendo especialmente útiles en regiones con recursos limitados debido a su bajo costo y facilidad de uso [Modha et al., 2021, An et al., 2021]. También se han implementado en el análisis de alimentos para la detección de adulterantes y contaminantes, así como en el monitoreo ambiental, permitiendo identificar metales pesados, pesticidas y otros compuestos tóxicos [Modha et al., 2021, Salentijn et al., 2018, Tesfaye and Hussen, 2022].

La implementación de procesos electroforéticos en medios porosos heterogéneos como el papel presenta desafíos fundamentales. A diferencia de los microcanales convencionales, donde las condiciones geométricas y fisicoquímicas son bien controladas, los sustratos porosos exhiben anisotropía, dispersión de los parámetros descriptivos, y efectos de interacción entre los analitos y la

matriz; que afectan de manera significativa tanto la movilidad electroforética como la difusión de las especies. A esto se suma la dificultad experimental de cuantificar parámetros clave, así como la necesidad de adaptar modelos de transporte de masa y carga para sistemas multifásicos complejos [Schaumburg et al., 2020b,a].

Desde el punto de vista computacional, la simulación de procesos electroforéticos en sustratos porosos representa un desafío significativo debido a la necesidad de capturar la interacción entre múltiples fenómenos de transporte (advección, difusión, migración iónica) en geometrías complejas y heterogéneas. La implementación de los modelos requiere tanto una adecuada formulación matemática como técnicas numéricas robustas que permitan representar con fidelidad el comportamiento de los sistemas. En este contexto, herramientas como el método de volúmenes finitos y los enfoques acoplados se han consolidado como alternativas efectivas para explorar la dinámica de los e-µPADs y guiar el diseño de dispositivos con mejor desempeño analítico [Márquez Damián et al., 2019].

La presente tesis aborda estos desafíos mediante una aproximación multiestrategia que incluye: (i) el desarrollo de metodologías experimentales precisas para la medición del flujo electroosmótico(EOF) en sustratos de papel; (ii) la implementación de un modelo multifísico que describe diferentes fenómenos de transporte en medios porosos; (iii) la propuesta de un método simplificado para la caracterización de la movilidad electroforética efectiva en papel; y (iv) la aplicación de técnicas de preconcentración específicas como la isotacoforesis (ITP) para la detección cuantitativa de compuestos de interés, como el glifosato.

Estos desarrollos permiten avanzar hacia el diseño de dispositivos e-µPADs con capacidad analítica comparable a técnicas de laboratorio, pero conservando la portabilidad, bajo costo y facilidad de uso característicos del papel. Asimismo, contribuyen a cerrar la brecha entre el conocimiento teórico sobre fenómenos electroforéticos y su implementación práctica en entornos reales de diagnóstico, monitoreo ambiental y análisis de campo.

1.1. Objetivos

1.1.1. Objetivo general

El objetivo general de esta tesis es el desarrollo de dispositivos electroforéticos microfluídicos basados en papel para detección y cuantificación de sustancias de interés ambiental, bromatológico y sanitario. Consecuentemente, el desarrollo de dispositivos como objetivo general involucra objetivos específicos parciales para cada dispositivo en particular.

1.1.2. Objetivos específicos

En particular, esta tesis contempló los siguientes objetivos específicos:

1. Caracterizar sustratos porosos para mejorar modelos computacionales existentes.
2. Diseñar métodos y dispositivos analíticos electroforéticos basados en papel a través del uso de modelos computacionales.
3. Fabricar y probar los dispositivos diseñados en condiciones de laboratorio.
4. Evaluar diferentes métodos de detección de acuerdo a las características de los analitos, los métodos de separación y el campo de aplicación del dispositivo.

1.2. Organización de la tesis

El texto principal de la tesis está organizado en cuatro capítulos, con los siguientes contenidos:

- En el presente capítulo se realiza una introducción a la temática y se describe la motivación y los objetivos a abordar en esta tesis.
- En el Capítulo 2 se presentará la metodología seguida para la resolución de los problemas.
- En el Capítulo 3 se hará un resumen de los resultados obtenidos para cada uno de los objetivos específicos propuestos.
- Finalmente, en el Capítulo 4, se darán las conclusiones generales y se discutirán potenciales trabajos futuros relacionados con los resultados de la tesis.

1.3. Antecedentes

La descripción matemática detallada y confiable para predecir el comportamiento de e-µPADs en diferentes situaciones operativas, asi como también parámetros que describen los sustratos y la dinámica de los analitos, son de interés fundamental. Su comprensión permite el desarrollo de técnicas numéricas y un diseño racional que es capaz de abarcar una amplia variedad de aplicaciones. A continuación se discuten algunos aspectos relacionados a los mecanismos fundamentales que gobiernan el funcionamiento de los e-µPADs. En particular, se analiza el flujo electroosmótico en medios porosos como proceso clave para el transporte de fluidos, así como también la formulación de un modelo multifísico que integre las distintas variables eléctricas, químicas y de transporte involucradas. Además, se aborda la movilidad electroforética de distintas especies, fuertemente

influenciada por las propiedades estructurales del medio poroso y las condiciones de operación. Finalmente, se presenta una aplicación concreta vinculada a la detección de glifosato (GlyP), destacando el potencial de estas plataformas en tareas de monitoreo ambiental y análisis de contaminantes.

1.3.1. Flujo electroosmótico en medios porosos

El desarrollo reciente de µPADs ha renovado el interés en las separaciones electroforéticas sobre sustratos porosos [Salentijn et al., 2018]. Aunque esta tecnología tuvo cierto auge a mediados del siglo XX para la separación de proteínas séricas [Cremer et al., 1950, Kunkel and Tiselius, 1951] y moléculas inorgánicas pequeñas [Durrum, 1951, Grassmann and Hannig, 1950], el surgimiento de técnicas más eficientes, como la electroforesis capilar y en gel, desplazó por décadas a las separaciones basadas en papel. En la actualidad, sin embargo, el bajo costo y la facilidad de fabricación de los dispositivos sobre papel han motivado el resurgimiento de investigaciones centradas en la utilización de dicho sustrato para aplicaciones analíticas. En el marco de la mecánica computacional, la caracterización y simulación de medios porosos representa un desafío complejo que requiere la integración de modelos matemáticos, numéricos y algoritmos computacionales para describir el comportamiento macroscópico de sistemas heterogéneos.

Distintos grupos de investigación han explorado la implementación de e-µPADs, obteniendo resultados diversos en términos de eficiencia de separación y límites de detección. Se han demostrado separaciones por electroforesis de zona sobre papel para aminoácidos [Ge et al., 2014] y aniones inorgánicos [Xu et al., 2016, Chagas et al., 2016], así como aplicaciones de ITP para mejorar la eficiencia en dispositivos de flujo lateral [Moghadam et al., 2014, Rosenfeld and Bercovici, 2014].

Sin embargo, los e-µPADs aún enfrentan limitaciones importantes, siendo la repetitibilidad una de las más críticas. Esta falencia se relaciona con la gran dispersión en los valores de los parámetros físicos que caracterizan al sustrato poroso, los cuales condicionan su comportamiento frente al flujo de fluidos, el transporte de masa y la acción de campos eléctricos [Schaumburg et al., 2020b,a]. Entre estos parámetros se encuentran la porosidad (ϕ), la tortuosidad (τ), la permeabilidad (K), el coeficiente de dispersión (s) y la movilidad electroosmótica (μ_{EOF}) [Urteaga et al., 2018, Mirzadeh et al., 2020].

De estos parámetros, ϕ, K y s suelen reportarse de forma relativamente consistente. En cambio, los valores informados para τ y μ_{EOF} muestran una variabilidad significativa, lo cual dificulta el diseño racional de dispositivos. Esta situación pone en evidencia la necesidad de una caracterización más detallada de los papeles utilizados con mayor frecuencia en aplicaciones electroforéticas.

En términos generales, μ_{EOF} se define como la relación entre la velocidad promedio del EOF (u_{EOF}) y el campo eléctrico aplicado (E), es decir [Yao and Santiago, 2003]:

$$\mu_{EOF} = \frac{u_{EOF}}{E} \tag{1.1}$$

En medios no porosos, como canales capilares o microcanales, cuando la doble capa eléctrica es delgada en comparación con el tamaño del canal, μ_{EOF} puede calcularse mediante la relación de Helmholtz-Smoluchowski [Probstein, 2003]:

$$\mu_{EOF} = -\frac{\epsilon\zeta}{\eta} \tag{1.2}$$

donde ϵ es la permitividad eléctrica del solvente, η su viscosidad, y ζ el potencial zeta, el cual depende de las propiedades de la interfaz sólido-líquido, la polaridad del solvente, la fuerza iónica y el pH de la solución [Berli et al., 2003].

A diferencia del caso capilar, existen muy pocos modelos consolidados para describir el EOF en medios porosos. La mayoría de ellos modelan el papel como un conjunto de capilares no conectados entre sí [Schaumburg et al., 2020a, Yao and Santiago, 2003, Rosenfeld and Bercovici, 2019]. En estos modelos, el potencial ζ asociado al EOF en papel (ζ_p) se considera un parámetro efectivo que resume múltiples suposiciones del modelo. En particular, Schaumburg et al. [Schaumburg et al., 2020a] propusieron un modelo que considera al papel como un medio constituido por capilares tortuosos, con una sección equivalente constante a lo largo de la tira. A partir de este modelo, y bajo el supuesto de un gradiente de presión despreciable, como suele ser el caso del EOF puro sobre una tira de papel, se obtiene una expresión modificada para μ_{EOF}:

$$\mu_{EOF} = -\frac{\phi\epsilon\zeta_p}{\tau^2\eta} \tag{1.3}$$

De acuerdo con esta expresión, el conocimiento del potencial efectivo ζ_p y de las propiedades del sustrato y del fluido permite estimar μ_{EOF} en papel. No obstante, los valores reportados en la literatura para ζ_p muestran una gran dispersión. Por ejemplo, Rosenfeld y Bercovici [Rosenfeld and Bercovici, 2019] obtuvieron $\zeta_p = -45$ mV en nitrocelulosa a pH 8, mientras que Leung [Leung et al., 2010] reportó ζ_p = -12.5 $\pm$ 6,5 mV para papel Whatman #1 a pH 3.7, utilizando una técnica monitoreo de corriente continua. Por otro lado, Schaumburg et al. [Schaumburg et al., 2020a] validaron su modelo con reportes de la literatura, empleando un valor de $\zeta_p = -15$ mV y τ = 2.9 para el mismo tipo de papel. En todos los casos, la incertidumbre asociada a estos parámetros es superior al 50 %.

Adicionalmente, varios trabajos han empleado el mencionado método de monitoreo de co-

rriente para estimar μ_{EOF} en papel [Kunkel and Tiselius, 1951, Mettakoonpitak and Henry, 2018, Schaumburg et al., 2019]. Sin embargo, este método resulta difícil de implementar en sustratos porosos ya que sufre de pobre reproducibilidad, a diferencia de lo que ocurre en microcanales o capilares. La dispersión en los valores reportados de ζ_p y μ_{EOF}, así como la falta de modelos ampliamente aceptados para medios porosos, evidencian que la caracterización de estos parámetros aún no alcanza el nivel necesario para permitir el diseño sistemático de dispositivos electroforéticos sobre papel. En consecuencia, la necesidad de modelos fiables y métodos robustos para la cuantificación de μ_{EOF} sigue vigente, especialmente considerando su impacto directo en el desempeño de los dispositivos en aplicaciones sensibles como diagnóstico en el punto de atención. Los detalles acerca de cómo se abordó la estimación de μ_{EOF} en este trabajo, incluyendo la metodología experimental y los procedimientos de análisis de datos, se desarrollan en la Sección 2.1. El artículo completo con los resultados correspondientes puede consultarse en el Apéndice A.

1.3.2. Modelo multifísico de transporte

Comprender la microestructura y las propiedades fisicoquímicas de los medios porosos resulta fundamental en múltiples áreas científicas y tecnológicas para diseñar y optimizar procesos que involucran transporte de fluídos, especies químicas y transferencia de carga eléctrica [Schaumburg et al., 2018a, Masoodi and Pillai, 2010, Gerlero et al., 2022]. Para ello, es necesario contar con modelos matemáticos confiables que describan el comportamiento macroscópico del medio a partir de su estructura microscópica, y que permitan predecir fenómenos bajo condiciones variadas, tales como imbibición capilar, flujo impulsado por gradientes de presión [Shen et al., 2021], EOF y corrientes eléctricas [Mai et al., 2019, Franck et al., 2021].

Los medios porosos, en particular los sustratos de papel, han sido objeto de numerosos estudios para comprender y modelar el transporte de fluidos. Desde comienzos del siglo XX, se han desarrollado modelos matemáticos que por lo general describen al medio como un conjunto de tubos capilares o como una red interconectada de canales. Como se comentó anteriormente, los parámetros característicos más utilizados incluyen a ϕ, que representa la fracción de volumen vacío; K, que vincula el gradiente de presión con el flujo volumétrico bajo condiciones de flujo laminar y lineal; y τ, definida como la razón entre la longitud promedio real que recorre el fluido dentro del medio y la longitud geométrica del sustrato en la dirección del flujo [Duda et al., 2011].

La dinámica de imbibición capilar ha sido tradicionalmente descrita mediante la ley de Lucas–Washburn [Washburn, 1921] , que establece que la posición del frente de fluido L_l se relaciona con el tiempo t mediante

$$L_l{}^2 = Dt$$

donde el coeficiente de difusión o de Washburn D depende de las propiedades del fluido y de la microestructura del medio poroso. La constante D se expresa generalmente en función de K, una diferencia de presión ΔP y la viscosidad dinámica η del fluido. El modelo clásico para la permeabilidad corresponde a un haz de tubos capilares rectos y paralelos de un determinado radio hidrodinámico. No obstante, al aplicar este modelo simple a sustratos de papel como Whatman #1, se observa que la velocidad de imbibición experimental es significativamente menor que la predicha. Para ajustar los datos, se introduce un radio efectivo r_{eff} notablemente menor, que puede expresarse en función de τ, e implica que el fluido recorre caminos más largos y complejos debido a la estructura fibrosa del papel, disminuyendo la permeabilidad efectiva. La tortuosidad, sin embargo, es un parámetro abstracto que no se mide directamente y que varía considerablemente según el tipo de experimento (flujo capilar, flujo hidrodinámico, transporte eléctrico) [Ezzatabadipour and Zahedi, 2021, Gerlero et al., 2021b]. Uno de los principales problemas asociados con el uso de la tortuosidad como parámetro ajustable es que los valores requeridos para reproducir los resultados experimentales suelen ser muy elevados, mucho mayores que los esperados a partir de la morfología observada del medio poroso. Esto pone en evidencia las limitaciones de los modelos basados en haces de tubos no interconectados para representar con fidelidad la complejidad estructural de sustratos como el papel.

Para superar estas limitaciones, se han desarrollado modelos más complejos, como el de tubos periódicamente constrictos [Berli et al., 2017, Sharma and Ross, 1991], que representan el medio como un haz de tubos con radios variables a lo largo de su eje . Este tipo de modelos busca capturar de manera más realista los efectos de la morfología de los poros sobre el transporte, incorporando la alternancia de constricciones y dilataciones características de medios como el papel. Si bien estos enfoques constituyen un avance significativo frente a los modelos basados en tubos rectos y paralelos, su implementación práctica requiere una adecuada selección de parámetros —como el radio hidrodinámico y el radio capilar efectivo— que no siempre pueden determinarse de forma directa a partir de la morfología del sustrato. Esto implica que múltiples combinaciones de parámetros pueden reproducir adecuadamente un experimento individual, pero no necesariamente reflejar de forma consistente el comportamiento del sistema bajo distintas condiciones. Por lo tanto, el desafío radica en identificar configuraciones de parámetros que representen fielmente la estructura del medio poroso y sean capaces de predecir simultáneamente diversos tipos de efectos, como la conducción eléctrica y el transporte hidrodinámico y capilar.

Las propiedades eléctricas de los medios porosos saturados también han sido estudiadas, destacando relaciones empíricas y modelos teóricos que vinculan la conductividad eléctrica del medio con la conductividad del fluido saturado, incluyendo enfoques basados en modelos de medio efec-

tivo, teoría de percolación y geometrías simplificadas [Archie, 1942, Bussian, 1983, Ghanbarian et al., 2014, Herrick and Kennedy, 1994].

Por otro lado, fenómenos como el EOF y la migración electroforética han recibido creciente atención debido a su relevancia en aplicaciones microfluídicas y analíticas [Schaumburg et al., 2020a]. Modelos que integren estos fenómenos junto con el transporte advectivo y difusivo permiten una descripción más completa y realista del comportamiento en medios porosos.

En consecuencia, formular un modelo matemático que incorpore la variabilidad espacial del radio de poro y contemple las múltiples físicas involucradas representa un desafío importante. Una estrategia atractiva consiste en emplear modelos de tubos periódicamente constrictos capaces de reproducir de forma coherente la dinámica de transporte bajo diferentes fenómenos físicos, como el flujo capilar, el flujo hidrodinámico y la conducción eléctrica. El principal reto es identificar un conjunto de parámetros geométricos y físicos que permita describir con precisión esta multifísica de manera unificada, evitando la dependencia exclusiva de parámetros abstractos como la tortuosidad, y capturando la heterogeneidad inherente del medio. De este modo, se busca mejorar la predictibilidad y aplicabilidad del modelo para el diseño y optimización de dispositivos µPADs y e-µPADs . La formulación metodológica del modelo multifísico propuesto se detalla en la Sección 2.2. El desarrollo completo del trabajo, incluyendo los resultados experimentales y su análisis, puede consultarse en el Apéndice B.

1.3.3. Movilidad electroforética en medios porosos

El estudio de las propiedades electroquímicas de los analitos es fundamental en distintas ramas de la química analítica [Gerlero et al., 2021b], especialmente para el diseño racional de biosensores destinados a la detección de compuestos en muestras biológicas o ambientales. En los últimos años, los e-µPADs se han posicionado como herramientas prometedoras para el análisis de proteínas [Hennig et al., 2021], ADN [Rosenfeld and Bercovici, 2018], sangre [Sena-Torralba et al., 2021] y contaminantes ambientales [Kung et al., 2019, Casado-Carmona et al., 2019].

Un aspecto clave para su desarrollo es la caracterización adecuada de las propiedades fisicoquímicas de los analitos y las soluciones buffer o de regulación de pH en interacción con medios porosos [de los Santos-Ramirez et al., 2023]. Los datos disponibles para sistemas de canal abierto, como las movilidades electroforéticas medidas en capilares y publicadas en bases de datos consolidadas [Hirokawa et al., 1983], requieren de modelos que permitan extrapolar su comportamiento en papel. Aunque estos modelos aún son escasos, su número ha ido en aumento en los últimos años [Franck et al., 2022, Novotnỳ and Gaš, 2021].

Además de su versatilidad en aplicaciones analíticas [Schaumburg et al., 2020b], los e-µPADs

ofrecen diversas técnicas de detección [Nguyen et al., 2020]. Para aplicaciones portátiles sin instrumental, la detección basada en color representa una alternativa atractiva [Schaumburg et al., 2022], tal como ocurrió con los primeros tests de embarazo [Wu et al., 2022]. Sin embargo, gran parte del desarrollo de estos dispositivos se basó en métodos empíricos [Schaumburg et al., 2018b], lo que limita su confiabilidad y robustez [Schaumburg et al., 2018a]. En este contexto, comprender el comportamiento electroforético de colorantes resulta fundamental para avanzar en dispositivos sin instrumental, lo que requiere tanto de modelos numéricos fiables como de datos experimentales validados [Damián et al., 2019].

Existen antecedentes en el uso de colorantes combinados con electroforesis en distintos contextos. Por ejemplo, colorantes de tinción de ácidos nucleicos se usan para visualizar fragmentos en geles de electroforesis, evaluando tamaño, cantidad y calidad del ADN [Haines et al., 2015]; la precipitación de colorantes se ha empleado para concentrar proteínas urinarias en análisis bidimensionales [Zukas and Breksa III, 2005]; y ciertas técnicas electroforéticas han servido para detectar colorantes que actúan como contaminantes [Ali et al., 2015]. Algunos estudios analizaron las movilidades electroforéticas de colorantes alimentarios en sistemas capilares o microfluídicos de canal abierto [Lee et al., 2008, Álvarez et al., 2017, Jager et al., 2005], aunque los valores reportados no son coincidentes. También se ha explorado la interacción de colorantes iónicos en geles porosos, observándose fenómenos de complejación y precipitación, así como la caracterización teórica y experimental de sus movilidades [Bikos and Mason, 2019]. A pesar de estos avances, aún son necesarias más investigaciones para lograr un desarrollos cuantitativos de e-μPADs sin instrumetal [Khurana and Santiago, 2008].

Para establecer correlaciones entre las movilidades en medios porosos y en canal abierto, se ha propuesto un modelo que representa el medio poroso como un conjunto de capilares no interconectados con constricciones periódicas [Franck et al., 2022]. A pesar de su simplicidad, el modelo ha demostrado ser el primero en representar simultáneamente fenómenos como la conductividad eléctrica, EOF, imbibición capilar y flujo por presión en un material homogéneo. En este contexto, también se ha logrado representar el fenómeno de electromigración. Alternativamente, la misma correlación lineal entre movilidades puede derivarse desde modelos continuos para medios porosos, si se consideran adecuadamente sus parámetros característicos [Gerlero et al., 2021a].

La movilidad electroforética (μ_e) representa la velocidad de migración de una partícula cargada bajo un campo eléctrico [Dovhunová et al., 2020], y depende de factores como la fuerza iónica (I) y el pH del medio, que afectan la carga efectiva de la molécula [Nowak et al., 2022]. La movilidad en papel, sin tener en cuenta otras interacciones, puede estimarse mediante:

$$\mu_p{}^0(pH, I) = \left(\frac{\phi}{C}\right) \mu_e(pH, I)$$

donde C es el factor de constricción [Franck et al., 2022]. Sin embargo, al realizar mediciones experimentales, se deben considerar también los efectos del EOF, que suma una contribución adicional a la movilidad medida [Franck et al., 2021]:

$$\mu_p(pH, I) = \mu_p{}^0(pH, I) + \mu_{EOF}(pH, I)$$

Finalmente, para incorporar las interacciones entre los colorantes y el sustrato, como la adsorción o retención, la movilidad debe corregirse mediante un factor de retardo específico para cada colorante [Jaitpal et al., 2022]. La caracterización precisa de estos parámetros, en especial de la movilidad electroforética, resulta entonces esencial no sólo para interpretar los fenómenos observados, sino también para desarrollar modelos predictivos confiables que permitan optimizar el diseño y funcionamiento de dispositivos e-μPADs sin instrumental. En la sección 2.3 se describe la metodología empleada para modelar y medir la movilidad electroforética en medios porosos. Los resultados de las simulaciones y el análisis detallado se presentan en el Apéndice C.

1.3.4. Detección de glifosato en un e-μPAD

El GlyP es el herbicida de mayor uso a nivel mundial. Solo en el sector agrícola, su uso aumentó más de 260 veces entre 1974 y 2014, impulsado principalmente por la adopción de cultivos genéticamente modificados tolerantes al GlyP a partir de 1996 [Benbrook, 2016], extendiéndose a aplicaciones agrícolas, forestales y urbanas [Huhn, 2018]. No obstante, el uso excesivo y no regulado del GlyP ha generado preocupación por su impacto ambiental [Bruggen et al., 2018], especialmente por su movilidad hacia cuerpos de agua superficiales, donde puede representar una amenaza para los ecosistemas [Gill et al., 2017]. A pesar de estos riesgos, muchos países aún no implementan monitoreos sistemáticos de GlyP en aguas [Oltramare et al., 2022].

Para el análisis de GlyP, la técnica estándar es la cromatografía líquida acoplada a espectrometría de masas (LC-MS), generalmente luego de una derivatización con cloruro de 9-fluorenil metilcarbonilo (FMOC), lo cual encarece y ralentiza los análisis [Okada et al., 2018]. Por esta razón, se han investigado métodos alternativos basados en técnicas espectroscópicas, sensores electroquímicos o electroforesis capilar (CE) [Valle et al., 2018]. Particular relevancia han cobrado los métodos colorimétricos, dado su bajo requerimiento instrumental. Algunos de estos han alcanzado límites de detección compatibles con el monitoreo ambiental. Por ejemplo, utilizando una sonda fluorescente en combinación con complejación competitiva con cobre, se logró detectar GlyP con

una simple lámpara ultravioleta (UV) como único equipamiento, alcanzando un límite de detección (LOD) de 12,04 nM [Wei et al., 2023].

Más recientemente, se desarrolló un método colorimétrico con detección a simple vista, en el cual la complejación de Cu^{2+} con violeta de pirocatecol (PV) genera un complejo azul. Debido a que el GlyP presenta una constante de formación de complejo con Cu^{2+} mayor que la del PV, la competencia por el cobre genera una disociación del complejo azul y la aparición del color amarillo característico del PV libre. Este cambio permite detectar GlyP visualmente en agua de grifo con un límite de detección de 20 µM, y cuantificar mediante análisis con teléfono móvil concentraciones tan bajas como 2,66 µM [Yadav and Zelder, 2021].

Sin embargo, estos métodos enfrentan dos grandes limitaciones. En primer lugar, las concentraciones de GlyP en cuerpos de agua superficiales suelen encontrarse por debajo de 6 nM [Ulrich and Ferguson, 2021, Schwientek et al., 2024], lo que hace insuficiente la sensibilidad de los enfoques actuales. En segundo lugar, la presencia de agentes complejantes en la matriz, como el EDTA, interfiere en el análisis al formar complejos con Cu^{2+} de manera más eficiente que el PV, impidiendo la detección de GlyP.

Una estrategia para superar estas limitaciones consiste en incorporar una etapa previa de preconcentración de muestra y eliminación de interferencias antes de la detección colorimétrica. En este contexto, la ITP sobre papel aparece como una técnica prometedora para cumplir ambas funciones.

Los ensayos colorimétricos en papel se han empleado desde hace más de un siglo. Sin embargo, en las últimas décadas, los e-μPADs han cobrado gran protagonismo por su bajo costo, portabilidad, rapidez y bajo consumo de muestra. Estos dispositivos pueden integrarse con métodos de detección colorimétricos, electroquímicos [Ferreira et al., 2021], u ópticos, y utilizar detectores simples como cámaras de teléfonos móviles [Zheng et al., 2021]. El análisis de imágenes obtenidas mediante estos dispositivos puede realizarse mediante programas informáticos, utilizando información del color o de canales individuales del espacio de color [Nery and Kubota, 2013].

La mayoría de los µPADs utilizan fenómenos de imbibición capilar o difusión para transportar la muestra hasta los reactivos. Sin embargo, estos mecanismos pasivos no permiten separar el analito de interés de los compuestos interferentes presentes en la matriz. Esta separación puede lograrse mediante el uso de campos eléctricos que movilicen activamente especies cargadas, como el GlyP.

Los e-μPADs han ganado atención en los últimos años [Salentijn et al., 2018], especialmente por su integración con tecnologías móviles para la detección [Schaumburg et al., 2020b, 2022]. Estos dispositivos han permitido la preconcentración y separación eficiente de proteínas séricas

humanas y bovinas [Niu et al., 2018], así como el análisis de biomarcadores como lípidos, carbohidratos, ácidos nucleicos y células [Pagaduan et al., 2015]. Asimismo, se han utilizado para mejorar el límite de detección de ensayos inmunológicos en flujo lateral. En estos casos, la técnica de isotacofóresis ha demostrado ser eficaz, alcanzando factores de preconcentración de hasta 900 veces [Moghadam et al., 2014].

La ITP se basa en sistemas electrolíticos con gradientes o perfiles discontinuos de concentración, permitiendo concentrar analitos traza en una región estrecha. Esta técnica ha sido implementada exitosamente tanto en microfluídica como en análisis bioquímicos y químicos en papel [Ramachandran and Santiago, 2022], mejorando sustancialmente los límites de detección [Malá and Gebauer, 2018]. Su versatilidad en el análisis de compuestos iónicos la convierte en una herramienta valiosa para aplicaciones biomédicas y medioambientales [Malá and Gebauer, 2023].

La combinación de detección colorimétrica con técnicas de separación electroforética en papel, como la ITP, representa una estrategia innovadora para el monitoreo ambiental de GlyP. Esta integración permite resolver limitaciones actuales en sensibilidad y selectividad, y ofrece una alternativa accesible en contextos donde el equipamiento es limitado o las regulaciones son escasas.

Para una descripción detallada de la metodología implementada en el dispositivo de detección de GlyP mediante e-μPADs con ITP en papel, se remite al capítulo 2.4, mientras que el desarrollo completo y validaciones experimentales se encuentran disponibles en el apéndice D.

Capítulo 2

Metodología

En el presente capítulo se expone la metodología empleada para abordar los problemas objetivo, describiendo en detalle las técnicas experimentales, los modelos matemáticos y las estrategias numéricas utilizadas.

Se introduce un método gravimétrico innovador para la medición precisa del EOF en papel, así como el desarrollo y la validación experimental de un modelo de tubos constrictos. Asimismo, se presenta la utilización de métodos computacionales especializados para la simulación de la imbibición capilar y los fenómenos de electroforesis, aplicados a la medición de movilidades electroforéticas. Este último modelo también fue empleado en el diseño y la optimización de un dispositivo destinado a la detección de GlyP. La integración de caracterización experimental y modelado computacional constituye el eje central de esta tesis, sentando las bases para futuros diseños y optimizaciones de sistemas microfluídicos acoplados.

Cada sección de este capítulo se corresponde directamente con uno de los cuatro artículos que forman la compilación de esta tesis:

- La **Sección A.2** describe la metodología presentada en el **Artículo 1** (Anexo A).
- Las **Secciones B.2** y **B.3** corresponden a la metodología del **Artículo 2** (Anexo B).
- La **Sección C.3** presenta la metodología del **Artículo 3** (Anexo C).
- La **Sección D.2** detalla la metodología del **Artículo 4** (Anexo D).

2.1. Flujo electroosmótico en medios porosos

2.1.1. Montaje experimental

Se diseñó un dispositivo para medir el EOF en tiras de 3 papeles diferentes, S&S, Whatman #1 y Munktell 00A, utilizando una balanza de precisión. El sistema consiste en dos cuchillas metálicas paralelas sobre las cuales se apoya un portaobjetos de vidrio. En el centro del portaobjetos se fija una tira de papel laminada, colocada de manera que sus extremos sobresalen para formar dos reservorios de líquido. Una de las cuchillas está apoyada sobre una balanza de precisión, mientras que la otra permanece fija sobre un soporte. De esta manera, cualquier desplazamiento de masa inducido por el EOF se traduce en una variación de fuerza medible por la balanza, gracias al momento generado respecto del punto de apoyo fijo (ver Fig. 2.1).

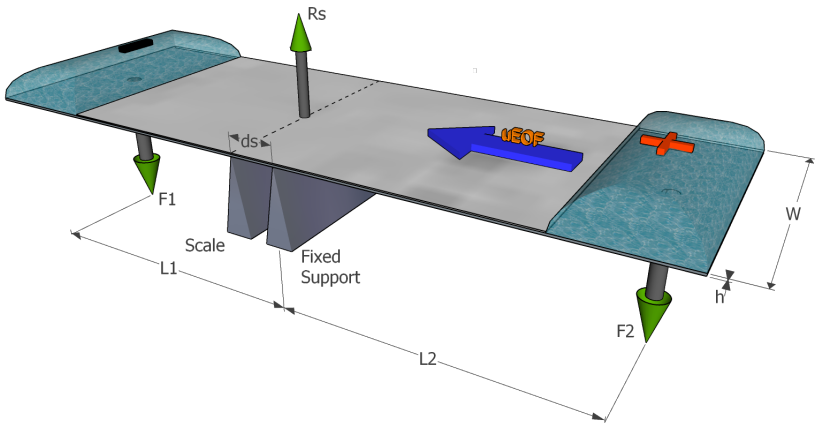

Figura 2.1: Montaje experimental utilizado para medir el EOF en sustratos de papel. Una balanza y un soporte fijo sostienen la tira de papel. Los signos menos (negro) y más (rojo) indican una posible configuración para aplicar el potencial eléctrico en los reservorios R_1 y R_2, respectivamente, generando EOF en la dirección indicada por la flecha azul. Esta dirección se alterna durante los experimentos.

Las tiras de papel fueron recortadas con láser a partir de discos comerciales de papel de filtro y luego laminadas con film plástico en ambos lados, dejando libre una sección de 9 mm en cada extremo para los reservorios. La lámina se adhirió al portaobjetos de vidrio mediante una cinta doble faz hidrofóbica.

Se aplicaron potenciales eléctricos entre ± 100 y ± 500 V mediante electrodos de platino ubicados en los reservorios. Para mitigar efectos de evaporación y procesos redox en los electrodos, la polaridad se invirtió cada 50 segundos. Los experimentos se repitieron al menos tres veces, cada uno incluyendo entre 6 y 10 ciclos de inversión de voltaje. También se realizaron mediciones de temperatura con un termómetro infrarrojo.

2.1.2. Principio de medición

El principio de medición consiste en registrar el desplazamiento de masa entre los dos reservorios producido por el EOF. Este flujo genera un desbalance sobre el sistema que se traduce en una variación en la lectura de la balanza. Si inicialmente hay equilibrio con una lectura de fuerza R_s, y luego de aplicar un campo eléctrico se traslada una masa Δm, la nueva lectura de fuerza será R_s'. La diferencia R_s = R_s' - R_s está relacionada con la masa desplazada mediante:

$$R_s = g\Delta m\frac{L_{cm}}{d_s} \tag{2.1}$$

donde g es la aceleración gravitacional, L_{cm} = L_{cm1} + L_{cm2} es la distancia total entre los centros de masa de los reservorios y d_s es la distancia entre el punto de apoyo fijo y la balanza. Cabe señalar que, al elegir un valor pequeño de d_s, se incrementa el cociente $\frac{L_{cm}}{d_s}$, lo que implica una amplificación de la variación de fuerza medida por la balanza para una misma masa desplazada.

Este diseño también permite compensar los efectos de evaporación. Si una cantidad igual de líquido se evapora de ambos reservorios y se elige $L_{cm1}{\approx}L_{cm2}$, el momento neto sobre el sistema no cambia, por lo que la lectura de la balanza permanece constante. Cualquier efecto residual producido por alguna asimetría en el sistema se elimina mediante el promedio de los ciclos de voltaje de signo opuesto.

u_{EOF} se calculó mediante la siguiente expresión:

$$u_{EOF} = \frac{R_s d_s}{gwh\rho_m \Delta t L_{cm}} \tag{2.2}$$

donde w y h son el ancho y el espesor del canal de papel, respectivamente, ρ_m es la densidad del líquido y Δt es el intervalo de tiempo durante el cual ocurre la transferencia de masa Δm.

2.1.3. Calibración del sistema

Para determinar el factor de amplificación L_{cm}/d_s, se utilizó un método experimental simple que evita errores asociados a la estimación geométrica del centro de masa del líquido en los reservorios. En equilibrio, se coloca una gota de masa conocida m_0 en el reservorio 1, y se registra la variación en la lectura de la balanza Δm_1. Luego se agrega otra gota idéntica en el reservorio 2, lo cual produce una variación opuesta Δm_2.

El factor de amplificación se obtiene como:

$$\frac{L_{cm}}{d_s} = \frac{\Delta m_1 - \Delta m_2}{m_0} \tag{2.3}$$

En los experimentos realizados, el factor de amplificación resultante fue de alrededor de 25.

2.1.4. Procesamiento de datos

Los datos obtenidos de la balanza se procesaron para calcular la masa desplazada por unidad de tiempo, $\Delta m/\Delta t$, lo cual permite determinar la velocidad del EOF. Este valor se utilizó para calcular μ_{EOF}, que caracteriza el comportamiento del EOF en los diferentes papeles analizados.

Para cada experimento, se analizaron múltiples ciclos de aplicación de voltaje y se descartaron los primeros segundos de cada ciclo para evitar efectos transitorios. Los datos se ajustaron mediante regresiones lineales para estimar las pendientes y, con ellas, las velocidades medias del flujo inducido.

2.2. Modelo multifísico de transporte

La Fig. 2.2 muestra un esquema simplificado de un sustrato poroso modelado como un conjunto de N_p tubos paralelos con constricciones. La función $R(x)$ representa el radio del tubo en función de la distancia x, que es la dirección principal del flujo y del campo eléctrico.

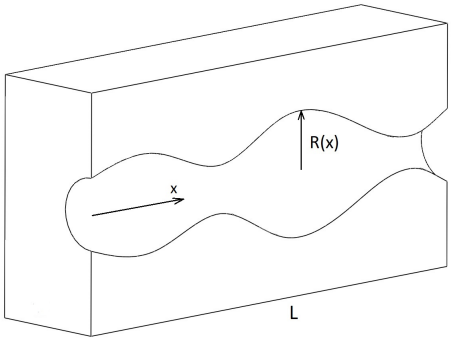

Figura 2.2: Esquema simplificado de un tubo con constricción. La estructura se repite aleatoriamente N_p veces, sin conexión entre los tubos vecinos.

La porosidad se calcula como:

$$\phi = \frac{N_p \int_0^L \pi R(x)^2 dx}{AL}$$

donde A es el área de la sección transversal y L la longitud del material.

2.2.1. Modelo hidrodinámico

Asumiendo que $R(x)$ es suave a lo largo de x y despreciando efectos inerciales (número de Reynolds bajo), el caudal a través de un único poro se calcula usando la relación de Hagen-Poiseuille [Reyssat et al., 2008]:

$$Q_h = \frac{\Delta P \pi}{8\eta \int_0^L R(x)^{-4} dx}$$

donde ΔP es la diferencia de presión aplicada y η la viscosidad del líquido. El caudal total para N_p tubos es $Q_H = N_p Q_h$, lo que lleva a:

$$Q_H = \frac{\Delta P \phi A}{8\eta L} \frac{1}{\int_0^L R(x)^2 dx \int_0^L R(x)^{-4} dx}$$

El momento estadístico de orden n de la distribución de radios se define como:

$$< R^n > \equiv \frac{\int_0^L R(x)^n dx}{L}$$

Así, se puede definir un radio hidráulico equivalente R_H:

$$R_H \equiv \sqrt{\frac{Q_H 8\eta L}{\Delta P \phi A}} = \sqrt{\frac{1}{\langle R^{-4} \rangle \langle R^2 \rangle}}$$

Este es el valor de radio que tendría un tubo de sección constante que produce el mismo caudal que el tubo constricto. El segundo miembro relaciona momentos de la distribución de radios con este valor de radio hidráulico efectivo medible.

2.2.2. Modelo de imbibición capilar

La imbibición capilar en materiales porosos ha sido ampliamente estudiada [Cai et al., 2022, Piovesan et al., 2022]. Para un tubo con constricciones, la dinámica de llenado se modela como [Young, 2004, Gorce et al., 2016, Reyssat et al., 2008]:

$$\int_0^L R(L_l)^3 \left[\int_0^{L_l} \frac{dx}{R(x)^4} \right] dL_l = \frac{\gamma \cos\theta t_{fill}}{4\eta}$$

donde L es el largo total del tubo, L_l es la posición de la interfaz, x la dirección del flujo, γ es la tensión superficial, θ el ángulo de contacto, y t_{fill} el tiempo de llenado.

Asumiendo una morfología homogénea a lo largo de x, es decir, que la función de densidad de

probabilidad (PDF) es igual en todas las regiones macroscópicas, se puede escribir:

$$\int_0^L R(L_l)^3 \left[\int_0^{L_l} \frac{dx}{R(x)^4}\right] dL_l \approx < R^{-4} > \int_0^L R(L_l)^3 L_l \, dL_l$$

Suponiendo un perfil periódico de radio, con periodo l_p y $L \gg l_p$, se obtiene:

$$\int_0^L R(L_l)^3 L_l \, dL_l \approx < R^3 > \frac{L^2}{2}$$

Sustituyendo en la primer ecuación:

$$< R^{-4} >< R^3 > \frac{L^2}{2} \approx \frac{\gamma \cos\theta t_{fill}}{4\eta}$$

Se define un radio capilar equivalente R_C:

$$R_C \equiv \frac{2L^2\eta}{\gamma \cos\theta t_{fill}} = \frac{1}{\langle R^{-4} \rangle \langle R^3 \rangle}$$

Este radio equivale al de un tubo recto que reproduce el mismo tiempo de imbibición capilar que un tubo con variaciones en su sección transversal. El resultado coincide con modelos previos para tubos sinusoidales y películas mesoporosas [Sharma and Ross, 1991, Berli et al., 2017]. Además, permite calcular el valor de D efectivo [Washburn, 1921]:

$$D = \frac{\gamma \cos\theta R_C}{2\eta}$$

2.2.3. Modelo eléctrico

Asumiendo que $R(x)$ es suave y que la conductividad eléctrica de las fibras es despreciable, la resistencia eléctrica de un conjunto de N_p tubos paralelos se calcula como:

$$\Omega_p = \frac{\rho_e}{N_p} \int_0^L \frac{dx}{\pi R(x)^2}$$

donde ρ_e es la resistividad del líquido.

Aplicando la ecuación de la porosidad, se obtiene:

$$\Omega_p = \frac{\rho_e \int_0^L \pi R(x)^2 dx \int_0^L \frac{dx}{\pi R(x)^2}}{\phi A L}$$

lo cual lleva a la relación:

$$\Omega_p \left(\frac{\phi A}{\rho_e L} \right) =< R^2 >< R^{-2} >$$

El término del lado derecho representa un factor de constricción C, que siempre es mayor a 1 para tubos constrictos o bien igual a 1 en el caso de tubos de radio uniforme. La resistencia eléctrica de un material saturado, $\frac{\rho_e L}{\phi A}$, corresponde a un prisma rectangular equivalente de resistividad ρ_e, sección $\phi\ A$ y longitud L.

2.2.4. Modelo de flujo electroosmótico

El EOF surge al aplicar una diferencia de potencial $\Delta\Phi$ en un medio poroso saturado, cargado eléctricamente en la interfaz sólido-líquido. La velocidad se calcula como el producto de la movilidad electroosmótica ($\mu_{EOF} = \frac{\epsilon\zeta}{\eta}$) y el campo eléctrico ($E = \frac{\Delta\Phi}{L}$).

Para un solo poro de radio variable $R(x)$, el caudal Q_{eof} es:

$$Q_{eof} = \pi R^2 \frac{\epsilon\,\zeta}{\eta}\, E = \frac{\epsilon\,\zeta}{\eta}\, \frac{\Delta\Phi}{\displaystyle\int_0^L \frac{dx}{\pi\, R(x)^2}}$$

Considerando N_p poros, el caudal total en el medio poroso se expresa en función de los momentos estadísticos de los radios como

$$Q_{EOF} = \frac{\epsilon\zeta\phi A}{\eta} \Delta\Phi \frac{1}{\langle R^{-2}\rangle \langle R^2\rangle}$$

Este resultado indica que el EOF depende inversamente del producto de los momentos $\langle R^{-2}\rangle$ y $\langle R^2\rangle$, que es el mismo factor de constricción C hallado para el modelo eléctrico, reflejando la influencia de la distribución del tamaño de los poros. Aunque no es posible determinar directamente estos momentos sólo a partir de la medición de Q_{EOF} sin conocer el potencial ζ, la relación puede invertirse usando medidas eléctricas para obtener los momentos y así estimar ζ a partir de experimentos de EOF.

2.2.5. Diseño Experimental

Se realizaron tres tipos de experimentos para caracterizar el transporte en dos tipos de papel diferentes (Whatman #1 y Munktell 00A): flujo inducido por presión hidrostática, imbibición capilar y conducción eléctrica. La Fig. 2.3 muestra los esquemas de configuración de cada montaje.

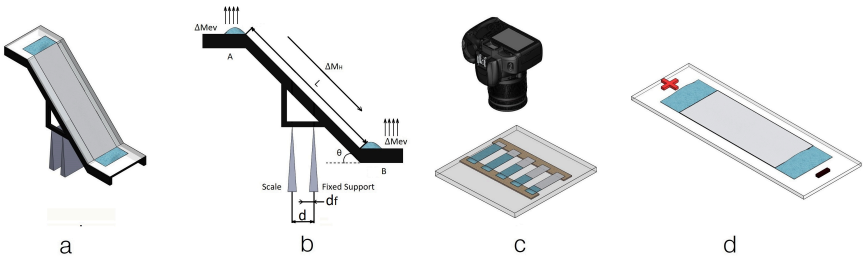

Figura 2.3: Esquemas experimentales: (a, b) flujo inducido por presión hidrostática, (c) imbibición capilar, (d) conducción eléctrica.

2.2.5.1. Flujo inducido por presión hidrostática

Para medir el flujo inducido por gravedad, se conectaron dos reservorios a cada lado de la tira de papel de manera tal que se encontraran a diferente altura y se registró la variación de masa entre de ellos utilizando un sistema similar al descrito en la sección 2.1.1, como puede observarse en las Figs. 2.3a y 2.3b . La calibración se realizó depositando volúmenes conocidos de líquido a cada lado y observando la respuesta del sistema, permitiendo determinar un factor de amplificación y corregir los efectos de evaporación. Este método posibilitó la medición precisa de caudales pequeños inducidos por diferencias de altura entre reservorios.

2.2.5.2. Imbibición capilar

La imbibición capilar se estudió colocando 10 tiras de papel de forma horizontal, mojando los reservorios de uno de los extremos. La saturación progresiva de los papeles se observó con una cámara y luz de fondo, permitiendo distinguir claramente la región húmeda de la seca (Fig. 2.3c).

El avance del frente húmedo se midió en función del tiempo, y los datos se ajustaron a la ley de Washburn, que establece que la distancia recorrida es proporcional a la raíz cuadrada del tiempo. Este análisis permitió estimar el radio capilar efectivo del papel R_C, previamente desarrollado.

Se realizaron experimentos con diferentes soluciones para evaluar el efecto de propiedades como viscosidad y concentración de solutos sobre la velocidad de imbibición, aportando información valiosa para modelar el transporte capilar en el sistema.

2.2.5.3. Experimentos eléctricos

Se realizaron mediciones eléctricas para determinar la resistencia del papel saturado, usando diferentes soluciones electrolíticas para variar la conductividad del líquido. Se aplicó un potencial constante bajo (aprox. 10 V) a través de tiras de papel de 10 mm de ancho y 40 mm de largo, minimizando efectos de calentamiento Joule y EOF (Fig. 2.3d). La resistividad de las soluciones

se midió con un medidor de conductividad. Mas detalles pueden encontrarse en la sección B.3.1 del apéndice B.

2.3. Movilidad electroforética en medios porosos

2.3.1. Modelo matemático

Como se describió en la sección anterior, el medio poroso se modela como un conjunto de capilares periódicamente constrictos y no interconectados [Franck et al., 2022], lo que permite representar varios fenómenos físico-químicos simultáneamente, incluyendo la electromigración.

La movilidad electroforética efectiva en el medio poroso se relaciona con la movilidad en canal abierto (μ_e) mediante ϕ y C:

$$\mu_p{}^0(pH, I) = \left(\frac{\phi}{C}\right) \mu_e(pH, I)$$

donde el pH y la fuerza iónica (I) afectan la movilidad.

Además, la contribución del EOF, que modifica el desplazamiento macroscópico medido, se agrega como un término adicional:

$$\mu_p(pH, I) = \mu_p{}^0(pH, I) + \mu_{EOF}(pH, I)$$

Finalmente, para considerar la interacción retardante de las moléculas con el sustrato, se introduce un factor de retardo R_f específico para cada colorante, dando la movilidad efectiva corregida:

$$\mu_p^{eff}(pH, I) = R_f \mu_p(pH, I) = R_f \left(\frac{\phi}{C}\mu_e(pH, I) + \mu_{EOF}(pH, I)\right)$$

2.3.2. Electroforesis capilar

Se midieron cinco colorantes alimentarios comunes: Naranja de metilo, Fast Green FCF, Tartrazina, Rojo Ponceau y Azul Brillante. Las movilidades electroforéticas de estos colorantes fueron evaluadas tanto en sistemas de CE como en el dispositivo de papel. Para ello, se emplearon dos soluciones buffer como electrolito de fondo (BGE), uno a pH 5.5 (Tris-Acetato) y otro a pH 9.0 (Amonio-Acetato), seleccionados por su uso frecuente en sistemas de papel y para permitir estudiar el efecto del pH. Los ensayos de CE se realizaron en un equipo con detección UV, utilizando un capilar de sílice fundida sin recubrimiento (75 µm de diámetro interno y 31 cm de longitud total).

2.3.3. Electroforesis en papel

Se diseñaron dispositivos de papel cortados a partir de discos de papel de filtro Whatman grado N.º 1 (150 mm) utilizando un láser de CO_2 de 40 W. Luego del corte, los dispositivos fueron laminados en caliente para prevenir evaporación. Se dejaron espacios simétricos de 5 mm sin laminar en los extremos del canal central para formar reservorios de líquido (ver Fig. 2.4). Este laminado no afecta significativamente la porosidad del papel [Elizalde et al., 2015, Gerlero et al., 2022].

El dispositivo se monta sobre una cinta adhesiva hidrofóbica de doble faz adherida a una placa de vidrio, lo que evita derrames y flujos secundarios. Se aplicó un potencial eléctrico con una fuente de voltaje que también mide la corriente aplicada.

Para medir el R_f de los colorantes se usaron tiras rectangulares de papel de 10 mm × 40 mm, laminadas parcialmente para dejar espacio a los reservorios de entrada. Se emplearon soluciones de colorante y buffer con las mismas concentraciones que en las pruebas electroforéticas.

Los experimentos se registraron con una cámara fotográfica ubicada a 30 cm del dispositivo, iluminando desde abajo con un diodo emisor de luz (LED) de color blanco. Los detalles sobre la composición de las soluciones buffer tanto de esta como de la sección 2.3.2, así como la información técnica de los equipos utilizados, se incluyen en el anexo C.

2.3.4. Funcionamiento del dispositivo

El dispositivo de electroforesis en papel (Fig. 2.4) se compone de tres zonas: entrada, detección y salida. En la zona de entrada se introduce el colorante diluido en el BGE, mientras que en los extremos de la zona de detección se colocan los reservorios con buffer. La zona de salida contiene una bomba capilar hecha del mismo papel.

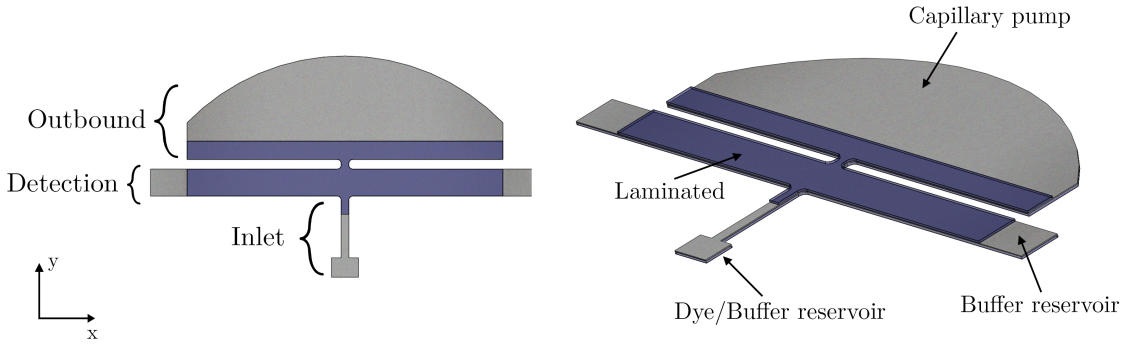

Figura 2.4: Dispositivo de electroforesis en papel. Se observan las tres zonas funcionales: entrada, detección y salida. La inyección del colorante ocurre desde la zona de entrada. Posteriormente, se genera una línea delgada en la zona de detección mediante inversión del flujo, y finalmente se aplica un campo eléctrico para realizar la separación. La laminación evita la evaporación durante los experimentos.

La operación consta de tres etapas: inyección, enfoque y electroforesis. En la *etapa de inyección*, el buffer avanza desde los reservorios laterales hacia el centro, y poco antes de que se encuentren los frentes de mojado, se agrega la solución de colorante en el extremo inferior. El diseño geométrico permite limitar la dispersión mecánica, generando una forma triangular inicial en la zona de detección [Urteaga et al., 2018].

En la *etapa de enfoque*, se reemplaza la entrada de colorante por otra bomba capilar. Esta redistribuye el colorante, generando una línea delgada adecuada para el análisis electroforético. La geometría de las alas laterales y las resistencias hidrodinámicas determinan las trayectorias del flujo.

Finalmente, en la *electroforesis*, se aplica una diferencia de potencial constante de 500 V entre los extremos de la zona de detección. Dos electrodos de platino se colocan en los reservorios laterales, generando un campo eléctrico que permite observar el movimiento diferencial de los colorantes. La longitud de las alas y el ancho del canal (8 mm) están diseñados para maximizar la resolución sin introducir efectos de borde significativos. La sección C.3.4 del apéndice C proporciona información ampliada al respecto.

2.3.5. Herramientas computacionales

Para determinar la posición espacial de los colorantes, se utilizó un método de detección por intensidad relativa. Se recortaron los perfiles de intensidad al 50 % del valor máximo, y se tomó ese punto como posición del colorante. A partir de la posición en función del tiempo, se aplicó un ajuste lineal por mínimos cuadrados. Los experimentos se repitieron, en la mayoría de los casos, tres veces y se utilizó el valor medio y la desviación estándar para calcular la movilidad efectiva. La principal fuente de dispersión proviene de la variabilidad entre tiras de papel [Elizalde et al., 2016].

En cuanto a las simulaciones computacionales, las mallas se generaron con el software STAR-CCM+ ®, utilizando aproximadamente 250.000 celdas de distribución mayormente uniforme. Las simulaciones se realizaron con OpenFOAM® v2112, empleando los solvers `porousMicroTransport` (modelo LETd para flujo capilar no saturado) [Gerlero et al., 2023, 2022] y `electroMicroTransport` (para separaciones electroforéticas) [Gerlero et al., 2021b].

2.3.5.1. Condiciones de borde

Durante la *etapa de inyección*, se aplica una condición de saturación en los extremos de los tres reservorios para modelar el llenado capilar, con contenido de humedad inicial correspondiente al aire seco y condiciones de flujo nulo en el resto del dominio. Los buffer se introducen mediante

condiciones de Dirichlet en los reservorios, con concentración inicial nula en el dominio y condiciones de flujo nulo en los demás bordes, al igual que el colorante.

En la *etapa de enfoque*, la condición en el reservorio de colorante/buffer cambia a flujo nulo, simulando su agotamiento.

Durante la *electroforesis*, se asume saturación completa, por lo que no se resuelve más el flujo capilar. El modelo considera transporte electroforético y EOF. Las concentraciones tienen condiciones de flujo nulo en todo el dominio, y el potencial eléctrico se impone con condiciones de Dirichlet en las entradas laterales.

2.4. Detección de glifosato en un e-μPAD

Para el desarrollo de los experimentos se utilizó GlyP estándar (98 %) junto con colorantes, complejos metálicos y disoluciones tampón, incluyendo BGE como HEPES, MES, y soluciones de amoníaco y ácido fórmico para ITP, todos preparados en agua ultrapura y sin purificación adicional.

2.4.1. Optimización de la detección colorimétrica

Se registraron espectros UV/VIS con un espectrofotómetro para analizar las constantes de estabilidad para los complejos Cu^{2+}-GlyP ([GLP])(log $\beta \approx$ 11.8–11.9) [Daniele, 1997, Madsen et al., 1978, Popov et al., 2001] y se asumió un valor aproximado de 5.7 para el complejo Cu^{2+}-PV ([PV]) [Yadav and Zelder, 2021, Kocyła et al., 2017]. Estas constantes dependen del pH y de las condiciones del medio, por lo que se utilizaron como referencia para estimar la competitividad del GlyP en la formación de complejos.

2.4.1.1. Evaluación de sustratos porosos

Se evaluaron tres soportes porosos para su uso en e-µPADs: papel de celulosa, nitrocelulosa y una placa de cromatografía de capa fina ALUGRAM RP-18W/UV_{254}. Se recortaron fragmentos de 5 mm x 5 mm, sobre los que se aplicaron soluciones de [PV] (75 µM) preparadas con colorante y Cu^{2+} en MES pH 6.5. Se ensayaron soluciones de GlyP con concentraciones entre 0 y 500 µM. Luego de secados, se aplicó el complejo colorimétrico y se tomaron fotografías en cada etapa para evaluar la visibilidad y el contraste en los diferentes sustratos.

2.4.2. Análisis por electroforesis capilar acoplada a espectrometría de masas (CE-MS)

Los análisis se realizaron en un sistema Agilent 7100 CE acoplado a un espectrómetro de masas por interfaz de electrospray. Las separaciones se realizaron en un capilar de sílice fundida (50 µm diámetro interno, 75 cm de longitud), con acondicionamiento previo y recubrimiento dinámico.

Se aplicó una presión interna de 50 mbar y un voltaje creciente de -15 kV a -30 kV. La inyección fue hidrodinámica y la detección se realizó en modo monitoreo de iones seleccionados (SIM) .

2.4.3. Herramientas computacionales

Las simulaciones numéricas se realizaron con OpenFOAM v2212®, utilizando el solver `electroMicroTransport` para separaciones electroforéticas [Gerlero et al., 2021b]. La malla fue generada con *blockMesh*, con aproximadamente 15 000 celdas distribuidas uniformemente. El modelo geométrico fue una tira rectangular de papel con una distancia efectiva de aplicación del campo eléctrico de 65 mm. Se consideró el transporte electroforético sin EOF, con condiciones de frontera de flujo nulo para los electrolitos y potencial prescrito en los reservorios. La porosidad y la tortuosidad del papel se determinaron experimentalmente de acuerdo a modelos anteriores [Franck et al., 2022]. Las movilidades electroforéticas se obtuvieron de PeakMaster, salvo la de GlyP, que se obtuvo de la bibliografía [Graf et al., 2022].

2.4.4. Electroforesis en papel

Se desarrolló un e-µPAD de bajo costo esquematizado en la Fig. 2.5a . Consiste en una carcasa impresa en 3D con una cámara de separación, reservorios para ánodo y cátodo con electrodos de platino, y una tira de nitrocelulosa de 80 mm de largo por 10 mm de ancho. La tira se apoyó sobre un vidrio, uniendo los dos reservorios, y se iluminó con una lámpara LED difusa de color blanco ubicada debajo del dispositivo de manera que se registró la luz transmitida a través de la tira.

2.4.4.1. Electroforesis capilar en papel

A partir de los resultados colorimétricos, se desarrolló una electroforesis capilar en papel (pCE) utilizando MES como BGE ajustado a pH 6.5 con KOH. Se preparó una solución con 175 µM de PV y 350 µM de $CuCl_2$ en el BGE. Se emplearon soluciones de GlyP a 100, 150, 400 y 1200 μM, y en todos los casos se agregó 3 % m/v de polivinilpirrolidona (PVP) para suprimir el EOF.

2.4.4.2. ITP en papel

En ITP, los analitos se preconcentran y separan gracias al uso de un electrolito líder (LE), con mayor movilidad iónica, y un electrolito terminal (TE), con menor movilidad. Bajo un campo eléctrico, los iones de la muestra migran y se ordenan entre LE y TE según su movilidad electroforética, alcanzando una misma velocidad migratoria. Esta propiedad permite lograr zonas discretas y estables de concentración elevada, lo que hace de ITP una técnica muy efectiva para la preconcentración de especies cargadas [Ramachandran and Santiago, 2022].

Los experimentos de ITP emplearon 2,5 mM de HEPES como TE, con 5 mM de ácido ε-aminocaproico como contraión (CI). El LE fue una solución de HCl 26 mM, y como CI se usó una mezcla de ácido ε-aminocaproico y TRIS (26 mM cada uno). Todos los electrolitos se optimizaron con PeakMaster [Gaš, 2023] y simulaciones numéricas (Sección D.2.4) para mantener un pH de 6.5. Para evitar efectos de borde por imbibición, se utilizó cinta adhesiva hidrofóbica en los extremos del vidrio [Schaumburg and Berli, 2019].

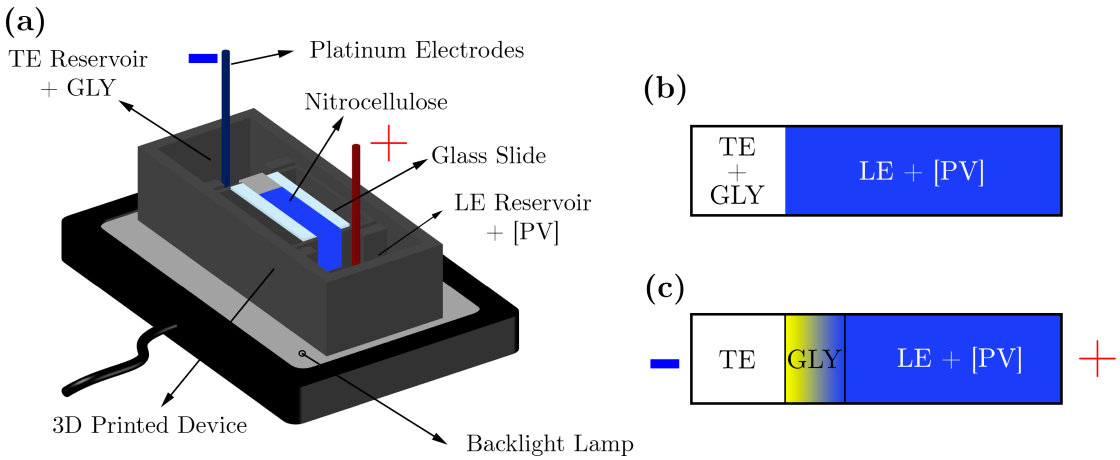

Figura 2.5: **(a)** Esquema del dispositivo e-µPAD con carcasa impresa en 3D, electrodos de platino y tira de nitrocelulosa entre los reservorios. **(b)** Configuración tras llenar los reservorios y antes de la migración. **(c)** Preconcentración de GlyP y cambio de color tras aplicar el campo eléctrico.

El reservorio del ánodo se llenó con el complejo colorimétrico [PV] a 175 µM en el LE. Luego de 150 s, el reservorio cátodico se llenó con GlyP disuelto en TE. El GlyP y [PV] se desplazaron por transporte por difusión, formando la configuración de la Fig. 2.5b.

Una vez que la tira está completamente mojada, los iones migran al aplicar un campo eléctrico. Esta configuración permite carga semi-infinita de muestra y preconcentración continua por ITP [Ramachandran and Santiago, 2022]. El cambio de color ocurre cuando GlyP preconcentrado alcanza el complejo [PV], de menor movilidad electroforética (Fig. 2.5c). Se aplicaron 400 V usando una fuente que permite la medida en simultaneo de la corriente utilizada. Se registraron

imágenes con una cámara fotográfica colocada a 30 cm. Información adicional sobre el dispositivo utilizado se presenta en la sección D.2.5.2 del apéndice D.

Capítulo 3

Resultados principales

En este capítulo se presentan los resultados más relevantes vinculados a cada uno de los objetivos específicos de la tesis, los cuales se desarrollan en detalle en los trabajos originales que forman la compilación y que se incluyen como anexos en este documento.

Cada sección de este capítulo se corresponde directamente con uno de los cuatro artículos publicados:

- La **Sección A.3** resume los resultados del **Artículo 1** (Anexo A).
- La **Sección B.4** presenta los resultados del **Artículo 2** (Anexo B).
- La **Sección C.4** aborda los resultados del **Artículo 3** (Anexo C).
- La **Sección D.3** expone los resultados del **Artículo 4** (Anexo D).

3.1. Flujo electroosmótico en medios porosos

Se midió la velocidad y movilidad electroosmótica en función del potencial eléctrico para tres valores de pH en tres tipos de papeles. A bajos potenciales se observó un comportamiento lineal, validando el modelo teórico. A mayores potenciales, la linealidad disminuyó, lo que se atribuye principalmente a efectos térmicos discutidos más adelante.

3.1.1. Cálculo de ${\mu_{EOF}}^0$ y ζ_p

La movilidad electroosmótica es, en principio, independiente del campo eléctrico. Sin embargo, al incrementar la intensidad del campo comienzan a manifestarse efectos térmicos que pueden modificar su valor. Para evitar esta dependencia con la temperatura, se define un valor de referencia de la movilidad electroosmótica a temperatura ambiente, denotado como ${\mu_{EOF}}^0$. En la Tabla 3.1

se presentan los valores de movilidad electroosmótica de referencia, ${\mu_{EOF}}^0$, junto con los valores de ζ_p, obtenidos para distintos sustratos y condiciones de pH.

	ϕ	pH	${\mu_{EOF}}^0$ $[\frac{\eta m^2}{Vs}]$	ζ_p [mV]
Whatman #1	0.69	4.78	561 ± 22	$-11{,}8 \pm 0{,}5$
		7	664 ± 65	$-13{,}9 \pm 1{,}4$
		9.29	854 ± 92	$-17{,}9 \pm 1{,}9$
Munktell 00A	0.47	4.78	537 ± 95	$-16{,}6 \pm 2{,}9$
		7	549 ± 40	$-16{,}9 \pm 1{,}2$
		9.29	512 ± 68	$-15{,}8 \pm 2{,}1$
S&S	0.42	4.78	81 ± 35	$-2{,}7 \pm 1{,}2$
		7	214 ± 52	$-7{,}3 \pm 1{,}8$
		9.29	258 ± 56	$-8{,}8 \pm 1{,}9$

Tabla 3.1: ζ_p y ${\mu_{EOF}}^0$ obtenidos para distintas soluciones buffer y tipos de sustrato. Las incertidumbres corresponden a intervalos de confianza del 95 % .

Se aplicaron correcciones al modelo lineal considerando el aumento de temperatura por efecto Joule, que afecta simultáneamente parámetros eléctricos y reológicos. Para el cálculo de ζ_p se consideró $\tau = 2{,}9$ [Schaumburg et al., 2020a]. La porosidad de los sustratos se determinó pesando los materiales secos y húmedos.

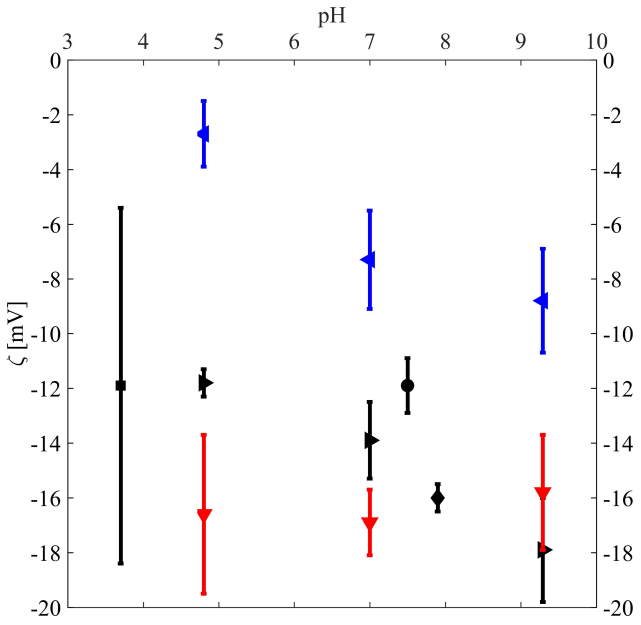

Figura 3.1: $\zeta_p(pH)$ para distintos sustratos. Marcadores cuadrados (■ [Leung et al., 2010]), circulares (● [Mettakoonpitak and Henry, 2018]) y romboidales (♦ [Schaumburg et al., 2019]) corresponden a datos bibliográficos de Whatman #1. Los triangulares representan estimaciones experimentales de este trabajo para Whatman #1 (►), Munktell 00A (▼) y S&S (◄).

Dado que se trabajó con soluciones acuosas diluidas, se usó $\eta = 1{,}0\,\text{mPa s}$ a $23\,^{\circ}\text{C}$ y permitividad relativa $\epsilon = 7{,}08 \times 10^{-10}\,\text{C}^2/\text{Nm}^2$. Los valores de ζ_p obtenidos se comparan con datos de literatura en la Fig. 3.1 . Se observa coherencia tanto en las barras de error como en la variación monótona con el pH. Los tres sustratos mostraron un aumento de μ_{EOF} y ζ_p con el pH, con mayor dependencia del pH en S&S, intermedia en Whatman #1 y muy baja en Munktell 00A. S&S, con su bajo μ_{EOF}, es adecuado para aplicaciones que requieren minimizar el EOF. Munktell 00A, con buena estabilidad frente al pH, es útil en técnicas de amplio rango de pH como isoelectroenfoque. Whatman #1 presenta un comportamiento comparable a materiales como vidrio o PDMS hidrofílico, siendo una opción apropiada para adaptar separaciones electroforéticas tradicionales a papel.

Los valores reportados corresponden a sustratos laminados para reducir evaporación, lo cual mejora la reproducibilidad. Sin embargo, podrían variar levemente si se usan sustratos sin laminar o con distintos materiales de laminado, dado que este proceso influye parcialmente en la superficie libre de fibras responsable del EOF.

3.1.2. Desviaciones del modelo lineal

Con el fin de considerar fuentes de error que desvían los valores experimentales obtenidos del modelo lineal, a continuación se describen distintos efectos presentes en el montaje experimental que afectan la medición. También se discute cómo abordarlos o cuantificarlos para mejorar futuros montajes.

3.1.2.1. Evaporación

La evaporación es un efecto importante, ya que reduce el volumen de los reservorios con el tiempo y afecta las mediciones. Sin embargo, el montaje presentado se autocompensa, como se explicó en la sección 2.1.2. La evaporación afecta simétricamente a ambos reservorios, por lo tanto, se espera que la balanza no registre cambios. Sin embargo, puede quedar un efecto residual debido a una leve asimetría en la posición relativa de los reservorios, lo cual se corrige promediando las pendientes positivas y negativas durante las mediciones.

3.1.2.2. Deriva de conductividad y efecto Joule

La resistencia eléctrica del papel disminuye con el tiempo al aplicar un voltaje. Esta variación se atribuye al calentamiento por efecto Joule, que reduce la viscosidad del electrolito y, por lo tanto, aumenta su conductividad. La resistencia puede expresarse como:

$$\Omega_p = \frac{1}{\sigma_p}\frac{L}{A}$$

donde σ_p es la conductividad eléctrica del papel y depende de la viscosidad del fluido:

$$\sigma_p = F\sum_{j=1}^{N} {z_j}^2 \frac{\mu_e}{\tau^2} C^j \phi, \quad \text{con} \quad \mu_e = \frac{q^j}{6\pi\eta r_s^j}$$

donde F es la constante de Faraday, z_j la valencia del ion j, μ_e su movilidad electroforética, C^j la concentración iónica. q^j es la carga del ion j y r_s^j su radio hidrodinámico. A altos voltajes, el calentamiento provoca no linealidades en el flujo electroósmico. Para describir este comportamiento se desarrolló un modelo donde se propone la siguiente dependencia de la constante electrosmótica con el potencial aplicado:

$$\mu_{EOF} = \frac{2{\mu_{EOF}}^0}{1+\sqrt{1-\varpi\Delta\Phi^2}}, \quad \text{con} \quad \varpi = \frac{4P}{Lwh'\Omega_p^0}$$

donde ϖ es un parámetro que depende de la pendiente P, que mide la dependencia de la viscosidad relativa con la temperatura de la solución. h' es el coeficiente de transferencia de calor convectivo y Ω_p^0 la resistencia eléctrica a temperatura ambiente. Los parámetros del modelo fueron ajustados experimentalmente y concuerdan con los valores esperados para el sistema.

3.2. Modelo multifísico de transporte

3.2.1. Resultados experimentales

Se realizaron experimentos hidrodinámicos para evaluar el radio equivalente correspondiente. Tras la calibración del sistema, se midieron variaciones de masa al colocar gotas en los reservorios superior e inferior. A partir de estas mediciones y siguiendo el protocolo de calibración descrito anteriormente (sección 2.1.3), se determinaron los factores de amplificación. El flujo másico neto se obtuvo a partir de un ajuste lineal, y se calculó de esta manera el valor de R_H.

El flujo de masa medida fue de aproximadamente $3{,}4 \times 10^{-4}$ g/sec, con factores de amplificación de flujo y evaporación de 29 y $-0{,}69$, respectivamente. El flujo evaporativo alcanzó $3{,}33\times10^{-5}$ g/sec, siendo comparable al flujo hidrodinámico a través del papel ($1{,}25\times10^{-5}$ g/sec), lo que valida la sensibilidad del sistema para distinguir ambas contribuciones, al mismo tiempo que indica la importancia de considerar este efecto para la correcta obtención del flujo.

Se realizaron también experimentos de imbibición capilar para evaluar el radio capilar equivalente. Se observó una correlación lineal del cuadrado de la posición del frente de líquido con el

tiempo, cumpliendo con la ley de Lucas-Washburn [Lucas, 1918, Washburn, 1921]. A partir de la pendiente se obtuvo el coeficiente D, dependiente del tipo de papel y del líquido. Se observaron dos grupos de valores correspondientes a distintos tipos de papel, con una dispersión del orden del 7 %, en línea con trabajos previos [Elizalde et al., 2016], aunque con valores promedio menores debido al uso de papel laminado.

Finalmente, se realizaron mediciones de conductividad eléctrica tanto en solución libre como en papel. Los resultados coincidieron con los valores teóricos esperados para las concentraciones de electrolitos a temperatura ambiente. La linealidad entre la conductancia medida y la conductividad eléctrica indicó buena correlación y ausencia de efectos relevantes como calentamiento Joule o EOF.

3.2.2. Distribución del tamaño de poro

Se evaluaron tres PDFs para describir la distribución del tamaño de los poros: (i) una distribución bimodal basada en dos funciones delta de Dirac que representan radios con igual probabilidad; (ii) una distribución tipo arcoseno que modela los radios como una función seno oscilante entre R_{max} y R_{min}; y (iii) una distribución log-normal continua, observadas en la Fig. 3.2.

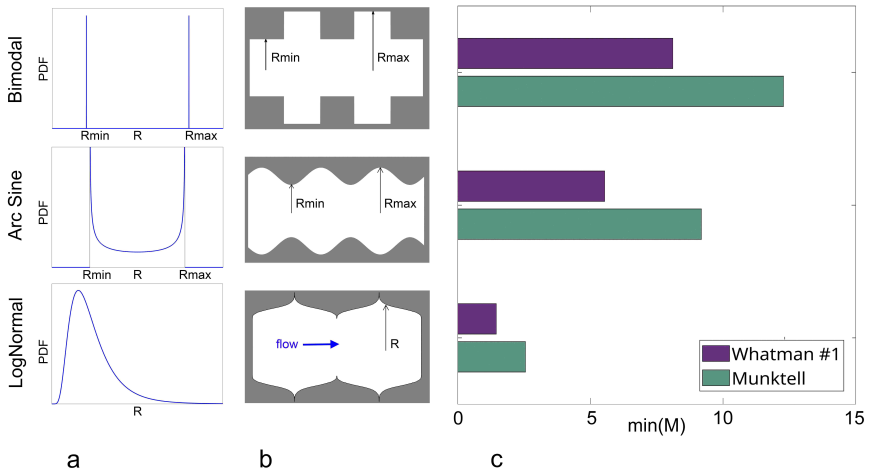

Figura 3.2: PDFs exploradas en el modelado: (a) densidades de probabilidad en función del radio, (b) representación esquemática de formas y radios característicos, (c) desempeño de cada PDF para describir datos experimentales de dos sustratos, evaluado mediante la prueba χ^2.

Las distribuciones bimodal y arcoseno son simples desde el punto de vista físico y matemático, y pueden manejarse analíticamente. Sin embargo, están limitadas en el rango de tamaños de poro que pueden describir (discreto en el caso bimodal), lo que restringe la representación de la morfología de los poros en sustratos de papel. Por otro lado, la distribución log-normal presenta

mayor complejidad, pero permite representar una variación continua y amplia en los tamaños de poro, lo que puede describir de manera más realista la distribución de poros en sustratos reales.

La distribución log-normal se define como:

$$f(R) = \frac{1}{Rv\sqrt{2\pi}} e^{-\frac{(\ln R - \xi)^2}{2v^2}}$$

donde la variable aleatoria R representa un radio específico. Los parámetros ξ y v determinan la media aritmética $E[R]$ y la varianza $Var[R]$ según:

$$E[R] = e^{\xi + \frac{v^2}{2}} = X$$

$$Var[R] = e^{2\xi + v^2}(e^{v^2} - 1)$$

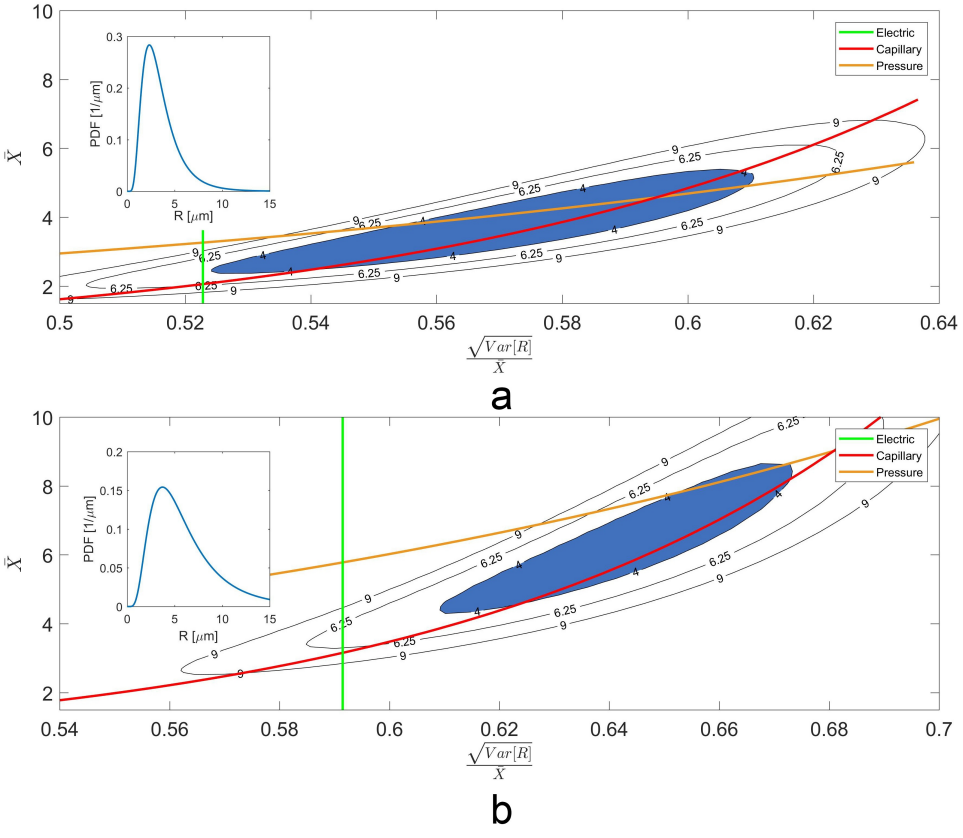

Figura 3.3: Mapa de contorno de los valores de M usando la distribución log-normal para Whatman #1 (a) y Munktell 00A (b). Las líneas sólidas indican las combinaciones de parámetros para las cuales la distribución reproduce los resultados experimentales de R_H (línea naranja), R_C (línea roja) y C (línea verde). La región coloreada en azul corresponde a $M < 3{,}84$, que representa la región de confianza del 95 % para los parámetros predichos. Los recuadros a la izquierda muestran la PDF log-normal óptima que produce el valor mínimo de M.

Para evaluar el desempeño de las PDFs, se construyó una función de mérito M que compara los valores experimentales de R_H, R_C y C con los valores predichos por el modelo para diferentes combinaciones de μ y σ (ver Fig. 3.3). Estas predicciones se calculan usando los momentos de la PDF y se ponderan según la dispersión experimental, obteniendo una distribución tipo Chi-cuadrado:

$$M(\xi, \upsilon) = \frac{(R_H - R_H(\xi,\upsilon))^2}{Var[R_H]} + \frac{(R_C - R_C(\xi,\upsilon))^2}{Var[R_C]} + \frac{(C - C(\xi,\upsilon))^2}{Var[C]}$$

Los resultados muestran que la distribución log-normal ofrece un mejor desempeño para representar simultáneamente los tres experimentos. La combinación óptima de parámetros ξ y υ se puede usar para predecir las respuestas experimentales. La mayor dispersión en Munktell indica que el modelo ajusta con menor fidelidad ese sustrato.

3.2.3. Comparación entre diferentes modelos

En la Tabla 3.2 se presenta la relación entre las PDF y parámetros clásicos de modelos de física en particular, como K, D, y ζ. También se incluyen C, y los radios equivalentes R_H y R_C para ambos sustratos.

Sustrato		**Whatman #1**		**Munktell 00A**	
Magnitud	Definición	Medición	Predicción del modelo	Medición	Predicción del modelo
Radio hidrodinámico equivalente [μm]	$R_H = \sqrt{\frac{1}{\langle R^{-4}\rangle\langle R^2\rangle}}$	$0{,}86 \pm 0{,}08$	0,79	$1{,}1 \pm 0{,}1$	0,93
Permeabilidad de Darcy $\times 10^{-14}$[m^2]	$K = \frac{{R_H}^2}{8}$	$9{,}3 \pm 0{,}9$	7,8	13 ± 1	10,9
Radio capilar equivalente [μm]	$R_C = \frac{1}{\langle R^{-4}\rangle\langle R^3\rangle}$	$0{,}089 \pm 0{,}008$	0,096	$0{,}064 \pm 0{,}006$	0,07
Coeficiente de Washburn $\times 10^{-6}$ [$\frac{\text{m}^2}{\text{s}}$]	$D = \frac{\gamma \cos\theta R_C}{2\eta}$	$1{,}8 \pm 0{,}2$	1,9	$1{,}3 \pm 0{,}1$	1,4
Factor de constricción	$C = \langle R^2\rangle\langle R^{-2}\rangle$	$2{,}6 \pm 0{,}3$	3,1	$3{,}3 \pm 0{,}3$	4
Potencial zeta [mV]	$\boldsymbol{\zeta_p} = \frac{\mu_{EOF}\eta C}{\epsilon\phi}$	$2{,}8 \pm 0{,}3$	3,3	$5{,}3 \pm 0{,}5$	6,4

Tabla 3.2: Parámetros para cada modelo físico particular y sus radios estadísticos correspondientes. μ_{EOF} se tomó de [Franck et al., 2021] para pH=4.7 y $E = 2{,}5\,\text{kV/m}$.

Las diferencias entre medición y predicción son pequeñas y en general compatibles con la

incertidumbre experimental. El modelo reproduce correctamente que R_H es aproximadamente diez veces mayor que R_C en los papeles estudiados.

En cuanto a los radios hidrodinámicos y capilares, las aparentes discrepancias [Alava et al., 2004] son inherentes a la extrapolación de modelos de flujo impulsados por capilaridad de tubos individuales a medios porosos: el principal inconveniente es considerar un radio de poro único tanto para la presión de Laplace como para la resistencia hidrodinámica.

En cuanto al EOF, el factor de constricción predicho es similar a la tortuosidad reportada para fenómenos electroforéticos y EOF [Gerlero et al., 2021b], aunque difiere de valores para transporte de fluidos [Matyka et al., 2008]. Además, estos valores corresponden a papel laminado por ambos lados y pueden variar en papeles con distinto tratamiento superficial [Noh and Phillips, 2010, Elizalde et al., 2016].

3.3. Movilidad electroforética en medios porosos

3.3.1. Prototipo asistido numéricamente

El diseño del dispositivo fue asistido numéricamente, y los resultados de las simulaciones definieron su configuración final. La secuencia operativa se analiza en tres etapas: inyección, enfoque y electroforesis.

Durante la etapa de inyección, las longitudes de los canales determinan la dinámica de imbibición de las soluciones. Al fijar un punto de control en el centro de la zona de detección, se puede ajustar el tiempo de entrada del buffer y el analito para que lleguen simultáneamente. La imbibición en tiras de papel homogéneo sigue la relación $L_l{}^2 = Dt$ y es independiente del ancho. La incertidumbre típica del coeficiente D ($\sim$20 %) [Elizalde et al., 2016] puede afectar el tiempo de llegada, aunque no altera la configuración cuasi-estacionaria de los colorantes.

La Fig. 3.4 muestra la comparación entre simulaciones y resultados experimentales. En la etapa de inyección, la distribución triangular del colorante en condiciones cuasi-estacionarias es reproducida por el modelo numérico. En la etapa de enfoque, el analito remanente se redistribuye siguiendo las nuevas líneas de corriente definidas por la geometría y los nuevos flujos. La simetría final se alcanza tras operar la segunda bomba capilar durante aproximadamente 500 segundos. La cantidad de colorante presente puede controlarse con el tiempo de operación de la etapa de enfoque.

Los solvers `porousMicroTransport` y `electroMicroTransport` requieren como entrada los parámetros característicos del medio poroso: porosidad ($\phi = 0{,}69$), factor de constricción ($C = 2{,}6$) y factor de dispersión (s=30 µm) [Urteaga et al., 2018]. También se necesita la movilidad electroforética en flujo libre (μ_e) y el pKa de los componentes del electrolito. Estos datos se

obtuvieron de la base `electrolytes` y, en el caso de los colorantes, se ajustaron con los resultados experimentales, incorporando un factor de retardo cromatográfico específico (R_f).

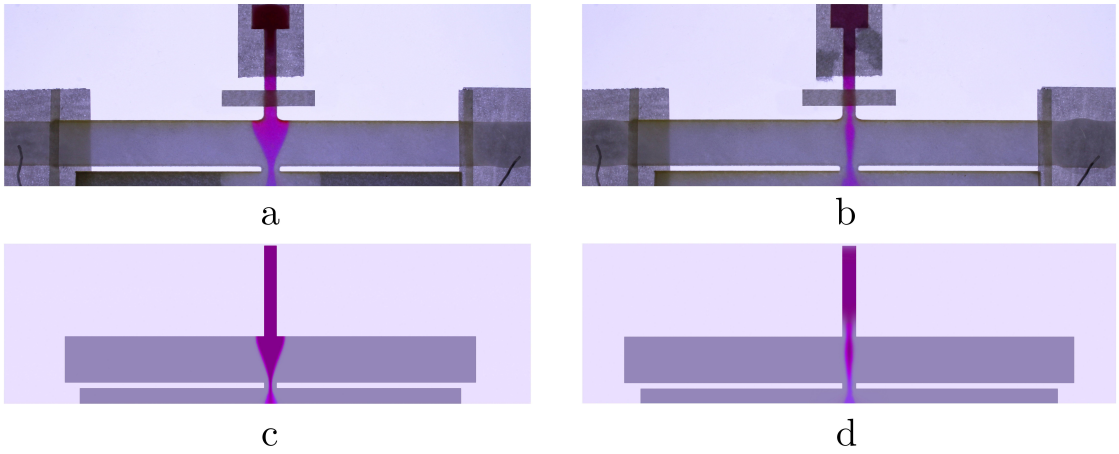

Figura 3.4: Etapas de validación del diseño propuesto. Resultados experimentales (A y B) vs simulaciones numéricas (C y D) en las etapas de inyección y enfoque.

En la simulación de la Fig. 3.4, se utilizaron los valores de μ_e y R_f reportados en la Tabla 3.3 para el colorante Tartrazina.

Las diferencias entre los resultados experimentales y simulados se deben a las incertidumbres en los parámetros macroscópicos del medio poroso. Aún así, las formas obtenidas en cada etapa son similares, lo que confirma la utilidad del diseño asistido por simulación numérica para reducir tiempos de desarrollo y número de prototipos experimentales.

3.3.2. Electroforesis en papel

Una vez completadas las etapas de inyección y enfoque, se aplicó una diferencia de potencial entre los extremos de los reservorios en la zona de detección. La simetría del dispositivo permite analizar moléculas con carga superficial positiva o negativa. Se analizaron cinco colorantes tanto en el dispositivo de papel como por CE. Los valores obtenidos y sus incertidumbres se presentan en la Tabla 3.3. La reproducibilidad se probó al menos cinco veces con Tartrazina a pH 5.5, observándose una dispersión menor al 7 %, coherente con la reproducibilidad típica de e-μPADs [Schaumburg et al., 2018a]. Las incertidumbres reportadas son la desviación estándar de los valores medidos (se asignó un 10 % a los colorantes medidos solo una vez).

Como ejemplo, se muestra la dinámica de la Tartrazina. En la Fig. 3.5A se observa el dispositivo durante la carrera electroforética a $t = 300$ s. La Fig. 3.5B muestra las curvas procesadas en $t = 0$ (azul) y $t = 300$ s (amarillo). La reconstrucción 2D del experimento se presenta en la Fig. 3.5C , donde el eje horizontal indica la posición y el vertical el tiempo. Su contraparte numéri-

ca se muestra en la Fig. 3.5D . La dispersión experimental es mayor que la simulada, posiblemente por diferencias en la movilidad efectiva de la molécula en el sustrato poroso. Factores como afinidad a las fibras, dispersión eléctrica y mecánica, y efectos de borde pueden contribuir, aunque no suelen afectar significativamente a canales abiertos o microchips.

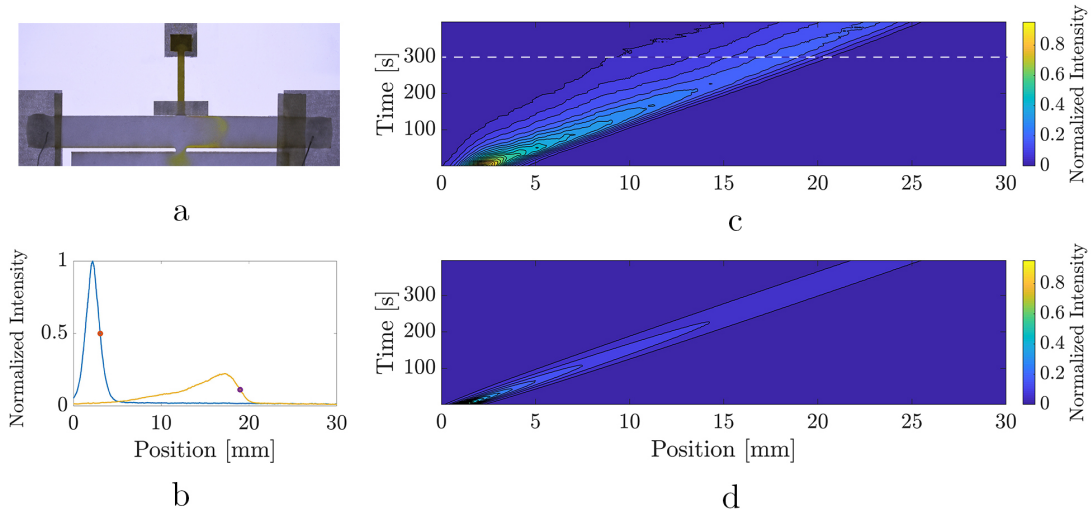

Figura 3.5: Resultados experimentales y numéricos para la electroforesis en papel de Tartrazina. a) Dispositivo operando a $t = 300$ s; b) Curvas procesadas para $t = 0$ s (azul) y $t = 300$ s (amarillo); c) Reconstrucción 2D experimental (posición vs tiempo); d) Resultado numérico correspondiente.

3.3.2.1. Cromatografía en papel

Para cuantificar el efecto de la afinidad de los colorantes a las fibras, se realizaron experimentos cromatográficos con las mismas concentraciones que en las corridas electroforéticas. Se observaron patrones de color ligeramente irregulares, ya que el avance en los bordes es más lento debido a la evaporación. Se midió un valor de L_{dye} para el colorante en el centro de la tira y un valor de L_{buffer} para el buffer. La pendiente del ajuste lineal de la posición del frente de colorante y buffer determina el factor de retardo R_f. Los valores de R_f se midieron para dos BGEs a pH 5.5 y 9.0, observándose diferencias según el pH. Estos resultados se presentan en la Tabla 3.3.

3.3.3. Validación del modelo

Para evaluar la influencia del medio poroso sobre las movilidades electroforéticas de los colorantes, se compararon las movilidades en papel y en canal abierto, como se muestra en la Fig. 3.6. Se realizó un ajuste lineal por mínimos cuadrados para los valores obtenidos de cada colorante a ambos valores de pH, siguiendo la relación lineal entre μ_p^{eff} y μ_e. Es importante destacar que para la regresión lineal se consideró un único parámetro libre (la pendiente de la función lineal sin

término independiente). Este parámetro es $\frac{\phi}{C}$, dado que todos los demás términos fueron medidos en este trabajo o tomados de la literatura [Franck et al., 2021].

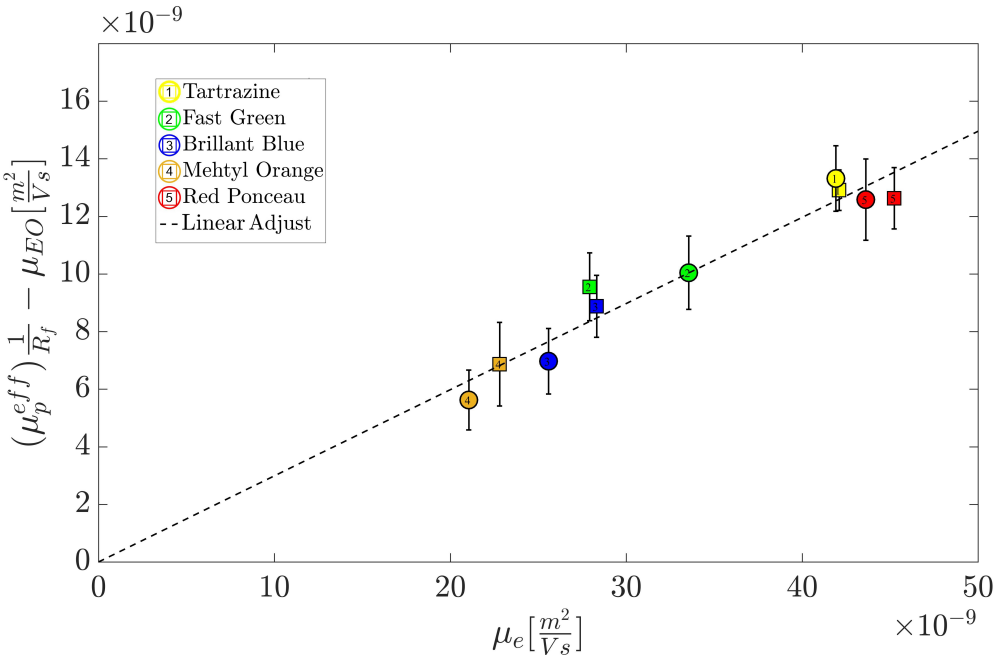

Figura 3.6: Validación experimental del modelo de movilidades electroforéticas en sustratos porosos. Se midieron las movilidades en canal abierto y en papel para distintos colorantes a dos valores de pH. Los cuadrados corresponden a pH=5.5 y los círculos a pH=9.0. La línea punteada representa el ajuste lineal por mínimos cuadrados a todos los datos con un único parámetro libre.

Sustancia	μ_e $10^{-9}\frac{m^2}{Vs}$		μ_p^{eff} $10^{-9}\frac{m^2}{Vs}$		R_f	
	pH=5.5	pH=9.0	pH=5.5	pH=9.0	pH=5.5	pH=9.0
Tartrazina	-42.1 ± 0.2	-41.9 ± 0.3	-9.2 ± 0.6	-8.6 ± 0.9	0.75 ± 0.02	0.68 ± 0.03
Fast Green FCF	-27.8 ± 0.1	-33.5 ± 0.2	-8.8 ± 1	-9.4 ± 1	0.98 ± 0.03	1 ± 0.07
Brillant Blue	-27.6 ± 0.1	-25.6 ± 0.2	-7.6 ± 0.8	-5.7 ± 0.6	0.92 ± 0.02	0.93 ± 0.04
Naranja de metilo	-21.9 ± 0.1	-21 ± 0.2	-1.6 ± 0.2	-1.7 ± 0.1	0.27 ± 0.02	0.35 ± 0.03
Rojo Ponceau	-45.3 ± 0.2	-43.6 ± 0.2	-10 ± 1	-11.4 ± 1.1	0.83 ± 0.03	0.97 ± 0.1

Tabla 3.3: Movilidades electroforéticas en canal abierto y en sustratos de papel, y factor de retención de distintos colorantes a dos valores de pH.

Los resultados mostrados en la Fig. 3.6 corroboran la hipótesis de que existe una relación lineal entre la movilidad efectiva medida en el papel (μ_p^{eff}) y μ_e, y que dicha relación depende únicamente de las características del medio poroso (es decir, de $\frac{\phi}{C}$). Una consecuencia práctica muy importante de la validación de este modelo es que μ_p^{eff} puede obtenerse directamente a partir de μ_e cuando se conocen ϕ y C para el sustrato y se mide R_f para el colorante en dicho sustrato.

La correlación propuesta es válida siempre que el BGE sea el mismo tanto en el canal abierto como en el medio poroso.

Para la regresión lineal mostrada, el valor obtenido de C es $2{,}3 \pm 0{,}1$, que es similar a valores obtenidos previamente mediante experimentos independientes basados en imbibición de agua, flujo impulsado por presión y conductividad eléctrica (ver apéndice B).

3.4. Detección de glifosato en un e-μPAD

3.4.1. Optimización de la detección colorimétrica

La detección colorimétrica se basa en la competencia entre el GlyP y PV por Cu^{2+}, formando GlyP complejos más estables que los de PV [Yadav and Zelder, 2021]. Esto genera un cambio de color de azul a amarillo, lo que permite la detección de GlyP.

$$\mathrm{PV} + 2\,\mathrm{Cu}^{2+} \rightleftharpoons [\mathrm{PV}]_{\text{azul}} \xrightarrow{+\mathrm{GlyP}} \mathrm{PV}_{\text{amarillo}} + [\mathrm{GlyP} - \mathrm{Cu}^{2+}]$$

La curva de calibración mostró un rango lineal de 1 a 60 µM. El límite de detección alcanzado fue de aproximadamente 1 µM por espectroscopía UV/Vis y 15 µM por detección visual.

3.4.1.1. Pruebas en sustratos porosos

En el papel de celulosa, no se observó cambio de color, lo que sugiere una fuerte adsorción de GlyP al sustrato, probablemente debido a interacciones con grupos –OH y O^- [de Aguiar Filho et al., 2021, Graf et al., 2022, Wimmer B. and C., 2022].

En nitrocelulosa se observó el cambio de color esperado, pero se presentó el efecto “anillo de café”, que se debe a que el solvente se evapora más rápido en el centro de la tira, lo que genera un gradiente de concentración [Zheng et al., 2021]. El EOF en este material es elevado (ver apéndice A), por lo que se añadió PVP para suprimir este flujo.

En placas TLC RP-18 W, la descomposición del complejo [PV] fue evidente por la pérdida del color azul y la aparición del color amarillo del PV libre.

Por lo tanto, se seleccionó la nitrocelulosa como soporte sólido para los experimentos posteriores.

3.4.2. Optimización numérica del electrolito para ITP

Se realizaron simulaciones numéricas para identificar las combinaciones de electrolitos más adecuadas para experimentos de ITP en papel. Se analizaron diferentes combinaciones de LE y de

TE, considerando el pH óptimo para la detección colorimétrica del GlyP, los factores de preconcentración alcanzados, la migración relativa de GlyP y el reactivo PV para asegurar complejación competitiva, y la influencia de los electrolitos sobre la estabilidad del complejo con PV.

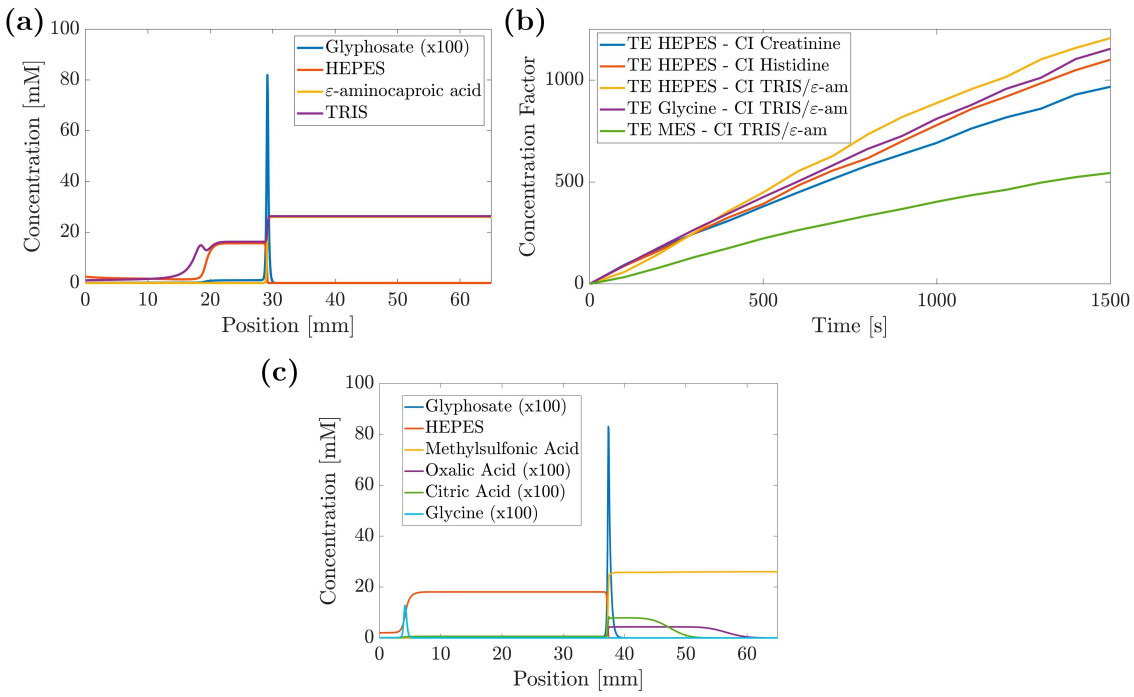

Figura 3.7: Resultados de simulaciones numéricas para optimizar combinaciones de electrolitos en ITP en papel. **(a)** Distribución de GlyP usando HEPES como TE, TRIS/ε-aminocaproico como CI y HCl como LE, a los 900 s. **(b)** Factores de preconcentración para diferentes combinaciones en función del tiempo. **(c)** Efectos de matriz con glicina, ácido oxálico y ácido cítrico, usando ácido metilsulfónico como LE.

La Fig. 3.7 muestra los resultados obtenidos. En (a) se observa un pico agudo de GlyP preconcentrado a partir de 1 µM hasta aproximadamente 820 µM. En (b) se comparan los factores de preconcentración para todas las combinaciones de electrolitos LE y TE, destacando un rendimiento inferior con MES como TE. En (c) se evaluaron efectos de matriz: la glicina no se incluye en el stack de ITP, y los ácidos oxálico y cítrico se separan adecuadamente de GlyP usando ácido metilsulfónico como LE, aunque con un leve descenso en el factor de preconcentración respecto a HCl. Por esta razón, se seleccionó HCl como LE para los experimentos, y se propone el sistema con ácido metilsulfónico para muestras ambientales complejas.

3.4.3. Verificación de la separación mediante ITP-UV

Para verificar la migración relativa del GlyP, el complejo [PV] y el PV libre, se reprodujo el sistema establecido de ITP sobre papel en un equipo comercial de CE. El capilar fue inicialmente

llenado con el LE, que contenía el complejo [PV], y posteriormente se introdujo el TE mediante presión. Al aplicar la tensión, se estableció un ITP dentro del capilar.

Los electroferogramas obtenidos demostraron una exitosa reproducción de la separación ITP para concentraciones de 1 y 2 µM de GlyP en el TE. La detección del GlyP se realizó de manera indirecta mediante la absorción UV del PV libre, liberado tras la disociación del complejo [PV] en presencia de GlyP [Yadav and Zelder, 2021]. Para ello, se monitoreó la absorción a 596 nm para el complejo [PV] y a 444 nm para el PV libre. Se observó una preconcentración de GlyP proveniente del TE, que se acumula en el frente del stack de ITP. Si bien la separación es sensible a variaciones del EOF debido al recubrimiento dinámico, no se realizaron ajustes adicionales para optimizarlo. Finalmente, se observó una disminución gradual de la línea base atribuida a la baja estabilidad del complejo en el medio buffer, así como una reducción en la señal en ambas longitudes de onda, causada por la preconcentración de impurezas antes de la llegada del GlyP.

3.4.4. Electroforesis sobre papel

3.4.4.1. Electroforesis capilar sobre papel

Se aplicaron 20 µL de solución de [PV] a la derecha de una línea imaginaria en el centro de la tira. Luego, se agregaron 10 µL de BGE y 20 µL de GlyP a la izquierda. Una vez llenados ambos reservorios con solución BGE, se aplicó un campo eléctrico de $1500\,\mathrm{V\,m^{-1}}$. Bajo estas condiciones, el GlyP migró hacia el cátodo con mayor velocidad que [PV], alcanzando la banda del complejo colorimétrico. Esto dio lugar a la formación del tinte libre amarillo y del complejo glifosato-cobre.

La curva de calibración mostró una saturación a partir de aproximadamente 400 µM de GlyP, estableciendo el límite superior del rango lineal. Las diferencias respecto a la muestra de 1200 µM fueron insignificantes, lo que sugiere que el rango óptimo de detección fue entre 100 µM y 400 µM, utilizando una concentración inicial de 175 µM de [PV]. El análisis de imágenes se realizó de manera idéntica al empleado en los experimentos de ITP descritos en la Sección 3.4.4.2. Aunque se ensayaron concentraciones menores de GlyP, el valor de 50 µM estuvo por debajo del LOD, estimado en torno a 100 µM, por lo que esta técnica no resulta adecuada para muestras ambientales.

3.4.4.2. ITP sobre papel

La técnica pCE mostró un LOD elevado para GlyP de 100 µM, mientras que en experimentos por lotes se alcanzaron valores de 2,66 µM con detección por smartphone [Yadav and Zelder, 2021] y de 1 µM usando el espectrómetro UV/VIS de alta gama. Por ello, se reemplazó pCE por la técnica

ITP en papel, para permitir la preconcentración. Se realizaron experimentos con concentraciones de GlyP de 1, 2, 5 y 25 µM, más un blanco con buffer puro.

Durante cada experimento se analizaron imágenes seleccionando un área rectangular de 34 mm x 3,3 mm, como se muestra en la Fig. 3.8a para la concentración de 5 µM al tiempo inicial. En la imagen inicial puede verse claramente la zona azul del complejo [PV] en LE, y una franja azul más intensa donde el TE con GlyP se encuentra con el [PV], debido al efecto de anillo de café.

A los 15 minutos de aplicar un voltaje de 400 V, se observa una clara preconcentración de GlyP, también en la Fig. 3.8a. Se identifican distintas zonas en la tira (ver Fig. 2.5c): i) zona de GlyP en TE, ii) zona mixta con complejo [GLP] y PV libre, iii) zona de [PV] en LE. La mezcla de compuestos azules y amarillos dificulta una evaluación visual directa.

Para un análisis completo, se construyeron matrices espacio-temporales para cada canal rojo-verde-azul (RGB), promediando verticalmente las intensidades del área analizada en cada imagen, y apilándolas temporalmente (Fig. 3.8b). Esto permite visualizar la dinámica del sistema en una única imagen.

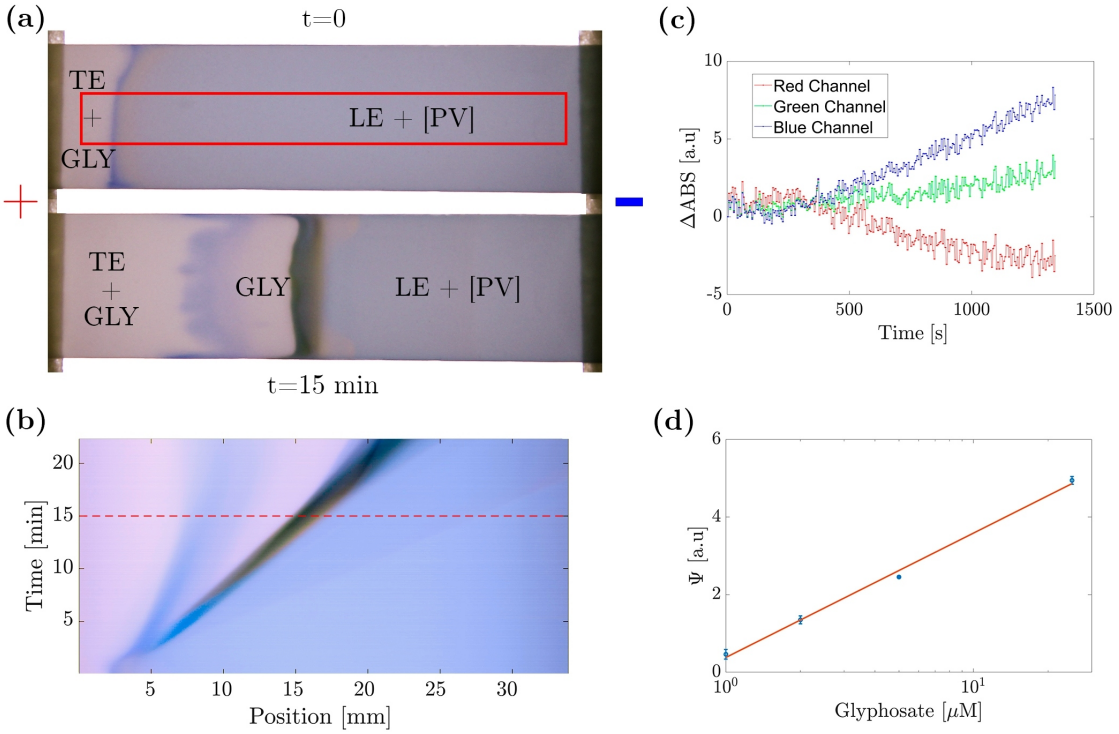

Figura 3.8: Resultados de detección de GlyP en el e-µPAD mediante ITP con detección colorimétrica. **(a)** Fotografías al inicio y a los 15 minutos, con el área de análisis en rojo. **(b)** Matriz espacio-temporal mostrando la dinámica del sistema. La línea punteada indica la imagen promedio vertical (a), en t=15 min. **(c)** Valores de ΔABS integrados espacialmente, por canal, a lo largo del tiempo. **(d)** Curva de calibración para múltiples concentraciones de GlyP (1, 2, 5 y 25 µM) usando el índice de absorción integrada Ψ.

La intensidad de cada canal RGB sigue la ley de Beer-Lambert:

$$I^{RGB}(x,t) = I_0^{RGB}(x)e^{-(\alpha_0+\alpha_{[PV]})d}$$

donde $I_0^{RGB}(x)$ es la intensidad de la luz de fondo, α_0 y $\alpha_{[PV]}$ los coeficientes de absorción del sustrato y del complejo [PV], respectivamente, y h el espesor del sustrato. Como $\alpha_{[PV]}h = \beta^{RGB}[C]_{[PV]}(t)$, se obtiene:

$$\log(I(x,t)) = \log(I_0(x)) - \alpha_0 h + \beta^{RGB}[C]_{[PV]}(t)$$

Restando esta expresión en t y en t_0, se elimina la influencia de la luz incidente y del sustrato:

$$\Delta ABS^{RGB}(x,t) = \log(I(x,0)) - \log(I(x,t)) = \beta^{RGB}([C]_{[PV]}(t) - [C]_{[PV]}(0))$$

El complejo [PV] absorbe preferentemente en rojo y el PV libre en azul, por lo que ΔABS^R es proporcional al [PV] complejo y ΔABS^B al PV libre. En presencia de GlyP se incrementa ΔABS^B y disminuye ΔABS^R. Esto se muestra en la Fig. 3.8c para $5\,\mu$M, donde ΔABS^R crece linealmente y ΔABS^B disminuye.

Se construyó una curva de calibración usando el índice de diferencia de absorción integrada: $\Psi = \int_0^{t_{ref}} (\Delta ABS^B - \Delta ABS^R)\, dt$, con $t_{ref} = 900$ s. En la Fig. 3.8d se presenta Ψ con barras de error y ajuste lineal logarítmico.

3.4.4.3. Validación de la preconcentración

La validación del factor de preconcentración de GlyP en ITP en papel se realizó en dos etapas. Primero, se efectuó una calibración depositando soluciones de GlyP a distintas concentraciones sobre nitrocelulosa. Luego de secarse, el GlyP fue extraído y cuantificado mediante CE-MS, utilizando como estándar interno glifosato-2-^{13}C a una concentración conocida de $6\,\mu$M. La comparación entre la señal de GlyP extraído y la del estándar mostró una eficiencia de extracción de aproximadamente 50 %.

En una segunda etapa, se llevó a cabo un experimento de ITP en papel con una concentración inicial de GlyP de $1\,\mu$M. La tira de nitrocelulosa se dividió en cinco segmentos, los cuales se analizaron por CE-MS. La mayor concentración se detectó en la zona central, donde la relación de señales entre GlyP y el estándar fue aproximadamente 15. Como el estándar estaba presente a $6\,\mu$M, esto indica que la concentración local de GlyP alcanzó aproximadamente $90\,\mu$M.

Teniendo en cuenta la eficiencia de extracción del 50 %, se estima que la concentración real de GlyP en el papel fue del orden de $180\,\mu$M, lo que representa el factor de preconcentración

alcanzado. Este valor es una estimación conservadora, ya que localmente podrían alcanzarse concentraciones aún mayores.

Capítulo 4

Conclusiones

En esta sección se desarrollan las conclusiones que se han obtenido a través del desarrollo de cada uno de los objetivos específicos de esta tesis, mencionados en la sección 1.1.2.

1. Caracterizar sustratos porosos para mejorar modelos computacionales existentes.

La caracterización de sustratos porosos llevada a cabo en esta tesis permitió mejorar los modelos computacionales empleados en el diseño y simulación de dispositivos electroforéticos microfluídicos de papel. Mediante mediciones precisas del flujo electroosmótico en tres tipos de papel, se obtuvo un parámetro representativo de cada sustrato que resultó fundamental tanto para su selección en una aplicación específica como para integrar esta información al modelo numérico mediante la estimación del potencial ζ_p. Además, el desarrollo de un modelo multifísico facilitó la estimación de parámetros estructurales esenciales, como la porosidad y la tortuosidad, necesarios para representar fielmente el transporte en medios porosos. Este modelo multifísico se construyó a partir del uso de una distribución de tamaño de poros adecuada, que sólo requiere de dos parámetros experimentales para quedar completamente determinada. De esta manera, se obtiene una descripción más detallada de la morfología del sustrato sin incorporar una complejidad excesiva en su representación. Complementariamente, la medición de movilidades electroforéticas permitió ampliar la base de datos de analitos relevantes en e-µPADs, mejorando la capacidad predictiva de los modelos y contribuyendo al diseño de sistemas analíticos más robustos y eficientes.

2. Diseñar métodos y dispositivos analíticos electroforéticos basados en papel a través del uso de modelos computacionales existentes.

A través de la integración de modelos computacionales con experimentación, se desarrollaron métodos analíticos y dispositivos electroforéticos en papel con un enfoque racional y optimizado. En particular, en la evaluación de movilidades electroforéticas en medios porosos se aplicaron dos solvers complementarios: uno para el llenado capilar del dispositivo (`porousMicroTransport`) y otro para simular el transporte electroforético de los analitos (`electroMicroTransport`). Esta estrategia permitió interpretar adecuadamente los resultados experimentales y sentó las bases para avanzar hacia diseños más complejos. En el caso del dispositivo orientado a la detección de glifosato, estas herramientas numéricas fueron utilizadas para guiar decisiones clave de diseño y operación, lo que permitió implementar una técnica de preconcentración isotacoforética efectiva, de bajo costo y con buena reproducibilidad. De este modo, los modelos existentes no solo sirvieron como apoyo teórico, sino como una plataforma central para el diseño y validación de sistemas analíticos funcionales. Estos desarrollos son de código abierto y están disponibles para que la comunidad científica pueda utilizarlos y adaptarlos directamente a sus propias investigaciones.

3. Fabricar y probar los dispositivos diseñados en condiciones de laboratorio.

Los dispositivos diseñados se fabricaron empleando técnicas de microfabricación tradicionales, con control preciso sobre dimensiones y propiedades físicas para asegurar su correcto funcionamiento. Las pruebas experimentales, realizadas con equipamiento avanzado, confirmaron la eficacia para la medición de movilidad electroforética en colorantes y para la preconcentración isotacoforética de glifosato para su posterior detección. En particular, en la tesis se desarrollaron dos técnicas experimentales novedosas para medir el EOF y la movilidad electroforética de colorantes en papeles, las cuales permiten obtener con alta precisión coeficientes fundamentales que la comunidad científica interesada en el tema requiere para avanzar en sus investigaciones. Los resultados evidenciaron que los dispositivos operan conforme a los principios planteados en el diseño, mostrando reproducibilidad y sensibilidad adecuadas para aplicaciones analíticas. La combinación de tecnologías de fabricación y métodos de caracterización avanzados garantizó un desempeño robusto y confiable bajo condiciones controladas de laboratorio. Este proceso permitió establecer un conjunto de técnicas y metodologías que no solo validan los dispositivos desarrollados, sino que también sientan las bases para el desarrollo y diversificación de futuras aplicaciones basadas en plataformas e-µPAD, ampliando su potencial hacia nuevos campos de análisis y diagnóstico.

4. Evaluar diferentes métodos de detección de acuerdo a las características de los analitos, los métodos de separación y el campo de aplicación del dispositivo.

Se evaluaron diversas técnicas electroforéticas para la separación y detección de analitos en medios porosos, considerando sus características particulares, los métodos de separación disponibles y el ámbito de aplicación de los dispositivos. En este proceso, los estudios con colorantes constituyeron una base fundamental para el desarrollo de algoritmos computacionales de análisis de imágenes que permitieron extender la metodología a analitos más complejos, como la medición indirecta de glifosato mediante pirocatecol violeta. Asimismo, se priorizó el uso de técnicas de detección accesibles y de bajo costo, como la captura de imágenes digitales, para garantizar la viabilidad práctica de los dispositivos. Además, se compararon estos métodos con técnicas analíticas de alta calidad y eficiencia, como la electroforesis capilar acoplada a espectrometría de masas, encontrando que no se observaron pérdidas significativas en sensibilidad ni precisión. En el caso específico del detector de glifosato, tras evaluar múltiples métodos electroforéticos mediante la herramienta computacional `electroMicroTransport`, la isotacoforesis se destacó por ofrecer el mejor compromiso entre capacidad de preconcentración y tiempo de detección, consolidándose como la técnica más adecuada para este analito en el contexto estudiado. Finalmente, es importante destacar la relevancia de contar con un método de detección sensible y de bajo costo para glifosato, que, según los resultados obtenidos en esta tesis, es factible y puede contribuir significativamente a aplicaciones ambientales.

4.1. Publicaciones y presentaciones realizadas vinculadas a la tesis

En el marco de esta tesis se han realizado diversas publicaciones y presentaciones que contribuyeron a la difusión y validación de los resultados obtenidos. Estas incluyen artículos con referato en revistas internacionales, donde se presentaron los avances y hallazgos, así como presentaciones en congresos nacionales que permitieron discutir y contrastar los resultados con la comunidad científica especializada.

- G. S. Gerlero, S. Márquez Damián, F. Schaumburg, N. Franck, P. A. Kler. Numerical simulations of paper-based electrophoretic separations with open-source tools. *Electrophoresis*, 42(16), 1543–1551, 2021.

- G. S. Gerlero, Z. I. Guerenstein, N. Franck, C. L. A. Berli, P. A. Kler. Comprehensive numerical prototyping of paper-based microfluidic devices using open-source tools. *Talanta Open*, 10(100350), 100350, 2024.

- N. Franck, P. A. Kler, R. Urteaga. Numerical prototyping of paper-based isotachophoresis.

Sesión: Flujo y transporte multifásico en medios porosos y microescala. Exposición en congreso MECOM - Congreso Argentino de Mecánica Computacional. Universidad Nacional de Resistencia, Chaco. 19(38):761, 2021.

- N. Franck, G. S. Gerlero, F. Schaumburg, R. Urteaga, P. A. Kler. Design of an Electrophoretic Device for Dye Characterization. Sesión: Flujo y transporte multifásico en medios porosos y microescala. Exposición en congreso MECOM - Congreso Argentino de Mecánica Computacional. Universidad Nacional del Sur, Bahia Blanca, Buenos Aires, 2022.

- N. Franck, G. S. Gerlero, F. Schaumburg, R. Urteaga, P. A. Kler. Development of a paper-based microfluidic device for electrophoretic characterization of dyes. Exposición en congreso MUFA - Congreso Argentino de Microfluidica. CNEA, Capital Federal, Buenos Aires, 2022.

- N. Franck, P. A. Kler, R. Urteaga. Design of a pre-concentrator paper-based microfluidic device with variable cross-sections. Exposición en congreso MECOM - Congreso Argentino de Mecánica Computacional. Universidad Nacional de Concordia, Entre Rios, 2023.

4.2. Trabajos a futuro

Una dirección relevante para el desarrollo futuro consiste en la extensión del solver `electroMicroTransport` mediante la incorporación de reacciones químicas acopladas al transporte electroforético. Esta capacidad resulta fundamental para el modelado de una amplia variedad de procesos de interés en microfluídica y química analítica. Entre los casos con validación experimental disponibles se encuentra el dispositivo desarrollado para la detección de GlyP, basado en la reacción con PV. La inclusión de estas reacciones permitirá simular de forma integrada dispositivos funcionales, así como explorar nuevas configuraciones experimentales orientadas a la detección selectiva de especies químicas.

Asimismo, se identifica como una línea estratégica la integración de las herramientas `electroMicroTransport` y `porousMicroTransport`. Esta fusión posibilitaría el tratamiento numérico de sistemas que combinan flujo electroforético, medios porosos no saturados y cinética química, actualmente modelados en etapas desacopladas. Tal desarrollo permitiría una descripción más amplia de fenómenos complejos en contextos experimentales realistas.

Adicionalmente, se prevé la aplicación de las herramientas desarrolladas al diseño y optimización de plataformas para electroforesis y detección de proteínas, como las implementadas en técnicas del tipo *Western Blot* en dispositivos microfluídicos. En particular, trabajos recientes de-

muestran el uso de medios porosos como geles de agarosa, para la separación y posterior inmunodetección. Las metodologías numéricas abordadas en esta tesis poseen el potencial de contribuir al diseño racional de estos sistemas, evaluando el impacto de la geometría, las propiedades del medio y las condiciones de operación. Estas líneas forman parte del plan de trabajo posdoctoral del autor.

Bibliografía

M. Alava, M. Dubé, and M. Rost. Imbibition in disordered media. *Adv Phys*, 53(2):83–175, Mar. 2004.

I. Ali, O. M. L. Alharbi, and M. M. Sanagi. Nano-capillary electrophoresis for environmental analysis. *Environ Chem Lett*, 14:79–98, 2015. doi: 10.1007/s10311-015-0547-x.

G. Álvarez, L. Montero, L. Llorens, M. Castro-Puyana, and A. Cifuentes. Recent advances in the application of capillary electromigration methods for food analysis and foodomics. *Electrophoresis*, 39:136–159, 2017. doi: 10.1002/elps.201700321.

R. An, Y. Man, S. Iram, E. Kucukal, M. N. Hasan, Y. Huang, U. Goreke, A. Bode, A. Hill, K. Cheng, Z. Sekyonda, S. P. Ahuja, J. A. Little, M. Hinczewski, and U. A. Gurkan. Point-of-care microchip electrophoresis for integrated anemia and hemoglobin variant testing. *Lab on a Chip*, 21(20):3863–3875, 2021. ISSN 1473-0189. doi: 10.1039/d1lc00371b. URL `http://dx.doi.org/10.1039/D1LC00371B`.

G. Archie. The Electrical Resistivity Log as an Aid in Determining Some Reservoir Characteristics. *T Soc Petrol En AIME*, 146(01):54–62, 1942.

C. M. Benbrook. Trends in glyphosate herbicide use in the United States and globally. *Environmental Sciences Europe*, 28(3), Feb. 2016. ISSN 2190-4715. doi: 10.1186/s12302-016-0070-0. URL `http://dx.doi.org/10.1186/s12302-016-0070-0`.

C. L. Berli, M. Mercuri, and M. G. Bellino. Modeling the abnormally slow infiltration rate in mesoporous films. *Phys Chem Chem Phys*, 19(3):1731–1734, 2017.

C. L. A. Berli, M. Piaggio, and J. Deiber. Modeling the zeta potential of silica capillaries in relation to the background electrolyte composition. *Electrophoresis*, 24:1587–1595, 2003.

D. A. Bikos and T. G. Mason. Band-collision gel electrophoresis. *Nat Commun*, 10, 2019. doi: 10.1038/s41467-019-11438-9.

A. V. Bruggen, M. He, K. Shin, V. Mai, K. Jeong, M. Finckh, and J. Morris. Environmental and health effects of the herbicide glyphosate. *Science of The Total Environment*, 616-617:255–268, Mar. 2018. doi: 10.1016/j.scitotenv.2017.10.309. URL https://doi.org/10.1016/j.scitotenv.2017.10.309.

A. E. Bussian. Electrical conductance in a porous medium. *Geophysics*, 48(9):1258–1268, 1983.

J. Cai, Y. Chen, Y. Liu, S. Li, and C. Sun. Capillary imbibition and flow of wetting liquid in irregular capillaries: A 100-year review. *Advances in Colloid and Interface Science*, 304:102654, 2022. ISSN 0001-8686.

F. A. Casado-Carmona, M. del Carmen Alcudia-León, R. Lucena, and S. Cárdenas. Portable stir membrane device for on-site environmental sampling and extraction. *J Chromatogr A*, 1606: 360359, 2019.

C. L. Chagas, F. R. de Souza, T. M. Cardoso, R. C. Moreira, J. A. da Silva, D. P. de Jesus, and W. K. Coltro. A fully disposable paper-based electrophoresis microchip with integrated pencil-drawn electrodes for contactless conductivity detection. *Anal Methods-UK*, 8(37):6682–6686, 2016.

H. Cremer, A. Tiselius, et al. Electrophoresis of protein on filter paper. *Biochem. Ztschr.*, 320: 273–283, 1950.

S. M. Damián, F. Schaumburg, and P. A. Kler. Open-source toolbox for electromigrative separations. *Comput Phys Commun*, 237:244–252, 2019.

P. Daniele. Copper(II) complexes of N-(phosphonomethyl)glycine in aqueous solution: a thermodynamic and spectrophotometric study. *Talanta*, 45(2):425–431, Dec. 1997. ISSN 0039-9140. doi: 10.1016/s0039-9140(97)00156-2. URL http://dx.doi.org/10.1016/S0039-9140(97)00156-2.

S. Q. de Aguiar Filho, A. M. F. Costa, A. K. dos Santos Pereira, G. S. Cavallini, and D. H. Pereira. Interaction of glyphosate in matrices of cellulose and diethylaminoethyl cellulose biopolymers: theoretical viewpoint of the adsorption process. *Journal of Molecular Modeling*, 27(9), Sept. 2021. ISSN 0948-5023. doi: 10.1007/s00894-021-04894-y. URL http://dx.doi.org/10.1007/s00894-021-04894-y.

J. M. de los Santos-Ramirez, P. G. Boyas-Chavez, A. Cerrillos-Ordoñez, M. Mata-Gomez, R. C. Gallo-Villanueva, and V. H. Perez-Gonzalez. Trends and challenges in microfluidic methods for protein manipulation—a review. *Electrophoresis*, 2023.

M. Dovhunová, M. Malỳ, P. Dubskỳ, G. S. Gerlero, and P. A. Kler. Generalized model of the linear theory of electromigration and its application to electrokinetic chromatography: Capillary zone electrophoretic systems with complex-forming equilibria. *J Chromatogr A*, 1610:460595, 2020.

A. Duda, Z. Koza, and M. Matyka. Hydraulic tortuosity in arbitrary porous media flow. *Phys. Rev. E Stat. Nonlin. Soft Matter Phys.*, 84(3 Pt 2):036319, Sept. 2011.

E. L. Durrum. Continuous electrophoresis and ionophoresis on filter paper1. *J Am Chem Soc*, 73 (10):4875–4880, 1951.

E. Elizalde, R. Urteaga, and C. L. A. Berli. Rational design of capillary-driven flows for paper-based microfluidics. *Lab Chip*, 15:2173–2180, 2015. doi: 10.1039/C4LC01487A.

E. Elizalde, R. Urteaga, and C. L. A. Berli. Precise capillary flow for paper-based viscometry. *Microfluid Nanofluid*, 20(10), 2016.

M. Ezzatabadipour and H. Zahedi. A novel method for streamline-based tortuosity calculation and investigation of obstacles shape effect on tortuosity in porous media with random elliptical obstacles using lattice boltzmann method. *Transport Porous Med*, 136(1):103–124, 2021.

F. T. Ferreira, K. A. Catalão, R. B. Mesquita, and A. O. Rangel. New microfluidic paper-based analytical device for iron determination in urine samples. *Analytical and Bioanalytical Chemistry*, 413:7463–7472, 2021. doi: 10.1007/s00216-021-03706-9.

N. Franck, F. Schaumburg, P. A. Kler, and R. Urteaga. Precise electroosmotic flow measurements on paper substrates. *Electrophoresis*, 42(7-8):975–982, 2021.

N. Franck, C. L. Berli, P. A. Kler, and R. Urteaga. Multiphysics approach for fluid and charge transport in paper-based microfluidics. *Microfluid Nanofluid*, 26:87, 2022.

B. Gaš. Peakmaster and Simul – Software tools for mastering electrophoresis. *TrAC Trends in Analytical Chemistry*, 165:117134, Aug. 2023. ISSN 0165-9936. doi: 10.1016/j.trac.2023.117134. URL `http://dx.doi.org/10.1016/j.trac.2023.117134`.

L. Ge, S. Wang, S. Ge, J. Yu, M. Yan, N. Li, and J. Huang. Electrophoretic separation in a microfluidic paper-based analytical device with an on-column wireless electrogenerated chemiluminescence detector. *Chem Commun*, 50(43):5699–5702, 2014.

G. S. Gerlero, S. M. Damián, and P. A. Kler. electromicrotransport v2107: Open-source toolbox for paper-based electromigrative separations. *Comput Phys Commun*, 269:108143, 2021a.

G. S. Gerlero, S. M. Damián, F. Schaumburg, N. Franck, and P. A. Kler. Numerical simulations of paper-based electrophoretic separations with open-source tools. *Electrophoresis*, 42:1543–1551, 2021b.

G. S. Gerlero, A. R. Valdez, R. Urteaga, and P. A. Kler. Validity of capillary imbibition models in paper-based microfluidic applications. *Transport Porous Med*, pages 1–20, Jan. 2022.

G. S. Gerlero, C. L. A. Berli, and P. A. Kler. Open-source high-performance software packages for direct and inverse solving of horizontal capillary flow. *Capillarity*, 6:31–40, 2023.

B. Ghanbarian, A. G. Hunt, R. P. Ewing, and T. E. Skinner. Universal scaling of the formation factor in porous media derived by combining percolation and effective medium theories. *Geophys Res Lett*, 41(11):3884–3890, 2014.

J. P. K. Gill, N. Sethi, A. Mohan, S. Datta, and M. Girdhar. Glyphosate toxicity for animals. *Environmental Chemistry Letters*, 16(2):401–426, Dec. 2017. doi: 10.1007/s10311-017-0689-0. URL `https://doi.org/10.1007/s10311-017-0689-0`.

J.-B. Gorce, I. J. Hewitt, and D. Vella. Capillary imbibition into converging tubes: beating washburn's law and the optimal imbibition of liquids. *Langmuir*, 32(6):1560–1567, 2016.

H. G. Graf, S. M. Biebl, L. Müller, C. Breitenstein, and C. Huhn. Capillary electrophoresis applied for the determination of acidity constants and limiting electrophoretic mobilities of ionizable herbicides including glyphosate and its metabolites and for their simultaneous separation. *Journal of Separation Science*, 45(5):1128–1139, Jan. 2022. ISSN 1615-9314. doi: 10.1002/jssc.202100952. URL `http://dx.doi.org/10.1002/jssc.202100952`.

W. Grassmann and K. Hannig. Ein einfaches verfahren zur kontinuierlichen trennung von stoffgemischen auf filterpapier durch elektrophorese. *Naturwissenschaften*, 37(17):397–397, 1950.

A. M. Haines, S. S. Tobe, H. J. Kobus, and A. Linacre. Properties of nucleic acid staining dyes used in gel electrophoresis. *Electrophoresis*, 36:941–944, 2015. doi: 10.1002/elps.201400496.

S. Hennig, Z. Shu, L. Gutzweiler, P. Koltay, F. Stetten, R. Zengerle, and S. M. Früh. Paper-based open microfluidic platform for protein electrophoresis and immunoprobing. *Electrophoresis*, 43:621–631, 2021. doi: 10.1002/elps.202100327.

D. C. Herrick and W. D. Kennedy. Electrical efficiency—a pore geometric theory for interpreting the electrical properties of reservoir rocks. *Geophysics*, 59(6):918–927, 1994.

T. Hirokawa, M. Nishino, N. Aoki, Y. Kiso, Y. Sawamoto, T. Yagi, and J.-I. Akiyama. Table of isotachophoretic indices: I. simulated qualitative and quantitative indices of 287 anionic substances in the range ph 3–10. *J Chromatogr A*, 271:1–106, 1983.

C. Huhn. More and enhanced glyphosate analysis is needed. *Analytical and Bioanalytical Chemistry*, 410(13):3041–3045, Mar. 2018. doi: 10.1007/s00216-018-1000-3. URL `https://doi.org/10.1007/s00216-018-1000-3`.

A. V. Jager, F. G. Tonin, and M. F. M. Tavares. Optimizing the separation of food dyes by capillary electrophoresis. *J Sep Sci*, 28:957–965, 2005. doi: 10.1002/jssc.200500039.

S. Jaitpal, P. Naik, S. Chakraborty, S. Banerjee, and D. Paul. Exploring the concentration-dependent transport and the loss of rhodamine b, tartrazine, methylene blue, and amaranth dyes in common paperfluidic substrates. *Res Surf Inter*, 6:100034, 2022. doi: 10.1016/j.rsurfi.2021.100034.

T. K. Khurana and J. G. Santiago. Preconcentration, separation, and indirect detection of nonfluorescent analytes using fluorescent mobility markers. *Anal Chem*, 80:279–286, 2008.

A. Kocyła, A. Pomorski, and A. Krężel. Molar absorption coefficients and stability constants of Zincon metal complexes for determination of metal ions and bioinorganic applications. *Journal of Inorganic Biochemistry*, 176:53–65, Nov. 2017. ISSN 0162-0134. doi: 10.1016/j.jinorgbio.2017.08.006. URL `http://dx.doi.org/10.1016/j.jinorgbio.2017.08.006`.

C.-T. Kung, C.-Y. Hou, Y.-N. Wang, and L.-M. Fu. Microfluidic paper-based analytical devices for environmental analysis of soil, air, ecology and river water. *Sensor Actuat B-Chem*, 301: 126855, 2019.

H. G. Kunkel and A. Tiselius. Electrophoresis of proteins on filter paper. *J Gen Physiol*, 35(1): 89–118, 1951.

K.-S. Lee, M. J. A. Shiddiky, S.-H. Park, D.-S. Park, and Y.-B. Shim. Electrophoretic analysis of food dyes using a miniaturized microfluidic system. *Electrophoresis*, 29:1910–1917, 2008. doi: 10.1002/elps.200700556.

V. Leung, A.-A. M. Shehata, C. D. Filipe, and R. Pelton. Streaming potential sensing in paper-based microfluidic channels. *Colloid Surf A*, 364(1-3):16–18, 2010.

R. Lucas. Ueber das Zeitgesetz des kapillaren Aufstiegs von Flüssigkeiten. *Colloid & Polymer Science*, 23(1):15–22, 1918.

H. E. L. Madsen, H. H. Christensen, C. Gottlieb-Petersen, A. F. Andresen, O. Smidsrød, C.-O. Pontchour, P. Phavanantha, S. Pramatus, B. N. Cyvin, and S. J. Cyvin. Stability constants of copper(II), zinc, manganese(ii), calcium, and magnesium complexes of N-(phosphonomethyl)glycine (glyphosate). *Acta Chemica Scandinavica*, 32a:79–83, 1978. ISSN 0904-213X. doi: 10.3891/acta.chem.scand.32a-0079. URL `http://dx.doi.org/10.3891/acta.chem.scand.32a-0079`.

V.-P. Mai, C.-H. Ku, and R.-J. Yang. Porosity estimation using electric current measurements for paper-based microfluidics. *Microfluid Nanofluid*, 23(4):1–10, 2019.

Z. Malá and P. Gebauer. Recent progress in analytical capillary isotachophoresis. *Electrophoresis*, 40(1):55–64, Aug. 2018. ISSN 1522-2683. doi: 10.1002/elps.201800239. URL `http://dx.doi.org/10.1002/elps.201800239`.

Z. Malá and P. Gebauer. Analytical isotachophoresis 1967–2022: From standard analytical technique to universal on-line concentration tool. *TrAC Trends in Analytical Chemistry*, 158:116837, Jan. 2023. ISSN 0165-9936. doi: 10.1016/j.trac.2022.116837. URL `http://dx.doi.org/10.1016/j.trac.2022.116837`.

R. Masoodi and K. M. Pillai. Darcy's law-based model for wicking in paper-like swelling porous media. *AIChE J*, 56(9):2257–2267, 2010.

M. Matyka, A. Khalili, and Z. Koza. Tortuosity-porosity relation in porous media flow. *Phys Rev E*, 78(2):026306, 2008.

J. Mettakoonpitak and C. S. Henry. Electrophoretic separations on parafilm-paper-based analytical devices. *Sensor Actuat B-Chem*, 273:1022–1028, 2018.

M. Mirzadeh, T. Zhou, M. A. Amooie, D. Fraggedakis, T. R. Ferguson, and M. Z. Bazant. Vortices of electro-osmotic flow in heterogeneous porous media. *arXiv preprint arXiv:2003.05974*, 2020.

S. Modha, C. Castro, and H. Tsutsui. Recent developments in flow modeling and fluid control for paper-based microfluidic biosensors. *Biosens Bioelectron*, page 113026, 2021.

B. Y. Moghadam, K. T. Connelly, and J. D. Posner. Isotachophoretic preconcenetration on paper-based microfluidic devices. *Analytical Chemistry*, 86(12):5829–5837, May 2014. doi: 10.1021/ac500780w. URL `https://doi.org/10.1021/ac500780w`.

S. Márquez Damián, F. Schaumburg, and P. A. Kler. Open-source toolbox for electromigrative separations. *Computer Physics Communications*, 237:244–252, Apr. 2019. ISSN 0010-4655. doi: 10.1016/j.cpc.2018.11.015. URL http://dx.doi.org/10.1016/j.cpc.2018.11.015.

E. W. Nery and L. T. Kubota. Sensing approaches on paper-based devices: a review. *Analytical and Bioanalytical Chemistry*, 405(24):7573–7595, Apr. 2013. ISSN 1618-2650. doi: 10.1007/s00216-013-6911-4. URL http://dx.doi.org/10.1007/s00216-013-6911-4.

V.-T. Nguyen, S. Song, S. Park, and C. Joo. Recent advances in high-sensitivity detection methods for paper-based lateral-flow assay. *Biosens Bioelectron*, 152:112015, 2020.

J.-C. Niu, T. Zhou, L.-L. Niu, Z.-S. Xie, F. Fang, F.-Q. Yang, and Z.-Y. Wu. Simultaneous pre-concentration and separation on simple paper-based analytical device for protein analysis. *Analytical and Bioanalytical Chemistry*, 410(6):1689–1695, Jan. 2018. ISSN 1618-2650. doi: 10.1007/s00216-017-0809-5. URL http://dx.doi.org/10.1007/s00216-017-0809-5.

H. Noh and S. T. Phillips. Metering the capillary-driven flow of fluids in paper-based microfluidic devices. *Anal Chem*, 82(10):4181–4187, 2010.

T. Novotnỳ and B. Gaš. Mathematical model of electromigration allowing the deviation from electroneutrality. *Electrophoresis*, 42:881–889, 2021.

P. M. Nowak, I. Biel, G. Kózka, M. Klag, and M. Woźniakiewicz. Influence of pH measurement inaccuracy on the values of acidity constant determined on the basis of electrophoretic and thermophoretic data. *Microchem J*, 181:107689, 2022. doi: 10.1016/j.microc.2022.107689.

E. Okada, T. Coggan, T. Anumol, B. Clarke, and G. Allinson. A simple and rapid direct injection method for the determination of glyphosate and AMPA in environmental water samples. *Analytical and Bioanalytical Chemistry*, 411(3):715–724, Dec. 2018. doi: 10.1007/s00216-018-1490-z. URL https://doi.org/10.1007/s00216-018-1490-z.

C. Oltramare, F. T. Weiss, P. Staudacher, O. Kibirango, A. Atuhaire, and C. Stamm. Pesticides monitoring in surface water of a subsistence agricultural catchment in Uganda using passive samplers. *Environmental Science and Pollution Research*, 30(4):10312–10328, Sept. 2022. ISSN 1614-7499. doi: 10.1007/s11356-022-22717-2. URL http://dx.doi.org/10.1007/s11356-022-22717-2.

J. V. Pagaduan, V. Sahore, and A. T. Woolley. Applications of microfluidics and microchip electrophoresis for potential clinical biomarker analysis. *Analytical and Bioanalytical Chemistry*,

407(23):6911–6922, Apr. 2015. ISSN 1618-2650. doi: 10.1007/s00216-015-8622-5. URL http://dx.doi.org/10.1007/s00216-015-8622-5.

A. Piovesan, R. Nicasy, T. Arens, B. Dequeker, J. Soete, C. Achille, R. Dochy, C. Parra-Cabrera, R. Ameloot, P. Verboven, and B. Nicolai. Multiscale modelling of capillary imbibition in 3d-printed porous microfluidic channels. *Microfluid Nanofluid*, 26(3):1–15, 2022.

K. Popov, H. Rönkkömäki, and L. H. J. Lajunen. Critical evaluation of stability constants of phosphonic acids (IUPAC Technical Report). *Pure and Applied Chemistry*, 73(10):1641–1677, Oct. 2001. ISSN 0033-4545. doi: 10.1351/pac200173101641. URL http://dx.doi.org/10.1351/pac200173101641.

R. Probstein. *Physicochemical Hydrodynamics. An Introduction*. Wiley-Interscience, 2nd edition, 2003.

A. Ramachandran and J. G. Santiago. Isotachophoresis: Theory and microfluidic applications. *Chemical Reviews*, 122(15):12904–12976, June 2022. doi: 10.1021/acs.chemrev.1c00640. URL https://doi.org/10.1021/acs.chemrev.1c00640.

M. Reyssat, L. Courbin, E. Reyssat, and H. A. Stone. Imbibition in geometries with axial variations. *J Fluid Mech*, 615:335–344, 2008.

T. Rosenfeld and M. Bercovici. 1000-fold sample focusing on paper-based microfluidic devices. *Lab Chip*, 14(23):4465–4474, 2014.

T. Rosenfeld and M. Bercovici. Amplification-free detection of dna in a paper-based microfluidic device using electroosmotically balanced isotachophoresis. *Lab Chip*, 18(6):861–868, 2018.

T. Rosenfeld and M. Bercovici. Dynamic control of capillary flow in porous media by electroosmotic pumping. *Lab Chip*, 19(2):328–334, 2019.

G. I. Salentijn, M. Grajewski, and E. Verpoorte. Reinventing (bio) chemical analysis with paper. *Anal Chem*, 90(23):13815–13825, 2018.

F. Schaumburg and C. L. Berli. Assessing the rapid flow in multilayer paper-based microfluidic devices. *Microfluid Nanofluid*, 23(8):1–10, 2019.

F. Schaumburg, P. A. Kler, and C. L. Berli. Numerical prototyping of lateral flow biosensors. *Sensors and Actuators B: Chemical*, 259:1099–1107, Apr. 2018a. ISSN 0925-4005. doi: 10.1016/j.snb.2017.12.044. URL http://dx.doi.org/10.1016/j.snb.2017.12.044.

F. Schaumburg, R. Urteaga, P. A. Kler, and C. L. Berli. Design keys for paper-based concentration gradient generators. *J Chromatogr A*, 1561:83–91, 2018b.

F. Schaumburg, C. Carrell, and C. S. Henry. Rapid bacteria detection at low concentrations using sequential immunomagnetic separation and paper-based isotachophoresis. *Anal Chem*, 2019.

F. Schaumburg, P. A. Kler, and C. L. Berli. Comprehensive model of electromigrative transport in microfluidic paper based analytical devices. *Electrophoresis*, 41(7-8):598–606, 2020a.

F. Schaumburg, P. A. Kler, C. S. Carrell, C. L. Berli, and C. S. Henry. USB powered microfluidic paper-based analytical devices. *Electrophoresis*, 41(7-8):562–569, 2020b. doi: 10.1002/elps.201900273.

F. Schaumburg, J. P. Vidocevich, G. S. Gerlero, N. Pujato, J. Macagno, P. A. Kler, and C. L. A. Berli. A free customizable tool for easy integration of microfluidics and smartphones. *Scientific Reports*, 12(1), May 2022. doi: 10.1038/s41598-022-13099-z. URL `https://doi.org/10.1038/s41598-022-13099-z`.

M. Schwientek, H. Rügner, S. Haderlein, W. Schulz, B. Wimmer, L. Engelbart, S. Bieger, and C. Huhn. Glyphosate contamination in European rivers not from herbicide application? Preprint (Version 3) available at Research Square, June 2024. URL `http://dx.doi.org/10.21203/rs.3.rs-3917957/v3`.

A. Sena-Torralba, R. Alvarez-Diduk, C. Parolo, H. Torné-Morató, A. Müller, and A. Merkoçi. Paper-based electrophoretic bioassay: Biosensing in whole blood operating via smartphone. *Anal Chem*, 93:3112–3121, 2021. doi: 10.1021/acs.analchem.0c04330.

R. Sharma and D. S. Ross. Kinetics of liquid penetration into periodically constricted capillaries. *J Chem Soc Faraday T*, 87(4):619–624, 1991.

F. Shen, M. Ai, Z. Li, X. Lu, Y. Pang, and Z. Liu. Pressure measurement methods in microchannels: advances and applications. *Microfluid and Nanofluid*, 25(5):1–31, 2021.

W. Su, X. Gao, L. Jiang, and J. Qin. Microfluidic platform towards point-of-care diagnostics in infectious diseases. *Journal of Chromatography A*, 1377:13–26, Jan. 2015. ISSN 0021-9673. doi: 10.1016/j.chroma.2014.12.041. URL `http://dx.doi.org/10.1016/j.chroma.2014.12.041`.

T. Tesfaye and A. Hussen. Microfluidic paper-based analytical device (μpad) fabricated by wax screen printing technique for the determination of nitrite and nitrate ion in water samples. *Microfluid Nanofluid*, 26(3):1–13, 2022.

J. C. Ulrich and P. L. Ferguson. Development of a sensitive direct injection LC-MS/MS method for the detection of glyphosate and aminomethylphosphonic acid (ampa) in hard waters. *Analytical and Bioanalytical Chemistry*, 413:3763–3774, 2021. doi: 10.1007/s00216-021-03324-5.

R. Urteaga, E. Elizalde, and C. L. A. Berli. Transverse solute dispersion in microfluidic paper-based analytical devices (μPADs). *Analyst*, 143:2259–2266, 2018. doi: 10.1039/c8an00149a.

A. L. Valle, F. C. C. Mello, R. P. Alves-Balvedi, L. P. Rodrigues, and L. R. Goulart. Glyphosate detection: methods, needs and challenges. *Environmental Chemistry Letters*, 17(1):291–317, Sept. 2018. ISSN 1610-3661. doi: 10.1007/s10311-018-0789-5. URL `http://dx.doi.org/10.1007/s10311-018-0789-5`.

E. W. Washburn. The dynamics of capillary flow. *Physical review*, 17(3):273, 1921.

P. Wei, L. Xiao, P. Hou, Q. Wang, and P. Wang. A novel Cu(II)-assisted peptide fluorescent probe for highly sensitive detection of glyphosate in real samples: real application in test strips and smartphone. *Analytical and Bioanalytical Chemistry*, 415(24):5985–5996, July 2023. doi: 10.1007/s00216-023-04869-3. URL `https://doi.org/10.1007/s00216-023-04869-3`.

B. C. Wimmer B. and H. C. Alternative Wege in der Glyphosatanalytik. *GIT Labor-Fachzeitschrift*, 4(66):28, June 2022. ISSN 0016-3538. URL `https://analyticalscience.wiley.com/content/magazine-do/wiley-analytical-science-magazine---june-2022`.

Z.-Y. Wu, F. Zhang, Z. Kuang, F. Fang, and Y.-Y. Song. Fast and sensitive colorimetric detection of pigments from beverages by gradient zone electrophoresis on a paper based analytical device. *Microchem J*, 179:107499, 2022.

C. Xu, W. Lin, and L. Cai. Demonstrating electrophoretic separation in a straight paper channel delimited by a hydrophobic wax barrier. *J Chem Educ*, 93(5):903–905, 2016.

P. Yadav and F. Zelder. Detection of glyphosate with a copper(II)-pyrocatechol violet based GlyPKit. *Analytical Methods*, 13(38):4354–4360, 2021. doi: 10.1039/d1ay01168e. URL `https://doi.org/10.1039/d1ay01168e`.

S. Yao and J. G. Santiago. Porous glass electroosmotic pumps: theory. *J Colloid Interf Sci*, 268 (1):133–142, 2003.

W.-B. Young. Analysis of capillary flows in non-uniform cross-sectional capillaries. *Colloid Surface A*, 234(1-3):123–128, 2004.

W. Zheng, K. Wang, H. Xu, C. Zheng, B. Cao, Q. Qin, Q. Jin, and D. Cui. Strategies for the detection of target analytes using microfluidic paper-based analytical devices. *Analytical and Bioanalytical Chemistry*, 413(9):2429–2445, Mar. 2021. doi: 10.1007/s00216-021-03213-x. URL `https://doi.org/10.1007/s00216-021-03213-x`.

A. A. Zukas and A. P. Breksa III. Extraction methods for analysis of citrus leaf proteins by two-dimensional gel electrophoresis. *J Chromatogr A*, 1078:201–205, 2005.

Anexos

En referencia a los artículos presentados a continuación en los Anexos A a D:

- N. Franck, F. Schaumburg, P.A. Kler, R. Urteaga. Precise electroosmotic flow measurements on paper substrates. *Electrophoresis*, 42(7–8): 975–982, 2021.
- N. Franck, C. L. A. Berli, P. A. Kler, R. Urteaga. Multiphysics approach for fluid and charge transport in paper-based microfluidics. *Microfluidics and Nanofluidics*, 26(11), 2022.
- N. Franck, L. Vera Candioti, G. S. Gerlero, R. Urteaga, P. A. Kler. A simple method for the assessment of electrophoretic mobility in porous media. *Electrophoresis*, 45(7–8), 589–598, 2023.
- N. Franck, P. Stopper, L. Ude, R. Urteaga, P. A. Kler, C. Huhn. Paper-based isotachophoretic preconcentration technique for low-cost determination of glyphosate. *Analytical and Bioanalytical Chemistry*, 416(29), 6745–6757, 2024.

el tesista asumió en todos ellos el rol de autor principal y declara haber realizado contribuciones esenciales en cada uno de ellos, particularmente en el modelado matemático, desarrollo de software, diseños experimentales, ejecución de los experimentos, validación y escritura de los trabajos; bajo la tutela del director y co-director de tesis y con las contribuciones de los otros co-autores de cada trabajo. El director y co-director de tesis avalan esta declaración.

_____	_____
Dr. Pablo A. Kler	Dr. Raul Urteaga
Director	Co-director

Anexo A

Precise electroosmotic flow measurements on paper substrates

El artículo presentado a continuación ha sido publicado en la revista **Electrophoresis**.

N. Franck, F. Schaumburg, P.A. Kler, R. Urteaga. Precise electroosmotic flow measurements on paper substrates. *Electrophoresis*, 42(7–8): 975–982, 2021. https://doi.org/10.1002/elps.202000271.

Precise electroosmotic flow measurements on paper substrates

Nicolás Franck[1], Federico Schaumburg[2], Pablo A. Kler[1,3], Raul Urteaga[4]

[1] CIMEC (Universidad Nacional del Litoral–CONICET), Colectora RN 168 Km 472, S3000GLN Santa Fe, Argentina

[2] INTEC (Universidad Nacional del Litoral–CONICET), Colectora RN 168 Km 472, S3000GLN Santa Fe, Argentina

[3] Departamento de Ingeniería en Sistemas de Información, Facultad Regional Santa Fe, Universidad Tecnológica Nacional, Lavaisse 610, Santa Fe, Argentina

[4] Instituto de Física del Litoral (IFIS Litoral, UNL–CONICET), Güemes 3450, S3000GLN Santa Fe, Argentina

Abstract

A novel method for electroosmotic flow (EOF) measurement on paper substrates is presented; it is based on dynamic mass measurements by simply using an analytical balance. This technique provides a more reliable alternative to other EOF measurement methods on porous media. The proposed method is used to increase the amount and quality of the available information about physical parameters that characterize fluid flow on microfluidic paper–based analytical devices (μPADs). Measurements were performed on some of the most frequently used materials for μPADs, i.e. Whatman #1, S&S and Muntktell 00A filter paper. Obtained experimental results are consistent with the few previously reported data, either experimental or numerical, characterizing EOF in paper substrates. Moreover, a thorough analysis is presented for the quantification of the different effects that affect the measurements such as Joule effect and evaporation. Experimental results enabled, for the first time, to establish well defined electroosmotic characteristics for the three substrates in terms of the magnitude of EOF as funtion of pH, enabling researchers to make a ra-

tional choice of the substrate depending on the electrophoretic technique to be implemented. The measurement method can be described as robust, reliable, and affordable enough for being adopted by researchers and companies devoted to electrophoretic µPADs and related technologies.

Keywords: Paper-based microfluidics, Electrophoresis, Electroosmosis, Whatman #1.

A.1. Introduction

Paper-based electrophoretic separations have renewed its relevance due to the contemporary expansion of paper-based microfluidic analytic devices (µPADs)[Salentijn et al., 2018]. Although several attempts were made in the mid 20th century for the separation of serum proteins [Cremer et al., 1950, Kunkel and Tiselius, 1951], and small inorganic molecules [Durrum, 1951, Grassmann and Hannig, 1950], the advantages later shown by capillary and gel-based separations interrupted the development of such techniques in paper substrates, for more than 70 years.

Hence, several research groups began developing electrophoretic µPADs (e-µPADs) in the last years. Paper-based electrophoretic separations have been demonstrated with different results in terms of separation efficiency and detection limits. For example paper zone electrophoresis has been proven for amino-acids [Ge et al., 2014] and small inorganic molecules [Xu et al., 2016, Chagas et al., 2016] as well as isotachophoresis for increasing the efficiency of lateral flow analysis [Moghadam et al., 2014, Rosenfeld and Bercovici, 2014]. However, µPADs in general and e-µPADs in particular suffer from poor repeatably, preventing this technology from finding new applications in sensitive fields like point-of-care (POC) or food safety. Such lack of reproducibility, is attached to the high scatter of the physical parameters that describe the substrates, and determine their behavior under fluid flow, mass transport and electric field actions [Schaumburg et al., 2020b,a]. These parameters are the porosity (ϕ), tortuosity (τ), permeability (K), dispersion coefficient (s), and electroosmotic mobility (K_{eo}) [Urteaga et al., 2018, Mirzadeh et al., 2020]. Although a detailed knowledge of the substrates seems to be necessary to develop reliable devices, little effort has been done to characterize the the most common paper types used in e-µPADs. The aforementioned set of parameters can be split into two groups. On one hand ϕ, K, and s are consistently informed with a remarkable reproducibility. On the other hand τ and K_{eo} are scarcely reported and with significant dispersion over their numerical values. Although this work focuses on K_{eo}, it is also of critical importance to develop similar studies on τ.

On a general basis, K_{eo} can be defined as the ratio between the mean electroosmotic velocity

u_{eo} and the electric field E, i.e. [Yao and Santiago, 2003],

$$K_{eo} = \frac{u_{eo}}{E}. \tag{A.1}$$

For non-porous media (tipically capillary tubes or microchannels), when the electric double layer is thin compared to the width of the channel, K_{eo} is given by the Helmholtz-Smoluchowski relation [Probstein, 2003]:

$$K_{eo} = -\frac{\epsilon\zeta}{\mu} \tag{A.2}$$

where ϵ and μ represent the electrical permittivity and viscosity of the solvent, while ζ represents the electrokinetic potential, i.e. the potential difference across the electric double layer, which depends on the material of the wall, polarity of the solvent, and, ionic strength and pH of the electrolyte solution [Berli et al., 2003].

In contrast to equation A.2, extensively validated for capillary and microchip electrophoretic separations [Damián et al., 2019], there are only a few models of K_{eo} for porous media, mainly based on modelling the paper substrate as a bunch of non-interconnected capillary tubes [Schaumburg et al., 2020a, Yao and Santiago, 2003, Rosenfeld and Bercovici, 2019]. In such models, the ζ-potential associated to electroosmotic flow (EOF) in paper substrates (ζ_p) plays the role of an operational parameter, whose value condenses most of the assumptions performed by such models. Recently, Schaumburg et al. presented a comprehensive model for electromigrative phenomena in paper-based substrates [Schaumburg et al., 2020a]. This model considers the e-µPADs material as a set of tortuous capillaries, with a preferential direction for the flow and with an equivalent section along the flow for each capillary. Using this model it is possible to arrive to an expression for K_{eo}; by considering the pressure gradient negligible, as it is the case of pure EOF on a single paper strip (which is also the case of our experimental setup) such expression is:

$$K_{eo} = -\frac{\phi\epsilon\zeta_p}{\tau^2\mu}. \tag{A.3}$$

Thus, K_{eo} can be obtained from ζ_p provided that parameters characteristic of the substrate and the fluid are known. It that regard, Schaumburg et al. validated their model with a ZE experiment from literature, using $\tau = 2.9$ and $\zeta_p = -15$ mV for Whatman # 1 filter paper, although parameters were reported with a level of uncertainty higher than 50 %. Similarly, the scarce ζ_p values reported calculated using other porous media models, also show great scatter. For instance, Rosenfeld and Bercovici [Rosenfeld and Bercovici, 2019] obtained $\zeta_p = -45$ mV starting from an EOF measurement in nitrocellulose at $pH = 8$. Also, Leung [Leung et al., 2010] obtained $\zeta_p = -12.5 \pm 6.5$ mV

when $pH = 3.7$ for Whatman #1 paper using a fiber-pad streaming potential technique. To the best of our knowledge, the rest of the reported numerical values for EOF characterization were obtained using the electric current monitoring method for Whatman #1 or other filter paper with similar pore sizes [Kunkel and Tiselius, 1951, Mettakoonpitak and Henry, 2018, Schaumburg et al., 2019]. Different from capillaries or microchannels, using the electric current method for EOF measurement in paper substrates is challenging and suffers from poor reproducibility. The uncertainty and scatter of informed ζ_p and K_{eo} values show that substrate characterization is still not up to the requirements of rational design of e-µPADs . The aforementioned problem uncovers the need of a unique and accepted model for e-µPADs to enable researchers to associate EOF with an intrinsic ζ-potential at the solid-liquid interface in the microscopic level, and the need of a reliable and robust method for the quantification of EOF in e-µPADs for direct estimation of K_{eo}.

Consequently, in this work we present a reliable and affordable method for K_{eo} measurement. We also present numerical values for K_{eo}, with a conscious quantification of uncertainties, for three different substrates with frequent use in e-µPADs : Whatman #1, S&S, and Muntktell 00A filter paper. Besides the numerical values obtained for uncertainties a discussion is included to identify and quantify possible deviations from the linear model in terms of evaporation and viscosity changes due to the heating by Joule effect of the substrates. We also provide equivalent values for ζ_p, by using the model presented in [Schaumburg et al., 2020a] and finally gather such information with previously reported values in order to provide readers for the first time (to the best of our knowledge) with a reliable compilation of ζ_p values for the most frequently used substrates. The presented EOF measurement method as well as the numerical values obtained will endow developers with reliable data, which will allow rational design of e-µPADs, needed to tackle new applications in sensitive fields like POC or food safety.

A.2. Materials and methods

A.2.1. Buffer solutions

In order to keep pH values constant during measurements Tris acetate (12 mM Tris - 22 mM acetic acid, pH=4.78), Tris phosphate (6.3 mM Tris - 4 mM phosphoric acid, pH=7.02), and Ammonium acetate (7 mM ammonium - 3.5 mM acetic acid, pH=9.29) were used as BGEs. All compounds were purchased from Laboratorios Cicarelli (Reagent SA, San Lorenzo, Argentina). All solutions were prepared with ultra pure water obtained from an inverse osmosis purifier (Osmoion, Apema SRL, Villa Dominico Argentina). The pH and conductivity of solutions were corroborated with ph-Meter (Adwa A12, Szeged, Hungary) and conductivity meter (Adwa AD 203,

Szeged,Hungary).

A.2.2. Experimental setup

The proposed setup is based on the gravimetric measurement of the electroosmotic flow in a paper strip placed over two parallel blades in the arrangement shown in the Fig. A.1. Here, the middle blade is attached to a fixed support and the left blade is placed over a precision scale (Ohaus Pioneer, Parsippany, NJ, USA). The scale records the change of mass distribution produced by the EOF. This scheme amplifies the force over the scale and balances the effects of evaporation, as will be explained in the next section. More graphical details about the setup and connections can be found in the supporting information.

Paper strips were cut from disks (Whatman #1, grade No. 1, 120 mm discs; Munktell, 00A, 125 mm discs; S&S, 0859, 150 mm discs) into $58\,\mathrm{mm}$ long (L_{tot}) and $20\,\mathrm{mm}$ width (w) pieces following the machine direction [Elizalde et al., 2016]. Devices were fabricated by laser-cutting (40W CO_2 laser from Lasers Cuyana, San Rafael, Argentina) and hot lamination (DASA LM330) on both sides of the paper strip. At both ends, symmetric $9\,\mathrm{mm}$ space was intentionally left for the liquid reservoirs by using a shorter lamination pouch on one side. Paper channels were laminated using film pouches of 150 µm thick (Binderplus, China) at 130 °C, at constant speed of 3.5 mm/s. The back of the strip was attached to hydrophobic double-sided adhesive tape (Stiko, Silkstone SA, Buenos Aires, Argentina), and placed over a glass slide settled on the top of the two thin blades, following the scheme in Fig. A.1.

Electric potential on the range of $\pm\ 100 - 500\,\mathrm{V}$ were applied across the reservoirs by using two platinum electrodes keeping minimum contact with the liquid in the reservoirs to minimize interference from buoyancy forces. It was supplied by a computer controlled electric source (Keithley 6487 Picoammetter, Cleveland, OH, USA). This instrument can measure the applied current, which allows estimating the electrical resistance of the circuit as a function of time. The polarity was inverted periodically after $50\,\mathrm{s}$ in order to balance residual evaporation effects (see next section), but also possible redox effects on electrode surface, such as bubble formation or electrolyte exhaustion, among others. Temperature measurements were performed with an infrared thermometer Testo 805i (Neustadt, Germany). Mass measurement experiments were repeated at least three times. Each experiment involved 6 to 10 voltage cycles. The scale digital output was analyzed by using the open source tool GNU Octave [GNU Octave Online, 2022].

A.2.3. Measuring principle

The stability of the glass slide in Fig. A.1 requires a zero net sum of the moments with respect to the fixed support:

$$F_1 L_1 - F_2 L_2 - R_s d_s = 0$$

where F_1 and F_2 are the liquid weight in reservoir 1 and 2 respectively, R_s is the force measured by the scale, and L_1 and L_2 are the lengths measured from the center of mass of each reservoir to the fixed support (See Fig. A.1). In this equilibrium equation, the torque contributions of the paper strip, double-sided adhesive tape and the glass slide are not considered as they do not change their contribution during the measurement process.

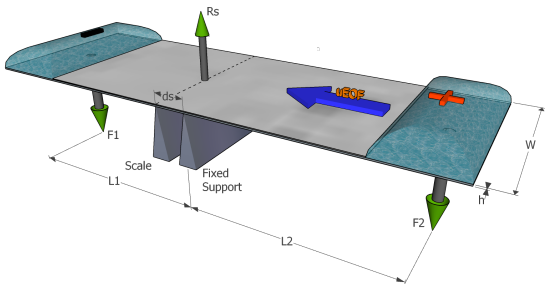

Figure A.1: Experimental setup used to measure EOF on paper substrates. A scale and a fixed support holds the paper strip. Minus (black) and plus (red) signs indicate a possible configuration for applying electric potential at reservoirs R_1 and R_2, respectively, generating EOF in the direction indicated by the blue arrow. This direction is alternated over the experiments as it is described in section A.2.5.

When a positive electric potential difference $\Delta\Phi$ is applied between reservoirs 1 and 2, after a time period Δt, a mass fraction Δm moves from reservoir 2 to reservoir 1. In this condition, a new equilibrium situation is reached, i.e.:

$$(F_1 - g\Delta m)L_1 - (F_2 + g\Delta m)L_2 - R_s^{'} d_s = 0$$

where $R_s^{'}$ is the new force measured in the scale. In this way, the variation in the scale $R_s^{'} - R_s = \Delta R_s$ can be calculated as:

$$\Delta R_s = g\Delta m \frac{L_1 + L_2}{d_s} = g\Delta m \frac{L}{d_s}. \tag{A.4}$$

Since $g\Delta m$ is the force value that the balance would record when measuring a mass Δm, i.e.

the weight of Δm, the ratio L/d_s results in an amplification factor of the measured weight. In our experiments this factor is approximately 25. Simultaneously, this experimental layout allows self-compensation of the mass variations at the reservoirs due to evaporation. Actually, if a mass quantity Δm_e is evaporated *simultaneously* at each reservoir, the scale measurement variation will be:

$$\Delta R_s = g\Delta m_e \frac{L_1 - L_2}{d_s}. \tag{A.5}$$

In this way, by choosing L_1 similar to L_2 by symmetrically placing the reservoirs around the fixed support, the variations due to evaporation can be canceled out. In any case, if any asymmetry still persists, it is expected a constant change of the scale measure. If the direction of the EOF is periodically reversed (changing the polarity of the potential), then it is possible to subtract this effect from the measurements, as it is shown in the next section.

The electroosmotic volume flow rate Q_{EOF} and Δm are related through density ρ, i.e. $\Delta m = \rho Q_{EOF}\Delta t$; where $Q_{EOF} = u_{EOF}wh$ with h being the thickness of the paper strip. Combining these definitions, eq. (A.4), and using $\Delta m = \Delta R_s/g$ one finally obtain,

$$u_{EOF} = \frac{\Delta m d_s}{wh\rho\Delta t L} \tag{A.6}$$

A.2.4. Calibration

The calibration procedure presented in this section is meant to obtain the amplification factor L/d_s shown in eq. (A.4). This coefficient could be calculated by direct measure of the distances involved, however this will introduce a new error, since L_1 and L_2 are measured from the fixed support to the center of mass of the drops on the reservoirs. Here we propose a simple method to overcome this issue. Initially, the glass slide is placed in position (i.e: the center of gravity of the slide between the fixed support and the scale); once equilibrium is achieved, a buffer solution drop of mass m_0 is released on reservoir 1, noticing a change in the scale of mass $\Delta m_1 = m_0 \cdot L_1/d_s$. At this time, the liquid starts to flow in direction to reservoir 2. When the fluid front reaches the end of the laminated paper strip, a second drop of mass m_0 is released on reservoir 2, with a consequent change of magnitude $\Delta m_2 = -m_0 \cdot L_2/d_s$. In this case the force on the scale decreases, given the relative position of the reservoir 2 to the fixed support (See Fig. A.1).

Taking into account the mass change values obtained during the calibration procedure, the

amplification factor can be readily obtained as,

$$L/d_s = \frac{\Delta m_1 - \Delta m_2}{m_0} \tag{A.7}$$

In the experiments, the mass of the drops used at calibration, m_0, was approximately $200\,\mu g$, corresponding to a solution volume of $200\,\mu L$. Distances (L_1 and L_2) from the center of mass of each reservoir to the fixed support were about $25\,mm$. The distance between blades was approximately $2\,mm$, resulting in an amplification factor of approximately 25.

It is important to note that it is assumed that throughout the measurement process, the center of mass of the liquid in the reservoirs does not change its position. This hypothesis is reasonable since the shape of the liquid does not change substantially due to evaporation.

A.2.5. Data processing

Data acquired from mass measurements is processed in order to calculate the mass change ratio $\Delta m/\Delta t$ from eq. (A.6) to finally calculate K_{eo} by means of eq. (A.1). Fig. A.2 A shows the mass evolution obtained for a typical measurement using Whatman #1 paper at $pH = 4.78$, alternating $\Delta\Phi = \pm$ 300 [V] every $\Delta t = 50s$. It is worth to note the positive and negative slopes after a Δt period, which correspond to the polarity inversion of $\Delta\Phi$. Taking relative peak points at regular interval of Δt, Δm can be precisely accounted for.

Data series with positive and negative slopes are averaged separately and later combined to obtain a single value. This procedure corrects the mass drift found in each experiment. A linear trend is used to fit data-points. The initial and final 5 % of the signal is not considered to avoid noisy data obtained around the abrupt voltage changes (inset in Fig. A.2 A). These sharp peaks are produced by small bubbles detached from electrode surface generating a detectable force that is measured by the scale.

In addition to the mass drift, Fig. A.2 shows a similar effect over the electric resistance, which exhibits a decay (Fig. A.2 B).

Electric resistance has a transitory phase due to the reconfiguration of the electrical double layer at electrode surfaces (resistance downward sharp peaks in Fig. A.2 B). It is worth to mention that the described sharp transitory effects are kept out of the measurement results as far as they occur in a region that is not considered for calculation.

The decay effects over mass and resistance measurements will be discussed in section A.3.3. Finally, weighted arithmetic mean is used to estimate the u_{EOF} for each pH value.

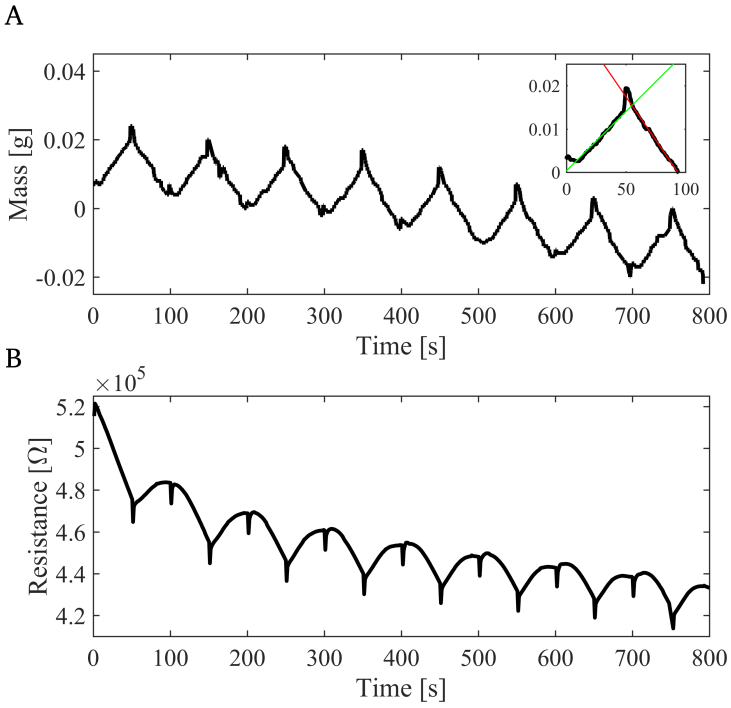

Figure A.2: Scale lecture (A), and electrical resistance (B) as function of time for Tris-Acetic, $pH = 4.78$, $\Delta\Phi = \pm$ 300 [V] and $\Delta t = 50s$, for Whatman #1 . The linear fit for averaged mass signal is shown in the inset.

A.3. Results and discussion

A.3.1. Electroosmotic flow measurements

Fig. A.3 gathers the main results obtained with the presented experimental method, showing the measured electroosmotic velocity and mobility as a function of electric potential for the three different values of pH, in Whatman #1 paper.

A remarkable linearity is shown for low electric potential values, which reinforces the model presented in eq. (A.3). In contrast, linearity decreases with high potential values, and the possible causes for this deviation are discussed in section A.3.3.

A.3.2. K_{eo} and zeta potential calculations

Table C.1 presents the results obtained for K_{eo} and ζ_p by using eqs. (A.1) and (A.3), respectively. Reported values for K_{eo} were corrected from the deviations of the linear model, by considering the temperature increase due to Joule effect, with its consequent influence over the viscosity. Such influence simultaneously affects electrical and rheological parameters of the system. The reported values of K_{eo} obtained at room temperature (K_{eo0}) are obtained from fitting the experimental data with a model of heating by Joule effect. This model is discussed in section A.3.3.2.

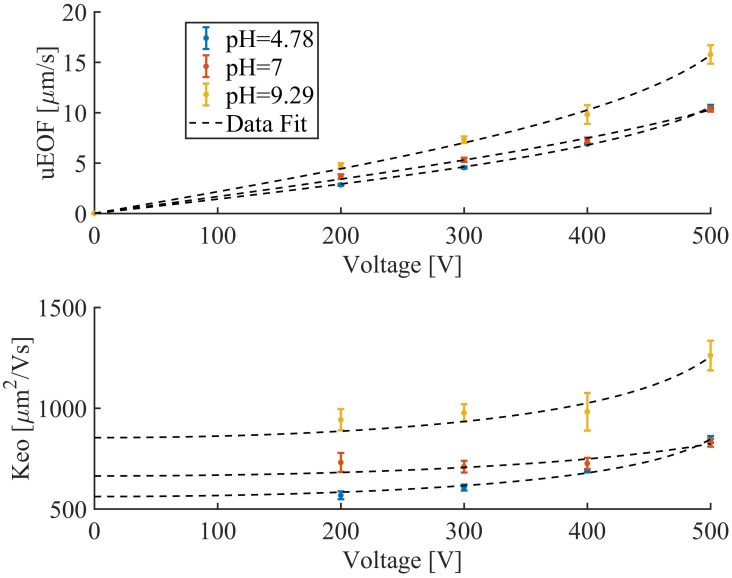

Figure A.3: Measured electroosmotic velocity (A) and electroosmotic mobility (B) for different electric potentials using buffer solutions with variable pH in Whatman #1. Data fit corresponds to eq (A.11), where K_{eo} is modeled using the non-linear model described in section A.3.3.2.Uncertainty values represent the 95 % confidence intervals on the mean using a Student-t distribution.

For the calculation of ζ_p by applying eq. (A.3), $\tau = 2.9$ was considered [Schaumburg et al., 2020a] for all substrates due to the high uncertainty in literature about this parameter. Reliable and robust measurements of τ will be part of a future work. Substrate porosity was found by weighting dry and wet substrates with known geometries.

As far as aqueous diluted solutions were used, we considered $\mu = 1.0\,\mathrm{mPa\,s}$ at initial $23\,^{\circ}\mathrm{C}$ and a relative permittivity $\epsilon = 7.08 \times 10^{-10}\,\mathrm{C^2/Nm^2}$.

	ϕ	pH	K_{eo0} $[\frac{\mu m^2}{Vs}]$	ζ_p [mV]
Whatman #1	0.69	4.78	561 ± 22	−11.8 ± 0.5
		7	664 ± 65	−13.9 ± 1.4
		9.29	854 ± 92	−17.9± 1.9
Munktell 00A	0.47	4.78	537 ± 95	−16.6 ± 2.9
		7	549 ± 40	−16.9 ± 1.2
		9.29	512 ± 68	−15.8 ± 2.1
S&S	0.42	4.78	81 ± 35	−2.7 ± 1.2
		7	214 ± 52	−7.3 ± 1.8
		9.29	258 ± 56	−8.8 ± 1.9

Table A.1: ζ_p potentials and K_{eo0} obtained for different buffer solutions and types of substrates used. Uncertainty values were calculated by using 95 % confidence bounds in fit process by using eq. A.11

.

Finally, the obtained values for ζ_p were gathered with other values obtained from literature in Fig. A.4. This figure reflects the reliability and robustness of the proposed method by considering the magnitude of the error bars, but also the monotonicity of the measured values with pH. The behaviour of the other measured substrates is similar, i.e. K_{eo} and ζ_p increase with pH, with higher influence of pH for S&S, moderate for Whatman #1, and very stable conditions for Muntktell 00A. In terms of magnitude of the flow S&S paper exhibits a very low K_{eo} which makes it suitable for applications that require EOF cancellation or minimization. In the case of Muntktell 00A, its stability over pH offers good oportunities to implement techniques with broad pH range operations such as IEF. Finally, Whatman # 1 paper offers a similar behaviour to closed channel materials such as glass or hydrophylic PDMS, working as a good starting point for adapting traditional electrophoretic separations to paper-based substrates.

It is worth to mention here that the reported values for K_{eo0} and ζ_p correspond to those measured with pouch laminated paper substrates to minimize evaporation effects as far it is recommendable for improving reproducibility. These reported values can be slightly modified when working with bare substrates (without lamination) or different lamination materials, due to the fact that lamination has a limited influence over the total fiber free surface that allocates electrical double layer producing EOF.

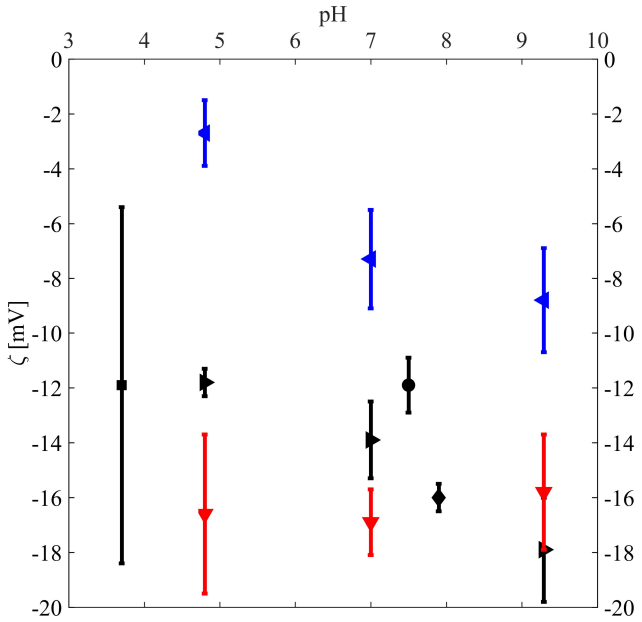

Figure A.4: $\zeta_p(pH)$ values for different substrates. Square (■ [Leung et al., 2010]), circular (● [Mettakoonpitak and Henry, 2018]) and rhomboidal (♦ [Schaumburg et al., 2019]) markers correspond to results obtained for Whatman#1 starting from bibliography data. Triangular markers correspond to estimations performed with experimental data obtained in this work for different paper types: Whatman #1 (►), Munktell 00A (▼) and S&S (◄).

A.3.3. Deviations from linear model

In order to account for possible error sources which deviate the obtained experimental values from the linear model, in the following we describe different effects that are present in the setup affecting the measurement process. We discuss also how to tackle or quantify such effects for improving future setups.

A.3.3.1. Evaporation

Evaporation is an important effect to consider in measurements. It reduces reservoir volume with time and affects measurements. However, the presented setup self-compensates the evaporation effect as it was already discussed in section A.2.3. However, such effect can be quantified in a calibration procedure by measuring the slope after the wetting front reaches the end of the paper strip and waiting for the pores of the paper strip to be fully saturated as was described in section A.2.4. Evaporation symmetrically affects both reservoirs, consequently, the scale will not register any changes in this configuration. Nevertheless, a small effect is still present due to a possible asymmetry of the relative reservoir positions relative to the fixed support. This residual asymmetry is corrected by averaging positive and negative slopes as it is shown in Fig. A.2 A and its inset.

A.3.3.2. Conductivity drift and Joule effect

In Fig. A.2B the electric resistance over time is shown for $\Delta\Phi = 300\,\mathrm{V}$ inverted periodically every $50\,\mathrm{s}$. It can be seen there that the average value is decreasing over time. On a general basis, such resistance is given by:

$$R_p = \frac{1}{\sigma_p}\frac{L}{A_p} \tag{A.8}$$

where subscript p refers to paper, A_p is the cross-sectional area and σ_p the electric conductivity. Therefore, the time-dependent variations observed in Fig. A.2 B can be explained only through changes in L, A_p or σ_p. Assuming that L and A_p are constant parameters over long time periods, focus must be put on σ_p changes. For a paper substrate, completely wet with an electrolyte solution, σ_p can be calculated as [Schaumburg et al., 2020a]:

$$\sigma_p = F\sum_{j=1}^{N} z_j^2 \frac{\Omega^j}{\tau^2} C^j \phi \tag{A.9}$$

where F is the Faraday constant, Ω^j the electrophoretic mobility, z^j the charge number and C^j concentration of the $j-$th species, respectively. By assuming a buffered system, C^j is constant and

the only variable parameter in eq. (A.9) is Ω^j. If j is a small ion, a possible model for Ω^j [Probstein, 2003] is:

$$\Omega^j = \frac{q^j}{6\pi\mu r_s^j} \tag{A.10}$$

where q^j is the charge, r_s^j is the hydrodynamic radius related to the size of the j-hydrated molecule. Again, from this expression, the only parameter than can change its value over time is μ. The decay observed in the electric resistance as it is shown in Fig. A.2B must be due to the decrease of the viscosity of the solution, due to thermal heating produced by Joule effect. Considering the electric current and potential measured during the experiments, this effect is not negligible.

The power of heating is $P = \frac{V^2}{R_p}$ and it depends on σ_p for each buffer solution. The maximum value for P can reach up to $1\,\mathrm{W}$ at $\Delta\Phi = 500V$. Such heating produces changes in bulk fluid viscosity that are consistent with changes in electric conductivity. For example, surface temperature measurements made in Munktell filter paper using an infrared thermometer, shows that for $\Delta\Phi = 400V$, the temperature change is $\Delta T \approx 22\,^{\circ}\mathrm{C}$. In this process, the electric resistance varies from $2.84 \times 10^5\,\Omega$ to $1.88 \times 10^5\,\Omega$ respectively, obtaining a variation ratio of 0.66. Such ratio is consistent with the expected decrease of the viscosity for the measured temperature range [Huber et al., 2009].

As far as the temperature increase reduces the buffer solution viscosity and this in turn produces the non-linear behavior of u_{EOF} showed in Fig. A.3 at high voltage values. In order to quantify this effect, a physical model that accounts for variations in rheological and electrical properties of the electrolyte was developed. In the following, the main results for such model are provided. Full hypotheses discussion and mathematical details can be found in the supporting information.

Based on such model, the final expression for K_{eo}, related to the electric potential is:

$$K_{eo} = \frac{2K_{eo_0}}{1 + \sqrt{1 - \alpha\Delta\Phi^2}} \tag{A.11}$$

The values reported in Table C.1 were obtained by using this model to fit data shown in Figure A.3. Here, the parameter α gathers the thermal characteristics of the strip and electrical properties of the buffer solution that determine the thermal behavior of the system, it can be calculated as:

$$\alpha = \frac{4A}{Lwh'R_0} \tag{A.12}$$

where A measures the relative viscosity variation dependence with the solution temperature (about

$0.024\,\mathrm{K}^{-1}$ [Huber et al., 2009] at ambient temperature), L and w are geometrical dimensions of the paper strip (see Fig.A.1), R_0 is the electrical resistance at room temperature and h' is the convective heat transfer coefficient. As it was mentioned, the parameter α characterize, the system both in terms of heat generation (due to Joule effect, through R_0), but also in terms of heat dissipation capacity of the strip (through h' and the rest of the parameters).

The values of α obtained from fitting the experimental data are in the range of 2.5×10^{-6}-$3.5 \times 10^{-6}\,\mathrm{V}^{-2}$. This values are consistent with the experimental value found for h' of about $68 \pm 15\,\mathrm{W/m^2K}$ and measured values of R_0 around $0.5\,\mathrm{M\Omega}$. More details about this calculations can be found in the supporting information.

A.4. Concluding remarks

In this work, a novel measurement method for K_{eo} has been developed in order to tackle the lack of information for developing robust and rational e-µPADs design. It has been demonstrated along the paper that such method is robust, reliable, and affordable. Such robustness is partially based on the fact that the setup auto-calibrates and self-compensates evaporation effects. All experiments demonstrate to be reproducible with remarkable low scatter when compared to previous works on e-µPADs. The experimental results obtained for K_{eo} are independent of the applied voltage for moderate field values. For high field values, Joule heating must be taken into account, and it was found that the variation in the value of measured K_{eo} can be explained in a consistent way with the decrease in the viscosity of the solution due to temperature increase. A model has been proposed to describe the dependence K_{eo} with the applied voltage, finding a proper correlation with the experimental data. From the obtained K_{eo} we derived $\zeta_p(pH)$ values that are consistent with those previously reported in the bibliography. Moreover, these K_{eo} and ζ_p values allow data driven decision making. For example, a e-µPAD designer might choose Munktell 00A paper, with an almost constant $K_{eo}(pH)$, if the pH of the solution is unknown or it is expected to change, but still wants to keep EOF constant. Alternatively, Whatman #1 might be preferred over S&S paper if higher EOF is required. Finally, we consider that this method is straightforward to be reproduced for other groups devoted to e-µPADs development for the different paper or paper like substrates used in the wide application field of such devices.

Acknowledgments

We thank Dr. Luciana Vera Candioti for her advice about BGEs. This research was supported by ANPCyT (GrantPICT-2018-02920), UTN (Grant PID ASUTIFE0005525TC) and CONICET,

Argentina.

Conflict of interest statement

All authors declare complete absence of financial/commercial conflicts of interest.

References

C. L. A. Berli, M. Piaggio, and J. Deiber. Modeling the zeta potential of silica capillaries in relation to the background electrolyte composition. *Electrophoresis*, 24:1587–1595, 2003.

C. L. Chagas, F. R. de Souza, T. M. Cardoso, R. C. Moreira, J. A. da Silva, D. P. de Jesus, and W. K. Coltro. A fully disposable paper-based electrophoresis microchip with integrated pencil-drawn electrodes for contactless conductivity detection. *Anal Methods-UK*, 8(37):6682–6686, 2016.

H. Cremer, A. Tiselius, et al. Electrophoresis of protein on filter paper. *Biochem. Ztschr.*, 320: 273–283, 1950.

S. M. Damián, F. Schaumburg, and P. A. Kler. Open-source toolbox for electromigrative separations. *Comput Phys Commun*, 237:244–252, 2019.

E. L. Durrum. Continuous electrophoresis and ionophoresis on filter paper1. *J Am Chem Soc*, 73 (10):4875–4880, 1951.

E. Elizalde, R. Urteaga, and C. L. A. Berli. Precise capillary flow for paper-based viscometry. *Microfluid Nanofluid*, 20(10), 2016.

L. Ge, S. Wang, S. Ge, J. Yu, M. Yan, N. Li, and J. Huang. Electrophoretic separation in a microfluidic paper-based analytical device with an on-column wireless electrogenerated chemiluminescence detector. *Chem Commun*, 50(43):5699–5702, 2014.

GNU Octave Online. 2020. Accessed: 2019-07-10.

W. Grassmann and K. Hannig. Ein einfaches verfahren zur kontinuierlichen trennung von stoffgemischen auf filterpapier durch elektrophorese. *Naturwissenschaften*, 37(17):397–397, 1950.

M. Huber, R. Perkins, A. Laesecke, D. Friend, J. Sengers, M. Assael, I. Metaxa, E. Vogel, R. Mareš, and K. Miyagawa. New international formulation for the viscosity of h2o. *J Phys Chem Ref Data*, 38:101–125, 06 2009. doi: 10.1063/1.3088050.

H. G. Kunkel and A. Tiselius. Electrophoresis of proteins on filter paper. *J Gen Physiol*, 35(1): 89–118, 1951.

V. Leung, A.-A. M. Shehata, C. D. Filipe, and R. Pelton. Streaming potential sensing in paper-based microfluidic channels. *Colloid Surf A*, 364(1-3):16–18, 2010.

J. Mettakoonpitak and C. S. Henry. Electrophoretic separations on parafilm-paper-based analytical devices. *Sensor Actuat B-Chem*, 273:1022–1028, 2018.

M. Mirzadeh, T. Zhou, M. A. Amooie, D. Fraggedakis, T. R. Ferguson, and M. Z. Bazant. Vortices of electro-osmotic flow in heterogeneous porous media. *arXiv preprint arXiv:2003.05974*, 2020.

B. Y. Moghadam, K. T. Connelly, and J. D. Posner. Isotachophoretic preconcenetration on paper-based microfluidic devices. *Anal. Chem.*, 86(12):5829–5837, 2014.

R. Probstein. *Physicochemical Hydrodynamics. An Introduction*. Wiley-Interscience, 2nd edition, 2003.

T. Rosenfeld and M. Bercovici. 1000-fold sample focusing on paper-based microfluidic devices. *Lab Chip*, 14(23):4465–4474, 2014.

T. Rosenfeld and M. Bercovici. Dynamic control of capillary flow in porous media by electroosmotic pumping. *Lab Chip*, 19(2):328–334, 2019.

G. I. Salentijn, M. Grajewski, and E. Verpoorte. Reinventing (bio) chemical analysis with paper. *Anal Chem*, 90(23):13815–13825, 2018.

F. Schaumburg, C. Carrell, and C. S. Henry. Rapid bacteria detection at low concentrations using sequential immunomagnetic separation and paper-based isotachophoresis. *Anal Chem*, 2019.

F. Schaumburg, P. A. Kler, and C. L. Berli. Comprehensive model of electromigrative transport in microfluidic paper based analytical devices. *Electrophoresis*, 41(7-8):598–606, 2020a.

F. Schaumburg, P. A. Kler, C. S. Carrell, C. L. Berli, and C. S. Henry. USB powered microfluidic paper-based analytical devices. *Electrophoresis*, 41(7-8):562–569, 2020b. doi: 10.1002/elps.201900273.

R. Urteaga, E. Elizalde, and C. L. A. Berli. Transverse solute dispersion in microfluidic paper-based analytical devices (μPADs). *Analyst*, 143:2259–2266, 2018. doi: 10.1039/c8an00149a.

C. Xu, W. Lin, and L. Cai. Demonstrating electrophoretic separation in a straight paper channel delimited by a hydrophobic wax barrier. *J Chem Educ*, 93(5):903–905, 2016.

S. Yao and J. G. Santiago. Porous glass electroosmotic pumps: theory. *J Colloid Interf Sci*, 268 (1):133–142, 2003.

Anexo B

Multiphysics approach for fluid and charge transport in paper-based microfluidics

El artículo presentado a continuación ha sido publicado en la revista **Microfluidics and Nanofluidics**.

N. Franck, C. L. A. Berli, P. A. Kler, R. Urteaga. Multiphysics approach for fluid and charge transport in paper-based microfluidics. *Microfluidics and Nanofluidics*, 26(11), 2022. `https://doi.org/10.1007/s10404-022-02590-8`.

Multiphysics approach for fluid and charge transport in paper-based microfluidics

Nicolás Franck[1], Claudio L. A. Berli[2], Pablo A. Kler[1,3], Raul Urteaga[4]

[1] Centro de Investigación en Métodos Computacionales (CIMEC, UNL–CONICET), Predio CCT CONICET Santa Fe. RN 168, Santa Fe 3000, Argentina

[2] Instituto de Desarrollo Tecnológico para la Industria Química (INTEC, UNL – CONICET), Predio CCT CONICET Santa Fe. RN 168, Santa Fe 3000, Argentina

[3] Departamento de Ingeniería en Sistemas de Información, Facultad Regional Santa Fe, Universidad Tecnológica Nacional, Lavaisse 610, Santa Fe, Argentina

[4] Instituto de Física del Litoral (IFIS Litoral, UNL–CONICET), Güemes 3450, S3000GLN Santa Fe, Argentina

Abstract

A multiphysic model that simultaneously describe different transport phenomena in porous media is presented. The porous matrix is regarded as a bundle of periodically constricted tubes, whose pore radius distribution is described by a probability density function (PDF). The mathematical basis and the experimental validation of the model are reported. Two different materials frequently used in paper-based microfluidics were used: Whatman #1 and Muntktell 00A filter papers. These substrates were studied by capillary imbibition, hydrostatic pressure-driven flow, and electrical resistance measurements. Different PDFs were evaluated to represent the output of these experiments, and their predictions were quantified by using a Chi-Square test. The model was able to simultaneously describe the three transport phenomena by using the log-normal PDF with two statistical parameters: mean and variance. The formulation avoids including the tortuosity of

the flow path, which is commonly employed as an adjusting parameter. The multiphysics model was also successfully used to calculate the parameters of single-physics models, such as Darcy's permeability and Lucas-Washburn diffusion coefficient. Furthermore, after obtaining a suitable PDF, the proposed model can be applied to different porous materials, as well as to the design of complex paper-based microfluidic devices that combine several types of papers.

Keywords: Paper-based microfluidics, Capillary flow, Fluid transport model, Pore radius distribution.

B.1. Introduction

Understanding the microstructure and physicochemical properties of porous media is of great importance for several fields in order to carry out rational design and optimization processes [Schaumburg et al., 2018a, Masoodi and Pillai, 2010, Gerlero et al., 2022]. Particularly, microfluidic paper-based analytical devices (μPADs) have gained remarkable popularity with their applications in chemistry, medicine, genetics, and cell biology, among others [Modha et al., 2021, Tesfaye and Hussen, 2022]. However, currently there exists the need to accelerate the introduction of μPADs into the market and public health systems. Reliable and useful mathematical models are required to predict the behavior of μPAD under different operative situations, which involve phenomena such as capillary imbibition, pressure-driven flow [Shen et al., 2021], electroosmotic flow, and electric current [Mai et al., 2019, Franck et al., 2021], plus those related to the transport and reaction of different chemical species. Porous media in general, and particularly paper substrates, have being systematically studied for fluid transport and, over the last century, several mathematical models have been proposed together with attempts for experimental validation. The aim was to define and characterize parameters that can act as intrinsic descriptors of pore structure and their influence on the macroscopic behavior of porous media for fluidic and electric phenomena [MacDonald, 2018]. In the pioneer works of [Lucas, 1918] and [Washburn, 1921], paper was modelled as a single circular and uniform cross section capillary tube. Later on, [Kozeny, 1927] modelled the porous medium as a bundle of capillary tubes of equal length, with not necessarily circular cross-section, neglecting the fluid velocity normal to the tube's axis. More recently, [Bear, 1972] represented the flow through a parallelepiped body of porous medium in a laminar flow regime, with circular capillary tubes of fixed diameter, by using the Hagen-Poiseuille law, and [Scheidegger, 1974] related the distribution of diameters of the capillary tubes to the pore size distribution. During the last years, models composed of a network of interconnected capillary channels were proposed [Gruener et al., 2012, Cummins et al., 2017].

Regarding capillary-driven flow, numerous experimental works have been documented as input for more complex interpretations of Lucas-Washburn dynamics. For example, [Böhm et al., 2014] studied the influence of the fiber material and porosity on the efficiency of capillary-driven flow of aqueous solutions. [Elizalde et al., 2016] made systematic wetting cycles and observed the trends in the imbibition dynamics due to changes in the inner structure of Whatman # 1 paper. More recently, [Lei et al., 2021] presented a model for the dynamics of capillary flow in periodically (sinusoidal) undulated channels, predicting the capillary rising dynamics. Additionally, the speed of meniscus advance as a function of capillary radius (variable) was described by [Gorce et al., 2016]. A similar process was documented for electrical properties, as it is described in the first works of [Archie, 1942], where the author proposed an empirical relationship that links the experimentally measured factors to the electrical conductivity of both the saturated rocks and the solution inside the void space. There were also different proposed relationships between the electrical conductivity of saturated porous media and pore fluid conductivity, like those based on effective medium [Bussian, 1983], percolation [Ghanbarian et al., 2014] and cylindrical tubes [Herrick and Kennedy, 1994].

As it was mentioned above, an important number of mathematical models and the associated experiments have been presented in the literature, aiming to reproduce only a particular phenomenon, such as Darcy flow [Mora et al., 2019], capillary imbibition [Piovesan et al., 2022, Elizalde et al., 2016, Salama et al., 2021], electrical resistance [Mai et al., 2019], electroomotic flow and electrophoretic migration [Schaumburg et al., 2020a], or advective non-reactive transport [Schaumburg et al., 2018b, Urteaga et al., 2018]. With the aforementioned exceptions, most of these models consider the paper porous structure as a bundle of non-interconnected capillary tubes and, on a general basis, the idea requires three different parameters: (i) porosity (ϕ), which is a direct physical parameter representing the fractions of void volume over the total volume of the substrate; (ii) Darcy permeability (K), which represents the constant of proportionality between the pressure gradient and the fluid flow under Darcy flow conditions; and (iii) tortuosity (τ), which is defined as the ratio of the hypothetical average length of the capillary tubes to the length of the substrate in the flow direction [Duda et al., 2011]. These three parameters clearly differ on their nature and accessibility. While ϕ and K can be measured via several techniques [Berg, 2014, Bear and Cheng, 2010], τ is a mathematical abstraction attached to the hypotheses of the model of non-interconnected capillary tubes [Liu et al., 2018, Cai et al., 2014, Duda et al., 2011].

It has been shown experimentally that capillary-driven infiltration in paper strips follows the simple Lucas-Washburn dynamics, $L^2 = Dt$, where L is the position of the imbibition front at time t and is D a dynamic coefficient that depends on the characteristics of both the fluid and

porous matrix. Actually, D is related to the Darcy permeability by $D = K\Delta P/\mu$, where ΔP is the driving pressure difference, and μ is the fluid viscosity. Further descriptions of D in terms of the paper microstructure require models for both K and ΔP.

The simplest physical representation of the porous space is the capillary bundle model: straight, parallel, and not interconnected pores of hydrodynamic radius r_h, for which the permeability is $K = r_h^2/8$. Concerning the pressure, the Laplace equation is adopted, $\Delta P = 2\gamma cos\theta/r_c$, where γ is the surface tension, and θ is the meniscus contact angle, and r_c is the capillary radius. Besides, it is customarily assumed that $r_h = r_c = r_{pore}$, where r_{pore} is expected to be the actual pore radius of the porous matrix. Then, the dynamic coefficient results $D = r_{pore}\gamma cos\theta/(4\mu)$. The practical problem that emerges is that water infiltration in paper (namely Whatman #1, nominal pore radius about $11\mu m$) is much slower than the value predicted by the above expression. Conversely, the effective pore radius (r_{eff}) that satisfies the experimental value of D is abnormally small (about $100nm$).

A straightforward correction is the incorporation of the tortuosity τ, aimed to account for the non-linear fluid paths of the cellulose matrix. Thus, considering $r_{eff} = r_{pore}/\tau^2$, the tortuosity of Whatman #1 ($r_{pore} \sim 11\mu m$) results $\tau \sim 10$, which is much larger than the expected for the configuration of cellulose fibers in paper. A second drawback of this approach is that the tortuosity values required to fit experimental data, strongly depends on the type of experiments (capillary filling, pressure driven-flow or electrically-driven transport) [Ezzatabadipour and Zahedi, 2021, Gerlero et al., 2021b]. It is therefore necessary to extend the existing models to a more general multiphysic approach that represents several transport phenomena at the same time, while avoiding the uncertain parameter τ in calculations.

Alternatively, one may introduce the well-known concept of periodically constricted tubes: a capillary bundle of parallel tubes, but now the pore radius is allowed to vary along the axial direction. Considering capillary tubes with periodic step changes of radius, from r_{max} to r_{min} and vice versa, yields $r_{eff} \sim (r_{min}^4)/(r_{max}^3)$ [Berli et al., 2017]. For Whatman #1, assuming $r_{max} \sim 11\mu m$, one obtains $r_{min} \sim 3.1\mu m$. Although these values are physically sound, one is still dealing with a pair of unknown parameters (analogously to $r_{eff} = r_{pore}/\tau^2$), where at least one of them cannot be measured. The problem is inherited from the ambiguous inclusion of the hydrodynamic and meniscus radius in the model, as mentioned above. In fact, the fluid dynamic problem itself suggests that there must be two relevant lengths characterizing the pore-scale geometry. In our present proposal, we stay in the scenario of the bundle of capillaries with periodically varying radii and include an innovative approach: the use of a probability density function to describe the pore radius distribution. Mathematically speaking, we are still dealing with the determination of

two parameters (the mean and variance of the distribution), but these characteristic parameters are able to simultaneously represents four different transport phenomena (capillary filling, pressure-driven flow, electric transport, and electroosmotic flow), which constitutes a substantial gain in the route toward a generalized model of paper substrates.

The experimental validation was performed over two substrates frequently used in μPADs: Whatman #1 and Muntktell 00A filter papers. We report measurements of capillary imbibition, hydrostatic pressure-driven flow, and electrical resistance measurements. The proposed PDFs were evaluated by quantifying their predictions for the three experiments using a χ^2 test. The alternative modelling here presented enables a more general approach for describing the paper micro-structure with an arbitrary number of parameters. The model overcomes the previously reported single-physics approaches and can be also used as a valid strategy for the simultaneous estimation of several parameters that characterize the transport properties of paper, such as Darcy permeability, Washburn constant, or zeta potential, from simple and reproducible experimental results. Moreover, after defining a suitable PDF for each paper, the behavior of μPADs that combine different porous materials can be objectively evaluated.

B.2. Model formulation

Fig. B.1 presents a simplified scheme of the proposed configuration for porous substrates as an arrangement of N_p parallel constricted tubes.

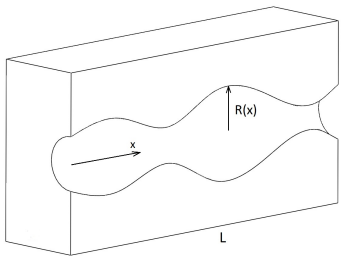

Figure B.1: Simplified scheme of the proposed configuration for a single constricted tube. The structure randomly repeats N_p times, without interconnections between neighbor tubes.

In this case, the function $R(x)$ represents the constriction function, i.e. the tube radius as a function of distance x (the main direction for the fluid flow and electric field). Following this modelling strategy, the porosity can be calculated as:

$$\phi = \frac{N_p \int_0^L \pi R(x)^2 dx}{AL} \tag{B.1}$$

where A is the cross sectional area (commonly rectangular) and L is the length of the material considered.

B.2.1. Hydrodynamic model

Considering that $R(x)$ is smooth along the $x-$axis and neglecting inertial effects (intra porous flow involves very low Reynolds numbers), one may use the Hagen-Poiseuille relation to calculate the flow rate through a single pore Q_h as follows [Reyssat et al., 2008]:

$$Q_h = \frac{\Delta P \pi}{8\mu_\ell \int_0^L R(x)^{-4} dx} \tag{B.2}$$

where ΔP is the applied pressure difference and μ_ℓ is the liquid viscosity. Accounting for the N_p pores present in the substrate, the total flow rate is $Q_H = N_p Q_h$. Further, introducing Eq. B.1 yields,

$$Q_H = \frac{\Delta P \phi A}{8\mu_\ell L} \frac{1}{\int_0^L R(x)^2 dx \int_0^L R(x)^{-4} dx}. \tag{B.3}$$

The $n-$th probability moment for the radius distribution is written as,

$$< R^n > \equiv \frac{\int_0^L R(x)^n dx}{L}. \tag{B.4}$$

Then, it is possible to define an equivalent hydraulic radius R_H as follows,

$$R_H \equiv \sqrt{\frac{Q_H 8\mu_\ell L}{\Delta P \phi A}} = \sqrt{\frac{1}{< R^{-4} >< R^2 >}} \tag{B.5}$$

which represents the capillary radius of a bundle of uniform tubes exhibiting the overall flow rate Q_H. Equation B.5 relates quantities that can be experimentally measured (first equality) to a certain combination of the probability moments of the radii distribution in the constricted tube model (second equality).

B.2.2. Capillary imbibition model

Capillary imbibition in porous materials has been extensively studied for more than 100 years and is currently an active topic of research [Cai et al., 2022, Piovesan et al., 2022]. Capillary imbibition dynamics on a constricted tube (Fig B.1) has been analyzed by different authors and

can be modelled as [Young, 2004, Gorce et al., 2016, Reyssat et al., 2008]:

$$\int_0^L R(l)^3 \left[\int_0^l \frac{dx}{R(x)^4}\right] dl = \frac{\gamma \cos\theta t_{fill}}{4\mu_\ell} \tag{B.6}$$

where γ is the surface tension of liquid, θ is the contact angle of the advancing meniscus in the pores, and t_{fill} is the filling time. Given that porous morphology is uniform along the imbibition direction, i.e. the PDF is the same in all macroscopic regions, the definition of probability moment (Eq.B.4) can be also used in an intermediate length scale l (instead of L) to obtain:

$$\int_0^L R(l)^3 \left[\int_0^l \frac{dx}{R(x)^4}\right] dl = < R^{-4} > \int_0^L R(l)^3 l dl.$$

Moreover, a periodic radius profile can be used to estimate the last integral, taking $R(x) = R(x + nl_p)$, being n a natural number. If $L \gg l_p$ and $nl_p \approx L$,

$$\int_0^L R(l)^3 l dl \approx \int_0^{nl_p} R(l)^3 l dl = \sum_{i=1}^{n} \int_{(i-1)l_p}^{il_p} R(l)^3 l dl$$

Considering that n is large, and the last integral is over one period, each term in the sum can be approximated by $< R^3 > il_p^2$ and:

$$\int_0^L R(l)^3 l dl \approx < R^3 > l_p^2 \sum_{i=1}^{n} i \approx < R^3 > \frac{L^2}{2}$$

Using this approximation, Eq. B.6 results:

$$< R^{-4} >< R^3 > \frac{L^2}{2} \approx \frac{\gamma \cos\theta t}{4\mu_\ell}. \tag{B.7}$$

Finally, it is possible to define an equivalent capillary radius R_C of uniform tubes that produces the same infiltration rate:

$$R_C \equiv \frac{2L^2\mu_\ell}{\gamma \cos\theta t_{fill}} = \frac{1}{< R^{-4} >< R^3 >}. \tag{B.8}$$

This result is in accordance with previously reported calculations for sinusoidal constricted tubes and infiltration of mesoporous films [Sharma and Ross, 1991, Berli et al., 2017]. In analogy to Eq. B.5, Eq. B.8 relates measurable quantities to a particular combination of the probability moments of the radii distribution in the constricted tube model. Moreover, after estimating R_C the

Washburn coefficient D can be calculated as [Washburn, 1921]:

$$D = \frac{\gamma \cos\theta R_C}{2\mu_\ell}. \tag{B.9}$$

B.2.3. Electric Model

Keeping the hypothesis that $R(x)$ is smooth, the electric potential will be only function of x inside the tube. Also, if the electrical conductivity of fibers is negligible, the electrical resistance of a bundle of N_p parallel tubes can be calculated as:

$$R_p = \frac{\rho}{N_p} \int_0^L \frac{dx}{\pi R(x)^2}$$

where ρ represents the electrical resistivity.

Introducing Eq. B.1, the electrical resistance results:

$$R_p = \frac{\rho \int_0^L \pi R(x)^2 dx \int_0^L \frac{dx}{\pi R(x)^2}}{\phi A L}.$$

Using Eq. 4 leads to the following relationship between the paper electric resistance and the probability moments:

$$R_p \left(\frac{\phi A}{\rho L} \right) =< R^2 >< R^{-2} > . \tag{B.10}$$

The right hand side of Eq. (B.10) can be interpreted as a constriction factor (C) that always satisfies $C \geq 1$, being $C = 1$ in the case of uniform tubes. Then, the electrical resistance of saturated material is $\frac{\rho L}{\phi A}$, which represents an equivalent prism of resistivity ρ, section ϕA, and length L.

B.2.4. Electroosmotic flow model

Electroosmotic (EO) flow is generated when a potential difference $\Delta\Phi$ is applied to a saturated porous material that is electrically charged at the solid-liquid interface. The EO velocity can be calculated by the product of the EO permeability ($K_{eo} = \frac{\epsilon\zeta}{\mu_\ell}$)[1] and the electric field ($E = \Delta\Phi/L$). Then, the EO flow rate for a single tube is [Probstein, 2005]:

$$Q_{eo} = \bar{u}_{eo}\pi R^2 = \pi R^2 \frac{\epsilon\zeta}{\mu_\ell} E$$

[1] where ϵ is the electrical permittivity of the solvent and ζ the electrokinetic potential.

which can be rewritten as follows, after using Eq. 4,

$$Q_{eo} = \frac{\epsilon\zeta}{\mu_\ell} \frac{\Delta\Phi}{\int_0^L \frac{dx}{\pi R(x)^2}}$$

Finally, considering N_p pores, the EO flow measured in the porous substrate is [Franck et al., 2021]:

$$\begin{aligned} Q_{EO} = Q_{eo} N_p &= \frac{\epsilon\zeta}{\mu_\ell L} \frac{\Delta\Phi}{< R^{-2} >} \frac{\phi A L}{< R^2 >} \\ &= \frac{\epsilon\zeta\phi A}{\mu_\ell} \Delta\Phi \frac{1}{< R^{-2} >< R^2 >} \end{aligned}$$

It is worth to mention here that one cannot determine the probability moments by a direct measurement of Q_{EO}, unless the ζ potential is known beforehand. However, since the expression for the probability moments agrees with the proposed for the electrical model, the term $\frac{1}{<R^{-2}><R^2>}$ can be obtained from electrical measurements and, consequently, the ζ potential could be determined from EO flow experiments (see section B.4.3).

B.3. Experimental

B.3.1. Materials

Three types of experiments were conducted, wich are outlined in Fig. B.2 and described in the following sections. Paper strips were cut from disks (Whatman #1, grade No. 1, 120 mm disc, Cityva, Marlborough, USA; Munktell, 00A, 125 mm disc, Munktell Filter AB, Falun, Sweden) following the machine direction [Elizalde et al., 2016]. A solution of Tris-Acetate (12 mM Tris - 22 mM acetic acid, pH=4.78) was employed for electric experiments. Solution was characterized with a conductivity meter (Adwa AD 203, Szeged, Hungary) and electrical resistance was measured with a Picoammeter/Voltage Source (Keithley 6487, Cleveland, OH, USA). Devices were fabricated by laser-cutting (40 W CO_2 laser, Lasers Cuyana, San Rafael, Argentina) and hot lamination (DASA LM330) on both sides of the paper strips using 150 µm thick pouches (Binderplus, China) at 135 °C, at a constant speed of 3.5 mm/s. This setup minimizes the effects of evaporation on measurements. At both ends, symmetric 9 mm spaces were left for liquid reservoirs, by using a shorter lamination pouch on one side. A precision scale (Ohaus Pioneer, Parsippany, NJ, USA) was used for fluid dynamic and surface tension experiments. Acetic acid and tris were purchased from Laboratorios Cicarelli (Reagent SA, San Lorenzo, Argentina). All solutions were prepared with ultra pure water obtained from an inverse osmosis purifier (Osmoion, Apema SRL, Villa Do-

minico Argentina). The same water was used for hydrostatic pressure-driven and capillary-driven experiments. Highly hydrophobic double-sided adhesive tape (Stiko, Silkstone SA, Buenos Aires, Argentina) was used to fix the paper strips in all experiments. All measurements were made under controlled room conditions: 24 °C and 50 % relative humidity.

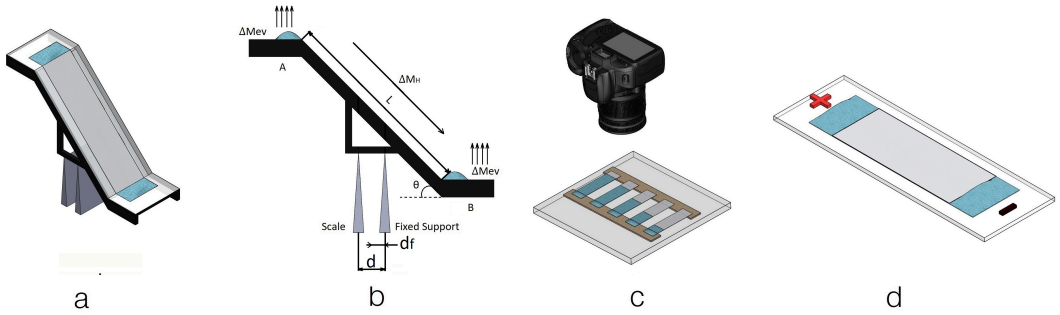

Figure B.2: Experimental setups of three different measurements: hydrostatic pressure-driven flow (a, b), capillary-driven flow (c), and electric current through the saturated paper (d).

B.3.2. Hydrostatic pressure-driven flow experiments

In this section the experiments associated with Eq. B.5 are presented. The experimental setup employed is shown in Fig. B.2a and B.2b, which is similar to the one used in a previous work [Franck et al., 2021]. A scale and a system of blades were used to amplify the measured weight of liquid in the reservoirs. The liquid was driven by the action of gravity through the inclined ramp draining the upper reservoir and filling the lower one. One blade was attached to a fixed support and the other one was placed over the scale. In this configuration, the scale records the change of mass distribution produced by the liquid flow in the paper strip. This scheme amplifies the force over the scale and balances the effects of evaporation, as it will be discussed below. The paper strip of length L, width W, thickness h was tilted at the angle θ (Fig. B.2a). The blades were separated by a distance d, and the center of mass was located at a distance d_f from the fixed blade (Fig B.2b). The mass variation actually recorded by the scale was determined by the flow of liquid between the reservoirs (ΔM_H) and the change in mass due to evaporation (ΔM_{ev}) that occurs at each reservoir, which was assumed to be identical on both sides. It is important to note that these phenomena were not equally amplified by the experimental scheme. While the flow between the reservoirs was amplified as,

$$\Delta M^H = \Delta M_H \frac{L \cos\theta}{d}, \tag{B.11}$$

where superscripts and subscripts denote mass change with and without amplification, respectively, the mass change due to evaporation was amplified as,

$$\Delta M^{ev} = \Delta M_{ev} \frac{d_f}{d}. \tag{B.12}$$

Then, the change in mass effectively recorded by the scale ΔM^s is given by:

$$\Delta M^s = \Delta M^H + \Delta M^{ev}.$$

It is worth to note that the amplification factor in ΔM^{ev} can be minimized by selecting a small value of d_f (placing the reservoirs symmetrically to the fixed support). Moreover, the amplification factors in Eqs.B.11 and B.12 can be experimentally evaluated by a calibration procedure [Franck et al., 2021]. A known mass of liquid ΔM_0 was added to the reservoir 1 (Fig. B.2b) and the mass increase in the scale ΔM^A was registered. Alternatively, the same mass was added to the reservoir 2 and the mass variation ΔM^B was registered. Then, the amplification factors were calculated as:

$$\frac{L\cos\theta}{d} = \frac{\Delta M^A - \Delta M^B}{\Delta M_0} \tag{B.13}$$

and

$$\frac{d_f}{d} = \frac{(\Delta M^B - \Delta M^A)}{2\Delta M_0} \frac{\frac{\Delta M^A}{\Delta M^B} + 1}{-\frac{\Delta M^A}{\Delta M^B} + 1} \tag{B.14}$$

Details about of the derivation of these expressions can be found in the Supplementary Information. For the experiments presented in this work, typical amplification factors were $\frac{L\cos\theta}{d} \approx 25$ and $\frac{d_f}{d} \approx 0.5$. In order to determine ΔM_{ev}, the complete system was supported by the scale by setting the two blades over the scale plate, thus the registered mass change was $2\Delta M_{ev}$. Consequently, the volumetric flow rate Q_H can be calculated by

$$Q_H = \frac{\Delta M_H}{\rho\, \Delta t} \tag{B.15}$$

and the pressure difference ΔP can be related to the height difference by:

$$\Delta P = \rho g L \sin\theta. \tag{B.16}$$

Finally, the values calculated through Eq. B.15 and B.16 can be replaced in Eq. B.5 to obtain the R_H.

B.3.3. Capillary imbibition experiments

In this section the experiments associated with Eq. B.8 are presented. The employed experimental setup (Fig. B.2c) is similar to the one used by [Elizalde et al., 2016]. In these experiments, the wetting front position is recorded over time, which enables the calculation of the effective capillary radius R_C (Eq. B.8). To determine R_C, the contact angle was considered as $\theta = 0$ [Elizalde et al., 2016] and the effective surface tension of the deionized water in paper, $\gamma = 40 \times 10^{-3}\,\mathrm{N/m}$. This value of surface tension is smaller than the obtained for pure water ($\sim 74 \times 10^{-3}\,\mathrm{N/m}$), probably due to the dissolution of some components present in the paper fibers [Elizalde et al., 2016]. The effective surface tension was obtained through additional experiments, which are reported in the Supplementary Information.

Ten rectangular paper strips for each type of paper were laser cut 10 mm width and 30 mm length and were mounted over a glass support. Hydrophobic double-sided adhesive tape was placed at the ends to fix the strips and to delimit the water reservoir. The strips were arranged keeping an air gap between the glass avoiding edge effects that could alter the imbibition flow [Schaumburg and Berli, 2019].

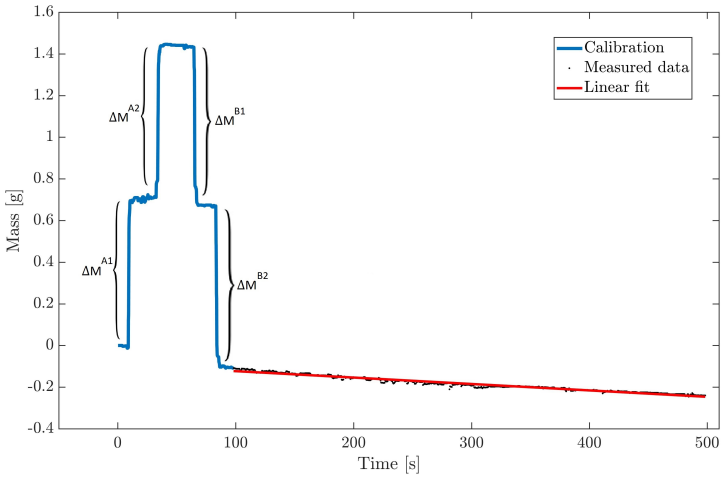

Figure B.3: Calibration process (blue line), determining ΔM^A and ΔM^B variations when known volume droplets are placed in reservoirs A and B respectively. This procedure can be used to obtain amplification factors of the system. Stabilized region (black dots) can be used to measure the flow rate through the paper strip.

Experiments were recorded by using a high resolution digital camera (Canon EOS 1000D). The microfluidic strips were placed horizontally and back-lit with a white LED lamp where irradiation was kept on a low value to avoid temperature increase. The camera was placed vertically at a distance of 30 cm, connected to a PC, and set to burst mode. The spatial resolution was 36 µm and the time resolution was 12 frames per minute. Experimental runs start when a small volume of

deionized water was poured into the inlet reservoir. Image postprocessing to extract the fluid front position as a function of time was implemented as follows: (i) the area of interest was taken as the central 90% of each paper strip width to avoid edge effects; (ii) paper strip area was processed to obtain a normalized grey scale matrix. The procedure involves subtraction of the first image to each image and then normalization by the last one. The resulting matrix was laterally averaged, thus obtaining a longitudinal saturation profile; (iii) the front position in each profile was determined at 25 % of saturated luminosity value.

B.3.4. Electrical resistance experiments

In this section the experiments associated with Eq. B.10 are presented. Electrically-driven measurements were carried out to determine the resistance of the saturated paper (Fig. B.2d). Different electrolyte solutions were used to measure different free solution conductivities, in order to improve the estimation of the left hand side (LHS) of Eq. B.10. Platinum electrodes were connected to the liquid reservoirs, and a constant difference potential was applied through the paper strips, which were $10\,\text{mm}$ width and $40\,\text{mm}$ length. Low voltages ($\approx 10\,\text{V}$) were used to minimize the effects of both Joule heating and EO flow. Free solution liquid resistivities (ρ) were measured with a conductivity meter. To extend the range of solution concentration that can be used in the experiments, electric resistance was measured in a calibrated capillary by applying $10\,\text{V}$ difference potential using platinum electrodes.

B.4. Results and discussion

B.4.1. Experimental results

Hydrodynamic experiments were performed as discussed in section B.3.2 to assess the LHS of Eq.B.5. Figure B.3 present the results of these measurements. The first part of the plot, colored in blue, corresponds to the calibration of the system. After completely filling the paper strip with water (not shown in the figure), two $50\,\mu\text{L}$ drops were consecutively placed in the upper reservoir. The scale measured a mass increase ΔM^{A1} and ΔM^{A2} respectively. The opposite occured when the drops were placed in the lower reservoir: a reduction of the mass was recorded. The amplification factors can be determined by averaging the measured values of ΔM^A, ΔM^B and using Eqs. B.13 and B.14. Afterwards, the liquid steadily flowed from the highest to the lowest reservoir, while data were recorded over time (black dots), after a small initial step allowed for system stabilization. The curve slope was determined with a linear fit (red line) and then used to

obtain R_H in Eq. B.5.

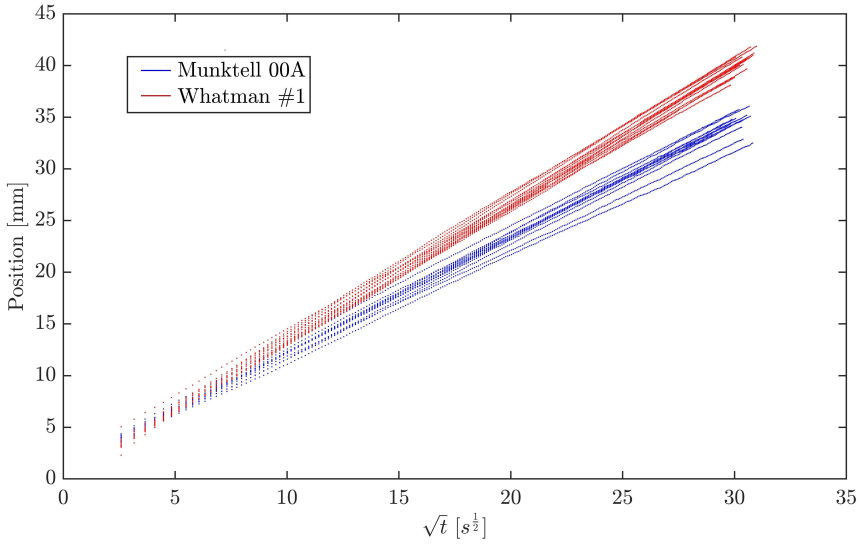

Figure B.4: Fluid front position as a function of square root of time, for the capillary filling of Whatman #1 and Munktell 00A papers along the machine direction. Different slopes indicate typical variations of R_C and D values obtained in identical paper strips (Eqs. (B.8) and (B.9), respectively).

The measured ΔM^s value in this case was $\approx 3.4 \times 10^{-4}$ g/sec. The mass flow and evaporation amplification factors were 29 and -0.69, respectively. The negative sign of d_f means that the reservoirs center of mass is at the right of the fixed blade (Fig. B.2b). Certainly, the center of mass of the whole system is however between the blades to ensure mechanical stability. Furthermore, the ΔM_{ev} measured in this case was 3.33×10^{-5} g/sec. It is important to note that this value is comparable to, even larger than, the hydrodynamic flow rate through the paper strip (ΔM_H =1.25 $\times 10^{-5}$ g/sec) obtained from Eq. B.11. The proposed experimental setup allows one to clearly distinguish between both magnitudes given the high ratio between the respective amplification factors.Capillary filling experiments were performed as discussed in section B.3.3 to asses the LHS of Eq. B.8. Figure B.4 shows several experiments of the fluid front imbibition dynamics for different substrates (Whatman # 1 and Munktell 00A). The squared position as a function of time shows a linear correlation ($L^2 = Dt$), as it is expected for systems satisfying the the Lucas-Washburn law ([Lucas, 1918], [Washburn, 1921]). In fact, the slope in this figure can be associated with a diffusive coefficient D (known as Washburn coefficient) that depends on the paper substrate and physical properties of the liquid (Eq. B.8). The measured values are summarized in Table C.1. Two groups of lines can be identified in Figure B.4, which correspond to the different paper substrates. The dispersion of D values for each paper corresponds to that found in previous works [Elizalde et al., 2016], which is around 7%. The average of D values, however, are smaller than those found on such previous work, due to the use of laminated paper strips on

both sides, which modifies the imbibition dynamics.

The last set of experiments corresponds to the electrical conductivity measurements made for both capillary tube (free solution) and paper substrates. The results obtained via direct measurements with the conductimeter and through the capillary matched those theoretically predicted for the electrolyte concentration at room temperature. Figure B.5 shows the results for several electrolyte solutions with different conductivities. The linearity of the plot indicates good data correlation, as well as negligible interference from Joule heating effects or EO flow.

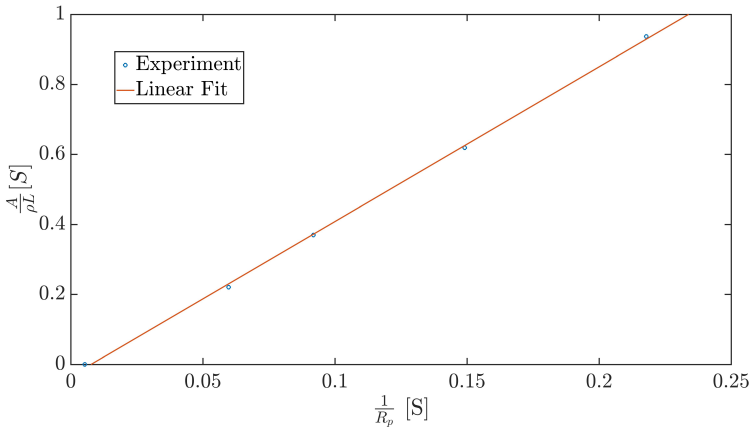

Figure B.5: Calculated free flow conductance as a function of the electric conductance in Whatman #1 substrate. Constriction factor (C) can be obtained from the slope of the linear fit, according to Eq. (B.10).

B.4.2. Pore size distribution

Three different PDFs were tested in order to optimize the description of pore size distribution: (i) bimodal distribution consisting in two delta Dirac's functions that represent the radii with an equal probability of occurrence ; (ii) arcsine distribution, which models radii as an oscillating sine wave between R_{max} and R_{min}); and (iii) log-normal continuous probability distribution. Fig. B.6 a and b show an schematic representation of these distributions. These distributions can be completely characterized by two free parameters, and they were have been previously used to describe similar systems [Sharma and Ross, 1991, Berli et al., 2017, Lei et al., 2021, Apostolopoulou et al., 2020, Aramideh et al., 2018]. Bimodal and arcsine distributions have the advantage of being physically and mathematically simple; both density functions can be analytically handled. However, the range of pore sizes they can explore are bounded (discrete in the case of the bimodal), which limits the description of the pore morphology arising in paper substrates. On the other hand, the log-normal distribution is more complex to handle, but it entails the possibility of wide and continuum variations of pore sizes (Fig. B.6 a), which allows one to reproduce the geometry of the

substrate with greater precision. The log-normal distribution will be further described next; while the description both bimodal and arcsine distributions are reported in the Supplementary Information.

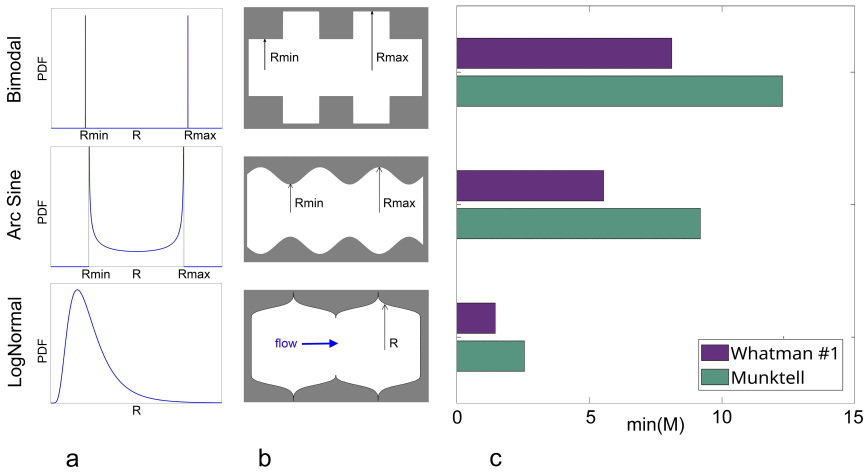

Figure B.6: PDFs explored in modeling: (a) plots of probability densities as a function of radius, (b) schematic representations of pore shapes and characteristic radii, (c) performance of each PDF to describe experimental data from two different substrates, as characterized by the χ^2 test.

The log-normal PDF is defined as:

$$f(R) = \frac{1}{R\sigma\sqrt{2\pi}} e^{-\frac{(\ln R - \mu)^2}{2\sigma^2}} \tag{B.17}$$

where the random variable R represents a specific radius. The parameters μ and σ define the arithmetic mean ($E[R]$) and variance ($Var[R]$) as follows:

$$E[R] = e^{\mu + \frac{\sigma^2}{2}} = X \tag{B.18}$$

$$Var[R] = e^{2\mu+\sigma^2}(e^{\sigma^2} - 1) \tag{B.19}$$

To evaluate the performance of the model with this radius distribution, a figure of merit M was constructed using the predicted results for the three performed experiments. The measured values of R_H, R_C and C were compared against the model predicted values $R_H(\mu, \sigma)$, $R_C(\mu, \sigma)$ and $C(\mu, \sigma)$, respectively, for different combinations of μ and σ. Each predicted value can be calculated using the PDF to evaluate the probability moments (Eq. (B.4)) in Eqs. (B.5), (B.8) and (B.10), respectively. The differences were weighed by the experimental dispersion of each magnitude to obtain a Chi-square type distribution [Press et al., 1986]. The final expression of the figure of merit

was,

$$M(\mu,\sigma) = \frac{(R_H - R_H(\mu,\sigma))^2}{Var[R_H]} + \frac{(R_C - R_C(\mu,\sigma))^2}{Var[R_C]} + \frac{(C - C(\mu,\sigma))^2}{Var[C]}$$

Since there are three measured values and two free parameters, this distribution has a degree of freedom of one, in which the 95% confidence level region is achieved for values of $M < 3.84$ [Abramowitz and Stegun, 1965].

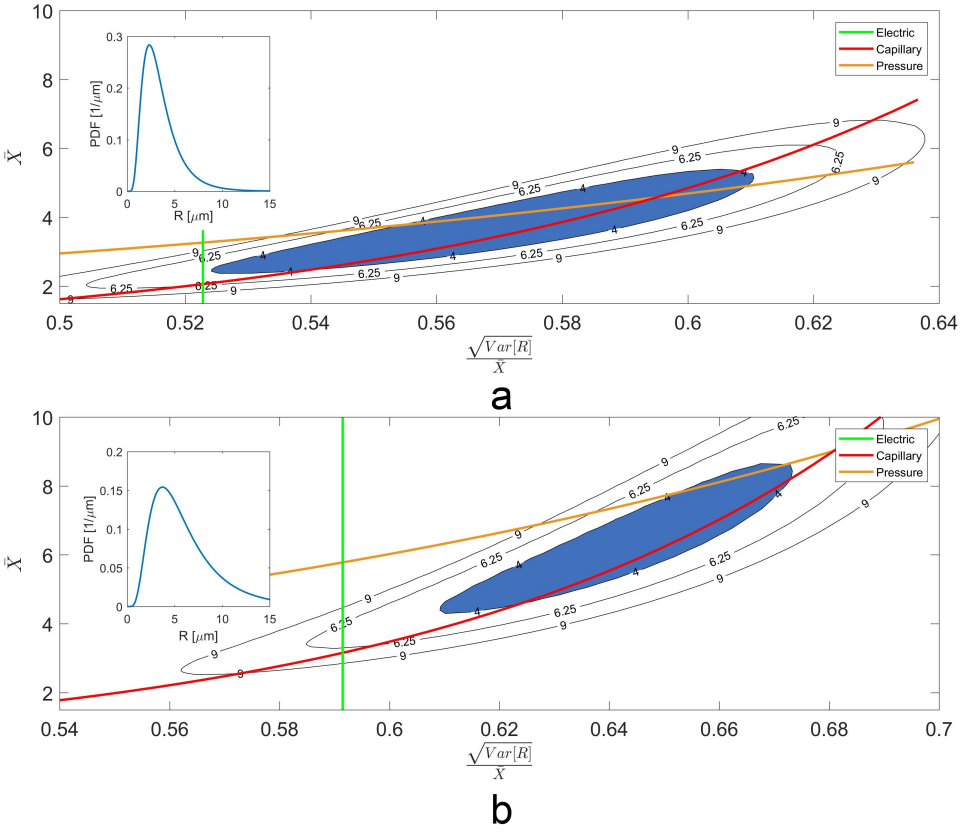

Figure B.7: Contour map values of M using the log-normal distribution for Whatman #1 (a) and Munktell 00A (b). Solid lines indicate the values for which the parameter combination of PDF reproduces the experimental results of R_H (orange line), R_C (red line), and C (green line). The colored (blue) region corresponds to $M < 3.84$, which represents the 95% confidence region for the predicted parameters. The insets on the left show the optimal log-normal PDF that produce the minimum value of M.

Figure B.7 shows contour maps of M obtained by using the log-normal distribution, for the two paper substrates. The results are presented in the transformed variables X and $\sqrt{Var[R]}/X$ for a better visualization. This configuration also enables a direct comparison to other probability distributions (see the Supplementary Information for details). The minimum M values obtained for different PDFs are shown in Fig. B.6d for the two paper substrates. From these results, it is clear that the log-normal distribution has a better performance to simultaneously represent the response of the three experiments. The optimum parameter combination (minumum M) can be

used to obtain the model prediction for each experiment. The overall results are summarized in Table C.1. Also in Figure B.7, the combinations of μ and σ that satisfy $R_H - R_H(\mu,\sigma) = 0$ (orange line), $R_C - R_C(\mu,\sigma) = 0$ (red line), and $C - C(\mu,\sigma) = 0$ (green line) are shown. These lines indicate the regions where the model independently reproduces each experimental result. The blue colored zones are limited by $M < 3.84$ and indicate the 95% confidence regions for the predicted parameters. Ideally, all the three lines should cross in a single point, which means that for different experiments the model predicts the same radius distribution, with an unique combination of mean radius and variance. The distance between the crossing points is an indicator of the model accuracy for the chosen PDF. Particularly, electrical measurements (vertical green lines) indicate that the factor C is independent of the mean value of the distribution X. In fact, a multiplicative factor in the distribution radius does not change neither C nor the $\sqrt{Var[R]}/X$ parameter.

On the other hand, results from capillary-driven flow (red line) and hydrostatic pressure-driven flow (orange line) depend on both variables. Regarding paper substrates, one observes that data cloud for Munktell has a larger error than for Whatman #1, which means that the model capture the experiments with lower fidelity for Munktell than for Whatman #1. In fact, the minimum of the function M determine the PDF parameters that better describe the experimental data. In the case of the Whatman #1 paper, the minimum corresponds to $\mu = 1.12$ and $\sigma = 0.52$, which in turn correspond to $X = 3.5\,\mu\text{m}$ and $\sqrt{Var[R]} = 6.1\,\mu\text{m}$ (see the inset in Fig. B.7a). In the case of Munktell paper, the optimum values are $\mu = 1.65$ and $\sigma = 0.586$, which correspond to $X = 3.5\,\mu\text{m}$ and $\sqrt{Var[R]} = 15.5\,\mu\text{m}$ (see the inset in Fig. B.7b).

B.4.3. Comparison between different models

In order to emphasize the advantages the multiphysic model, we present the direct link between the PDFs and some well-known parameters from single-physics models, such as Darcy's permeability K, Washburn coefficient D, and electrokinetic potential ζ. Additionally, the constriction factor (C), the equivalent radii for hydrodynamic (R_H) and capillary phenomena (R_C) are reported for both substrates. To summarize this information, two types of data are presented in Table C.1: (i) from measurements, with values and uncertainties related to each set of experiments (*Measurement*) and (ii) from model, using the best fitted values according to minimum M (*Model prediction*). The results in Table C.1 show that the deviations between the measurement and the model predictions are relatively small, most of them within the range of the measurement uncertainty. It is worth to mention here that the model captures the fact that R_H is about ten times larger than R_C in paper substrates.

Table B.1: Parameters for single-physics models related to different radii statics in the present work. Electroosmotic permeability (K_{eo}) was obtained from [Franck et al., 2021] for pH=4.7 solution at $E = 2.5\,\mathrm{kV/m}$.

Substrate		**Whatman #1**		**Munktell 00A**	
Magnitude	Definition	Measurement	Model prediction	Measurement	Model prediction
Equivalent hydrodynamic radius [μm]	$R_H = \sqrt{\frac{1}{<R^{-4}><R^2>}}$	0.86 ± 0.08	0.79	1.1 ± 0.1	0.93
Darcy permeability $\times 10^{-14}$[m^2]	$K = \frac{R_H^2}{8}$	9.3 ± 0.9	7.8	13 ± 1	10.9
Equivalent capillary radius [μm]	$R_C = \frac{1}{<R^{-4}><R^3>}$	0.089 ± 0.008	0.096	0.064 ± 0.006	0.07
Washburn coefficient $\times 10^{-6}$ [$\frac{\mathrm{m}^2}{\mathrm{s}}$]	$D = \frac{\gamma \cos\theta R_C}{2\mu_\ell}$	1.8 ± 0.2	1.9	1.3 ± 0.1	1.4
Constriction factor	$C = < R^2 >< R^{-2} >$	2.6 ± 0.3	3.1	3.3 ± 0.3	4
Zeta potential [mV]	$\boldsymbol{\zeta_P} = \frac{K_{eo}\mu_\ell C}{\epsilon\phi}$	2.8 ± 0.3	3.3	5.3 ± 0.5	6.4

This apparent discrepancy, which is known in the microfluidics community [Alava et al., 2004], is inherent to the extrapolation of capillary-driven flow models from single tubes to porous media: the main pitfall is considering a unique pore radius for both Laplace pressure and fluid resistance. Regarding EO flow, one may note that the value obtained for the constriction factor is comparable to the value of tortuosity calculated for electrokinetic and EO phenomena by [Gerlero et al., 2021b], while being different to those predicted for fluid transport [Matyka et al., 2008]. Finally, it is necessary to remark that these reported values correspond to both sides laminated paper, and could differ from other results where paper was not laminated or single side-laminated [Noh and Phillips, 2010, Elizalde et al., 2016].

B.5. Conclusions

This paper proposes an innovative approach that considers the pore space as a bundle of periodically constricted tubes modelled through a PDF of the porous radii, which can simultaneously represent four different transport phenomena in porous substrates: capillary filling, pressure-driven flow, electric transport, and electroosmotic flow. The mathematical basis of the model were described and the model predictions were experimentally validated by using well-known filter pa-

pers. The proposed model enabled the characterization of porous substrates by means of a reduced number of parameters (two free parameters describing the radius distribution). In relation to single-physics models, the multiphysics approach avoids the concept of tortuosity (τ), which is normally used as an adjustment variable. Although τ is a widely used parameter, its value strongly depends on the experiment under consideration and can be much larger than expected for the paper morphology. In contrast, the constricted tube model can reasonably reproduce the results obtained in all the experiments studied using a single PDF.

Typical parameters values for Whatman #1 and Munktell 00A papers are provided for double laminated substrates aimed to improve the prediction capability of most of μ-PADs developers working with such materials. The fact that fluid and charge transport phenomena are satisfactorily described by a single topological scheme confirms that the proposed model entails a more generalized view of the underlying physics.

This model's feature definitely improves the prediction capabilities because, performing only two of the proposed experiments, a given substrate can be fully characterized for any of the studied processes (capillary filling, pressure driven flow, electroosmotic flow, and electric current driving). Furthermore, after having characterized different substrates, developers can use different combination of papers for creating arbitrary multi-substrates arrangements. The behavior of these complex heterogeneous μPADs can be predicted through an equivalent PDF made as the weighted sum of single paper PDFs. Finally, it is important to note that the proposed model can be applied to porous media different from paper by simply selecting the suitable pore distribution function.

Acknowledgements

This research was supported by CONICET, ANPCyT (Grant PICT 2018-02920), UTN (Grant PID ASUTNFE0005525), and UNL (Grant CAI+D 50620190100114LI), Argentina.

Conflict of interest

The authors declare that they have no conflict of interest.

Data avilability statement

The datasets generated during and analysing the current study are available from the corresponding author on reasonable request.

Supplementary information

Supplementary information providing experimental data on surface tension measurements, as well as the results of χ^2 test of other PDFs, can be found in the on-line version of the article.

References

M. Abramowitz and I. A. Stegun. *Handbook of Mathematical Functions*. American Association of Physics Teachers, 01 1965.

M. Alava, M. Dubé, and M. Rost. Imbibition in disordered media. *Adv Phys*, 53(2):83–175, Mar. 2004.

M. Apostolopoulou, M. Stamatakis, A. Striolo, R. Dusterhoft, R. Hull, and R. Day. A novel modeling approach to stochastically evaluate the impact of pore network geometry, chemistry and topology on fluid transport. *Transport Porous Med*, 136(2):495–520, 2020.

S. Aramideh, P. P. Vlachos, and A. M. Ardekani. Pore-scale statistics of flow and transport through porous media. *Phys. Rev. E*, 98:013104, Jul 2018.

G. Archie. The Electrical Resistivity Log as an Aid in Determining Some Reservoir Characteristics. *T Soc Petrol En AIME*, 146(01):54–62, 1942.

J. Bear. *Dynamics of Fluids in Porous Media*. American Elsevier Publishing Company, New York, USA., 1972.

J. Bear and A. H.-D. Cheng. *Modeling groundwater flow and contaminant transport*, volume 23. Springer Science & Business Media, Dordrecht, Netherlands, 2010.

C. Berg. Permeability description by characteristic length, tortuosity, constriction and porosity. *Transport in Porous Media*, 103:381–400, 2014.

C. L. Berli, M. Mercuri, and M. G. Bellino. Modeling the abnormally slow infiltration rate in mesoporous films. *Phys Chem Chem Phys*, 19(3):1731–1734, 2017.

A. E. Bussian. Electrical conductance in a porous medium. *Geophysics*, 48(9):1258–1268, 1983.

A. Böhm, F. Carstens, C. Trieb, S. Schabel, and M. Biesalski. Engineering microfluidic papers: Effect of fiber source and paper sheet properties on capillary-driven fluid flow. *Microfluid Nanofluid*, 16:789–799, 05 2014.

J. Cai, E. Perfect, C.-L. Cheng, and X. Hu. Generalized modeling of spontaneous imbibition based on hagen–poiseuille flow in tortuous capillaries with variably shaped apertures. *Langmuir*, 30(18):5142–5151, May 2014.

J. Cai, Y. Chen, Y. Liu, S. Li, and C. Sun. Capillary imbibition and flow of wetting liquid in irregular capillaries: A 100-year review. *Advances in Colloid and Interface Science*, 304:102654, 2022. ISSN 0001-8686.

B. M. Cummins, R. Chinthapatla, F. S. Ligler, and G. M. Walker. Time-dependent model for fluid flow in porous materials with multiple pore sizes. *Anal Chem*, 89(8):4377–4381, 2017.

A. Duda, Z. Koza, and M. Matyka. Hydraulic tortuosity in arbitrary porous media flow. *Phys. Rev. E Stat. Nonlin. Soft Matter Phys.*, 84(3 Pt 2):036319, Sept. 2011.

E. Elizalde, R. Urteaga, and C. L. A. Berli. Precise capillary flow for paper-based viscometry. *Microfluid Nanofluid*, 20(10):1–8, 2016.

M. Ezzatabadipour and H. Zahedi. A novel method for streamline-based tortuosity calculation and investigation of obstacles shape effect on tortuosity in porous media with random elliptical obstacles using lattice boltzmann method. *Transport Porous Med*, 136(1):103–124, 2021.

N. Franck, F. Schaumburg, P. A. Kler, and R. Urteaga. Precise electroosmotic flow measurements on paper substrates. *Electrophoresis*, 42(7-8):975–982, 2021.

G. S. Gerlero, S. M. Damián, F. Schaumburg, N. Franck, and P. A. Kler. Numerical simulations of paper-based electrophoretic separations with open-source tools. *Electrophoresis*, 42:1543–1551, 2021.

G. S. Gerlero, A. R. Valdez, R. Urteaga, and P. A. Kler. Validity of capillary imbibition models in paper-based microfluidic applications. *Transport Porous Med*, pages 1–20, Jan. 2022.

B. Ghanbarian, A. G. Hunt, R. P. Ewing, and T. E. Skinner. Universal scaling of the formation factor in porous media derived by combining percolation and effective medium theories. *Geophys Res Lett*, 41(11):3884–3890, 2014.

J.-B. Gorce, I. J. Hewitt, and D. Vella. Capillary imbibition into converging tubes: beating washburn's law and the optimal imbibition of liquids. *Langmuir*, 32(6):1560–1567, 2016.

S. Gruener, Z. Sadjadi, H. E. Hermes, A. V. Kityk, K. Knorr, S. U. Egelhaaf, H. Rieger, and P. Huber. Anomalous front broadening during spontaneous imbibition in a matrix with elongated pores. *P Natl Acad Sci USA*, 109(26):10245–10250, 2012.

D. C. Herrick and W. D. Kennedy. Electrical efficiency—a pore geometric theory for interpreting the electrical properties of reservoir rocks. *Geophysics*, 59(6):918–927, 1994.

M. Kozeny. Uber kapillare leitung des wassers im boden. *Sitzber. Akad. Wiss. Wein, Math-naturw*, 136:Abt. II a, P. 277, 1927.

J. Lei, Z. Xu, F. Xin, and T. J. Lu. Dynamics of capillary flow in an undulated tube. *Phys Fluids*, 33(5):052109, 2021.

Z. Liu, X. He, J. Han, X. Zhang, F. Li, A. Li, Z. Qu, and F. Xu. Liquid wicking behavior in paper-like materials: mathematical models and their emerging biomedical applications. *Microfluid Nanofluid*, 22(11):1–20, 2018.

R. Lucas. Ueber das Zeitgesetz des kapillaren Aufstiegs von Flüssigkeiten. *Colloid & Polymer Science*, 23(1):15–22, 1918.

B. D. MacDonald. Flow of liquids through paper. *J Fluid Mech*, 852:1–4, 2018.

V.-P. Mai, C.-H. Ku, and R.-J. Yang. Porosity estimation using electric current measurements for paper-based microfluidics. *Microfluid Nanofluid*, 23(4):1–10, 2019.

R. Masoodi and K. M. Pillai. Darcy's law-based model for wicking in paper-like swelling porous media. *AIChE J*, 56(9):2257–2267, 2010.

M. Matyka, A. Khalili, and Z. Koza. Tortuosity-porosity relation in porous media flow. *Phys Rev E*, 78(2):026306, 2008.

S. Modha, C. Castro, and H. Tsutsui. Recent developments in flow modeling and fluid control for paper-based microfluidic biosensors. *Biosens Bioelectron*, page 113026, 2021.

M. F. Mora, C. D. Garcia, F. Schaumburg, P. A. Kler, C. L. Berli, M. Hashimoto, and E. Carrilho. Patterning and modeling three-dimensional microfluidic devices fabricated on a single sheet of paper. *Anal Chem*, 91(13):8298–8303, 2019.

H. Noh and S. T. Phillips. Metering the capillary-driven flow of fluids in paper-based microfluidic devices. *Anal Chem*, 82(10):4181–4187, 2010.

A. Piovesan, R. Nicasy, T. Arens, B. Dequeker, J. Soete, C. Achille, R. Dochy, C. Parra-Cabrera, R. Ameloot, P. Verboven, and B. Nicolai. Multiscale modelling of capillary imbibition in 3d-printed porous microfluidic channels. *Microfluid Nanofluid*, 26(3):1–15, 2022.

W. H. Press, W. T. Vetterling, S. A. Teukolsky, and B. P. Flannery. *Numerical recipes*, volume 818. Cambridge university press, Cambridge, UK., 1986.

R. F. Probstein. *Physicochemical hydrodynamics: an introduction*. John Wiley & Sons, Newark, NJ, USA., 2005.

M. Reyssat, L. Courbin, E. Reyssat, and H. A. Stone. Imbibition in geometries with axial variations. *J Fluid Mech*, 615:335–344, 2008.

A. Salama, J. Cai, J. Kou, S. Sun, M. F. El-Amin, and Y. Wang. Investigation of the dynamics of immiscible displacement of a ganglion in capillaries. 2021.

F. Schaumburg and C. L. Berli. Assessing the rapid flow in multilayer paper-based microfluidic devices. *Microfluid Nanofluid*, 23(8):1–10, 2019.

F. Schaumburg, P. A. Kler, and C. L. A. Berli. Numerical prototyping of lateral flow biosensors. *Sensor Actuat B-Chem*, 259:1099–1107, 2018a.

F. Schaumburg, R. Urteaga, P. A. Kler, and C. L. Berli. Design keys for paper-based concentration gradient generators. *J chromatogr A*, 1561:83–91, 2018b.

F. Schaumburg, P. A. Kler, and C. L. Berli. Comprehensive model of electromigrative transport in microfluidic paper based analytical devices. *Electrophoresis*, 41(7-8):598–606, 2020.

A. E. Scheidegger. *The Physics of Flow Through Porous Media (3rd Edition)*. University of Toronto Press, Toronto, Canada., 1974.

R. Sharma and D. S. Ross. Kinetics of liquid penetration into periodically constricted capillaries. *J Chem Soc Faraday T*, 87(4):619–624, 1991.

F. Shen, M. Ai, Z. Li, X. Lu, Y. Pang, and Z. Liu. Pressure measurement methods in microchannels: advances and applications. *Microfluid and Nanofluid*, 25(5):1–31, 2021.

T. Tesfaye and A. Hussen. Microfluidic paper-based analytical device (μpad) fabricated by wax screen printing technique for the determination of nitrite and nitrate ion in water samples. *Microfluid Nanofluid*, 26(3):1–13, 2022.

R. Urteaga, E. Elizalde, and C. L. A. Berli. Transverse solute dispersion in microfluidic paper-based analytical devices (μPADs). *Analyst*, 143:2259–2266, 2018. doi: 10.1039/c8an00149a.

E. W. Washburn. The dynamics of capillary flow. *Physical review*, 17(3):273, 1921.

W.-B. Young. Analysis of capillary flows in non-uniform cross-sectional capillaries. *Colloid Surface A*, 234(1-3):123–128, 2004.

Anexo C

A simple method for the assessment of electrophoretic mobility in porous media

El artículo presentado a continuación ha sido publicado en la revista **Electrophoresis**.

N. Franck, L. Vera Candioti, G. S. Gerlero, R. Urteaga, P. A. Kler. A simple method for the assessment of electrophoretic mobility in porous media. *Electrophoresis*, 45(7–8), 589–598, 2023. https://doi.org/10.1002/elps.202300180.

A simple method for the assessment of electrophoretic mobility in porous media

Nicolás Franck[1,2], Luciana Vera Candioti[3], Gabriel S. Gerlero[1,4], Raul Urteaga[2], Pablo A. Kler[1,5],

[1] CIMEC (Universidad Nacional del Litoral–CONICET), Colectora RN 168 Km 472, S3000GLN Santa Fe, Argentina

[2] Instituto de Física del Litoral (IFIS Litoral, UNL–CONICET), Güemes 3450, S3000GLN Santa Fe, Argentina

[3] Departamento de Ciencias Biológicas, Cátedra de Bromatología y Nutrición - (FBCB,UNL–CONICET), Ciudad Universitaria - RN168, S3000GLN Santa Fe, Argentina

[4] Universidad Nacional de Rafaela, Bv. Roca 989, S2300KCJ Rafaela, Santa Fe, Argentina

[5] Departamento de Ingeniería en Sistemas de Información, Facultad Regional Santa Fe, Universidad Tecnológica Nacional, Lavaisse 610, Santa Fe, Argentina

Abstract

Developing paper-based electrophoretic methods involve dealing with significant uncertainty levels when compared to their capillary counterparts. Critical information for developing these kinds of methods are the electrophoretic mobility of background electrolytes and samples. This work presents the design and characterization of a device for measuring the electrophoretic mobilities of dyes in porous media. The device was developed with the aim of validating a previously presented model and also proposing a protocol for the straightforward determination of electrophoretic mobilities in porous media when open-channel values are already known. Whatman #1 paper was used as a model substrate as far as it is the most common porous medium substrate for paper-based electrophoresis. The device was designed using a numerical simulation–assisted

approach, utilizing OpenFOAM® and specific solvers for capillary transport and electromigration, namely `porousMicroTransport` and `electroMicroTransport` respectively. The electrophoretic mobilities of five dyes were analyzed experimentally with the proposed device. To establish appropriate comparative values at different pHs, experiments in fused silica capillaries were also performed. An effective parameter model for describing the electrophoretic behaviour of dyes in porous media, i.e. the constriction factor, was found consistent with previous reports for the Whatman #1 paper. This consistency was found after considering (via direct measurements) the chromatographic effect of the medium over each dye. Consequently, the recorded values hold significant worth due to their potential for direct application in designing new experiments or devices in Whatman #1 paper. With the validation of the model through the experiments with the proposed device, those researchers interested on developing electrophoretic methods in porous substrates can make use of the open-channel electrophoretic mobilities reported in the literature, or in the well-known software databases, and correct them for the media of interest just by performing two simple characterization steps.

C.1. Introduction

Understanding the electrochemical properties of analytes is of great importance in several scientific fields where analytical chemistry is involved [Gerlero et al., 2021b]. The precise characterization of molecules is essential to carry out rational designs of biosensors to determine analytes of interest in biological and environmental samples. Recently, paper-based electrophoretic microfluidic analytical devices (e-μPADs) have become relevant for the analysis of proteins [Hennig et al., 2021], DNA [Rosenfeld and Bercovici, 2018], blood [Sena-Torralba et al., 2021] as well as environmental analytes [Kung et al., 2019, Casado-Carmona et al., 2019]. One of the challenges faced when designing these devices is the uncertainty of the physicochemical properties of the analytes, buffers, and solvents when they interact inside a porous medium [de los Santos-Ramirez et al., 2023]. For this reason, reliable and validated models are necessary in order to take advantage of all the information available for open-channel systems, e.g. electrophoretic mobilities reported in the well-known software databases [Hirokawa et al., 1983]. Such models are not abundant in literature, but their number is growing in the last few years [Franck et al., 2022, Novotnỳ and Gaš, 2021].

In parallel to the broad range of applications of e-μPADs [Schaumburg et al., 2020b], such technology also offers a wide range of detection techniques [Nguyen et al., 2020]. However, for easy and fast point-of-need applications, instrument-free detection techniques are desirable

[Schaumburg et al., 2022]. In this sense, as it was for the pioneering pregnancy tests, colour-based detection systems clearly represent such a paradigm[Wu et al., 2022]. However, as it was extensively discussed in the literature, the development of most paper-based microfluidics technologies was based on empirical methodologies [Schaumburg et al., 2018b], conspiring with their reliability and analytical robustness [Schaumburg et al., 2018a]. In order to improve this situation for instrument-free e-μPADs, a deeper knowledge of the electrophoretic behaviour of colourants and dyes are necessary, as well as reliable numerical models for prediction and optimization of designs and operational parameters [Damián et al., 2019].

Different dyes are frequently used in combination with electrophoretic separations, e.g. nucleic acid staining dyes are used for detecting nucleic acids in electrophoresis gels, used as indicators of fragment size along with quantity and quality of DNA based on the fluorescent signal present within the gel [Haines et al., 2015]; dye precipitation provided effective methods for concentrating urine of low to intermediate protein content prior to a two-dimensional electrophoresis analysis [Zukas and Breksa III, 2005]; and also, electrophoretic techniques have even been used to detect dyes that act as pollutants [Ali et al., 2015]. Several authors have analyzed, among other parameters, electrophoretic mobilities of different types of food dyes in open-channel microfluidic and capillary systems [Lee et al., 2008, Álvarez et al., 2017, Jager et al., 2005] but there exist some discrepancies in the reported values. Binding interactions of anionic and cationic dyes have been studied in gel electrophoresis, observing complexing and precipitation reactions when using a nanoporous elastic gel immersed in an electrolyte buffer solution, electrophoretic mobilities have been characterized also both theoretically and experimentally [Bikos and Mason, 2019]. Despite the existent applications that combine dyes and electrophoretic separations, more work is still necessary for developing instrument-free e-μPADs for quantitative analysis [Khurana and Santiago, 2008].

This work will focus on designing a device capable of measuring the electrophoretic mobilities of different dyes in a porous medium by following a numerically assisted design process. The chosen material for the e-μPADs is the Whatman #1 paper, as far as it is the most used material for these kinds of devices [Zhu et al., 2023]. In parallel, as model analytes, different dyes were selected due to their importance in the developing of instrument-free e-μPADs, but also taking advantage of such characteristics to develop an experimental setup depending on a single commercial camera as the whole detection system [Schaumburg et al., 2022].

With the set of measured values in Whatman #1 paper and the values obtained under the same pH and ionic strength conditions for the same dyes in CE, a previously developed model [Franck et al., 2022] is validated in order to demonstrate a straightforward correlation between porous

media and open channel electrophoretic mobilities. The effects of chromatography (retention factors) were also evaluated to complete a successful validation of the model. The main contribution of this validation is to provide e-μPADs developers with a reliable correlation between open-channel electrophoretic mobilities and its counterpart in porous media. The minimal information needed for using such correlation are the porosity and the constriction factor of the porous medium, and the retention factor of the molecule in such substrate. Having objective certainty about electrophoretic mobilities of dyes in paper and other porous substrates will enable the rapid development of instrument-free detection e-μPADs.

C.2. Mathematical model

In order to develop a correlation between open-channel and porous electrophoretic mobility, a previously developed model is used as template [Franck et al., 2022]. Such model is based on the hypothesis that the porous medium can be modelled as a bunch of periodically constrict non-interconected capillary tubes. Although, this abstraction of the geometry of the porous media (particularly for paper) can be though as an oversimplification, it was demonstrated that the proposed model is at present the first one that can correctly represent simultaneously four physicochemical phenomena, (i.e. electrical conductivity, electroosmotic flow, capillary imbibition and pressure driven flow) within an homogeneous material strategy. In this work we also include the electromigration as another phenomena that can be correctly represented with this model. In parallel, the proposed linear correlation can also be obtained by using any continuous model for porous media, by considering the correct set of characteristic parameters associated to such model.

Electromigrative behavior of a particle is represented through its electrophoretic mobility (μ_e), which is defined as the relationship between the electromigration velocity and the strength of the electric field [Dovhunová et al., 2020]. Consequently, the first approximation to calculate mobilities in porous media is to introduce the concepts of porosity (ϕ) and constriction factor (c_f) [Franck et al., 2022]:

$$\mu_p^0(pH, I) = \left(\frac{\phi}{c_f}\right) \mu_e(pH, I) \tag{C.1}$$

In addition to pH and I, other effects must be considered in experimental conditions, one of them is the EOF that affect the macroscopic measurement of electrophoretic mobilities because its contribution to the overall movement. EOF effects in paper substrates were recently studied at different pHs [Franck et al., 2021]. This effect modifies the measured values by a quantity

equivalent to mobility (μ_{EO}):

$$\mu_p(pH, I) = \mu_p^0(pH, I) + \mu_{EO}(pH, I) \tag{C.2}$$

Finally, to consider the interaction of the dye molecules with the substrate that retards the flow of dyes, electrophoretic mobility described by eq. (C.2) should be corrected using retardation factor [Jaitpal et al., 2022] for each specific dye as follows:

$$\mu_p^{eff}(pH, I) = R_f \mu_p(pH, I) = R_f \left(\frac{\phi}{c_f} \mu_e(pH, I) + \mu_{EO}(pH, I) \right). \tag{C.3}$$

As it was mentioned before, due to the complexity of models [Gerlero et al., 2023] and their implementation, comprehensive approaches for modelling fluid flow, and transport of solutes (including electromigration) in paper-based substrates are not extensively reported in the literature [Gerlero et al., 2021a].

C.3. Materials and Methods

C.3.1. Chemicals

Five dyes were used in the experiments. Methyl Orange and Fast Green FCF were purchased from Sigma-Aldrich Corp. (St. Louis, MO, USA) and Tartrazine, Red Ponceau and Brillant Blue from Fleibor S.A (La Tablada, Buenos Aires, Argentina). Two buffer solutions were used as background electrolytes (BGE) in the CE and paper-based electrophoresis experiments: a pH=5.5 solution of Tris-Acetate (17.5 mM Tris - 20 mM Acetic acid) and pH=9.0 of Ammonium-Acetate (20 mM Ammonium hydroxide- 10 mM Acetic acid). Acetic acid, Tris and ammonium hydroxide were purchased from Laboratorios Cicarelli (Reagent SA, San Lorenzo, Argentina). All solutions were prepared with ultrapure water obtained from an inverse osmosis purifier (Osmoion, Apema SRL, Villa Dominico, Argentina). The pH of the solutions was corroborated with the pH-Meter (Adwa A12, Szeged, Hungary). BGE compositions, and their pH and ionic strength values, were selected according to typical buffers used in paper-based electrophoretic devices [Sena-Torralba et al., 2021] and previous works from our group where EOF and c_f were measured [Franck et al., 2022, 2021]. BGE concentration was set to effectively work as a buffer avoiding electrodispersion of the sample, but with lower enough conductivity to avoid significant thermal deviations due to the Joule effect.

C.3.2. Capillary electrophoresis

All the CE experiments were carried out on a Beckman Coulter MDQ system (Beckman Coulter, Fullerton California, USA) equipped with a UV detector. Separation was performed by applying a normal polarity of 20 kV, employing an uncoated fused-silica capillary (MicroSolv Technology Corporation, Eatontown, NJ, USA) with an inner diameter of 75 µm and a total length of 31 cm (21 cm effective length, Le). The hydrodynamic injection was performed in the cathode by applying a pressure of 34.5 mbar for 5 sec. The cartridge was maintained at 25 °C, and the electropherograms were recorded with the 200 nm wavelength signal. All solutions were filtered through 0.45 µm nylon membranes (Sartorius AG, Gottingen, Germany) before use. Before and between runs, the capillary was successively flushed with 0.1 mol L^{-1} sodium hydroxide (Laboratorios Cicarelli Reagent SA, San Lorenzo, Argentina), ultrapure water, and BGE for 2 min.

C.3.3. Paper-based electrophoresis

Paper geometries were cut from Whatman qualitative filter paper, grade No. 1, 150 mm disks (Cityva, Marlborough, USA). These cuts were performed with a laser cutting machine (40 W CO_2 laser, Lasers Cuyana, San Rafael, Argentina). After cutting hot lamination of substrates was done to avoid evaporation effects. With a commercial lamination machine (DASA LM330, DASA, Caseros, Argentina), lamination was done on both sides of the paper strips using 150 µm thick pouches (Binderplus, China) at 135 °C, at a constant speed of 3.5 mm/s. As it was already demonstrated, under these lamination conditions, the nominal paper porosity (and constriction factor) reported by the manufacturer is not affected significantly [Elizalde et al., 2015, Gerlero et al., 2022]. At both ends of the centre channel (Fig. C.1), symmetric 5 mm spaces were left for liquid reservoirs, by using a shorter lamination pouch on the upper side. The paper device must be placed on a hydrophobic double-sided adhesive tape (Stiko, Silkstone SA, Buenos Aires, Argentina), wider than the detection zone, on a glass plate. The device is placed on the tape in order to avoid spillage of liquid on the glass or the forming of secondary flow channels with low electrical resistance. The electric potential was applied with a Picoammeter/Voltage Source (Keithley 6487, Cleveland, OH, USA), which also measures the intensity of the applied current.

For the R_f measurements, samples and buffers of the same concentrations as in the electrophoretic measurements were used. Rectangular paper strips of 10 mm in width and 40 mm in length were cut and laminated, leaving a 2 mm space for dye input reservoirs.

Experiments were recorded using a high-resolution digital camera (Canon EOS 1000D). The microfluidic devices were placed horizontally and back-lit with a white LED lamp. The camera was placed vertically at a distance of 30 cm, connected to a PC, and set to burst mode. The spatial

resolution was 36 µm and the time resolution was 12 frames per minute.

C.3.4. Device operation

The schematic of the electrophoretic microfluidic device, as depicted in Fig. C.1, comprises three different sections. The bottom section, referred to as the *inlet zone*, contains the buffer mixed with the dye of interest. The *detection zone* serves as the site for the electrophoretic analysis and buffer reservoirs are placed at the ends. The top *outbound zone* contains the capillary pump.

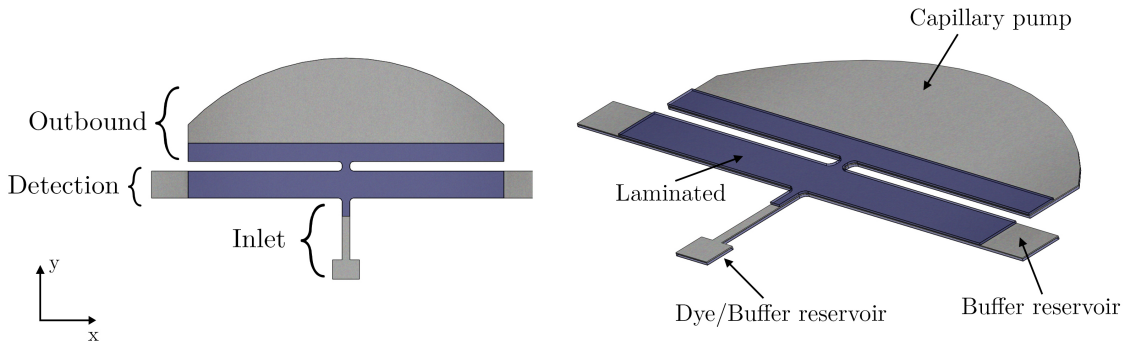

Figure C.1: Paper-based electrophoretic device. The device geometry defines three regions: input, detection, and output. Initially, the dye is introduced through the input zone and is conducted towards the pumping region while the buffer is incorporated on both sides of the detection zone. Then, an inversion of the flow is induced in the input region, which allows the generation of a thin line of dye in the detection region. Finally, high voltage is applied between the ends of the detection region where electrophoresis occurs. The lamination region prevents evaporation during experiments.

The *injection stage* begins when the buffer is simultaneously placed in the reservoirs at the ends of the detection zone. The length of the detection wings plays a crucial role in determining the elapsed time between the injection of buffer in reservoirs to the arrival at the central region. When the fronts are close to meeting, the reservoir in the inlet area is filled with dye diluted in the BGE. The wetting fronts will continue their dynamics and collide so that the device will be completely wet from the outbound zone downwards. The design of the device focuses on providing rapid analysis of analytes while maintaining a compact size. The time required for the dyes to reach the detection zone depends on the length of the inlet zone. Due to the mechanical dispersion of analytes during the injection, the inlet width is limited to a minimum value of 1 mm [Urteaga et al., 2018].

The injection stage produces a characteristic distribution of the dye producing a triangle shape in the detection zone (Fig. C.2A), so a refocusing process is necessary for the sample stack. Next, a configuration change is made to the position of the sources and sinks. The dye inlet is replaced with another capillary pump, made of the same type of paper. The goal is to get a narrow enough

sample line under the laminate. This stage is denominated *focusing stage*. The dye streamlines are determined by the geometric configuration of the inlet and wings, where their hydrodynamic resistances are proportional to their respective lengths. The upper section, which comprises the capillary pump, maintains a continuous pressure difference downstream and allows for the imbibition of buffer and analyte throughout the injection and focusing stages. Once the desired dye distribution is obtained, the outbound zone is filled with liquid to stop the capillary pump and the device is ready for the electrophoretic experiment.

The end of the protocol consists of connecting platinum electrodes in the reservoirs of the detection zone. A constant 500 V potential difference is applied to measure the movement of the dyes under the influence of an electric field. This stage is called the *electrophoretic run stage*. The wings were designed to be long enough to accurately identify dyes with high electrophoretic mobility, while also providing an acceptable number of image sample points and adequate resolution. The width of the detection zone (~ 8 mm) was chosen wide enough to avoid large edge effects when an electric field is applied.

C.3.5. Computational tools

Images obtained from experiments and screenshots of simulations were analyzed with a guide user interface (GUI) program developed in the open-source tool GNU Octave framework [GNU Octave Online, 2022]. To recognize the analytes and determine their spatial position, a method of relative intensity detection was used. The intensity profiles of each dye in each photo were cut at a 50 % intensity value relative to the maximum peak value, and that point established a spatial position. Once the position of the dye is determined as a function of time, a (linear) least squares fit was made. The regression coefficients R^2 obtained were greater than 0.99 in each case. These experiments were repeated and the mean value and the standard deviation were used to represent the dispersion in calculating effective mobility. The experimental dispersion of the data comes mainly from the inherent variability in the properties that exist in different strips of paper [Elizalde et al., 2016]. Detailed information can be found in the supplementary information.

For the numerical prototyping, meshing processes were made with STAR-CCM+ ® software from Siemens Digital Industries Software, (Plano, TX, USA). The number of cells for all cases was kept approximately constant in the range of 250.000 with a mostly uniform spatial distribution. Numerical simulations were performed using OpenFOAM® v2112. The solvers selected within the OpenFOAM® environment were `porousMicroTransport` with a LETd model for unsaturated capillary flow [Gerlero et al., 2023, 2022] and `electroMicroTransport` solver for electrophoretic separations [Gerlero et al., 2021b]. All the simulated cases were run on an

AMD® Ryzen 5 3400G 3.70 GHz (1 CPU, 4 cores), 16 GB Micron 16 GB-DDR3-1600 MHz; using one core for serial simulations and four cores for parallel simulations.

C.3.5.1. Boundary conditions

The first two stages of the simulation consider the equations of capillary flow for the solvent and transport of the dissolved dye and buffer species [Horgue et al., 2022]. For the initial *injection stage*, a saturated boundary condition for the moisture content in the substrate is applied at the ends of the three liquid reservoirs (c.f. Fig. C.1) in order to model the capillary filling. The initial condition for this field corresponds to the air-dry moisture content [Gerlero et al., 2022], and no-flux conditions are applied on all other boundaries. The concentration fields for the buffer species are also configured with Dirichlet-type boundary conditions at the three reservoirs, with zero initial concentration in the device and no-flux conditions across the rest of the boundaries. The dye concentration field has a Dirichlet-type condition at the end of the dye/buffer reservoir, with no-flux boundary conditions elsewhere and zero initial concentration.

In the *focusing* stage, the boundary condition for moisture content at the dye/buffer inlet is changed to no-flux to model the exhaustion of the contents in such reservoir.

Finally, the *electrophoretic run* stage, requires a complete saturation of the device, meaning that the capillary flow equation is in a steady state and needs not be solved further. The solver used for this stage considers the electrophoretic transport of the dye species as well as electroosmotic flow. Boundary conditions for buffer and dye concentrations are set to no-flux everywhere. For the electric potential, Dirichlet boundary conditions at the wing inlets impose the prescribed potential difference.

C.4. Results and discussion

C.4.1. Numerically assisted prototype design

As mentioned earlier, the design of the device was numerically aided. The numerical prototypes and the results of the simulations determined the final design. As was also mentioned, the operational sequence can be analyzed in three stages: injection, focusing, and electrophoretic run stage.

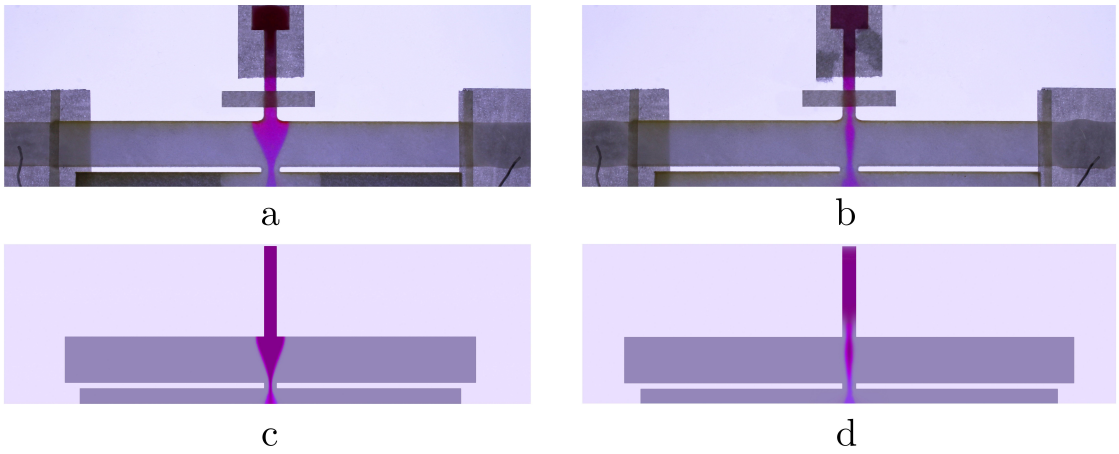

Figure C.2: Stages of validation of the proposed design. Experimental (A) vs numerical (C) results of the injection stage. In the focusing stage, we also compare the laboratory prototype (B) vs the simulated results (D).

Regarding the injection step, inlet and detection channel lengths determine the imbibition kinematics of the solutions. By setting a control point in the centre of the x-axis and y-axis of the detection zone, we can determine the time difference between the buffer/analyte inlet vs buffer reservoir to achieve the same arrival time for both components at the control point. Imbibition kinematics of uniform paper strips obeys the $l^2 = Dt$ relation and it is independent of the width of the strip. The standard uncertainty of D coefficient ($\sim$ 20%) [Elizalde et al., 2016] in Whatman #1 paper, can appreciably affect the arrival time at the control point. Nevertheless, the quasi-steady state of the dye configuration would not be affected by these uncertainties. The configuration of the experimental injection stage is shown in Fig. C.2A. It can be seen that, after reaching a quasi-steady condition, the dye distribution takes on a shape similar to a triangle that is well reproduced by the numerical simulation (Fig. C.2C).

After reaching this state, the focusing stage follows in order to shrink the triangular shape. The remaining analyte in the device, located mostly in the detection zone, will be redistributed according to the new streamlines given the geometry and configuration of sources and sink positions. The second capillary pump should be held long enough ($\sim$ $500s$) to ensure a symmetrical dye distribution. The amount of present dye can be controlled by the time that the new pump is operative. The final experimental configuration before starting the electrophoretic run stage is shown in Fig. C.2B).

The numerical solvers `porousMicroTransport` and `electroMicroTransport` need as input the porous media characteristic parameters, i.e. porosity ($\phi = 0.69$), constriction factor ($c_f = 2.6$), and dispersion factor [Urteaga et al., 2018]; for the transported substances, the electrophoretic mobility (μ_e) and the respective pKa for BGE components are required. Such values

can be found in `electrolytes` database that complements the `electroMicroTransport` toolbox. In the case of the dyes, such values were taken from literature for the initial simulations, and corrected afterwards with the experimental results obtained in the experiments presented here. In these cases, the effect of chromatography was included via a specific-dye retardation factor (R_f) that affects the electrophoretic mobility. In the case of simulation of Fig. C.2, values of μ_e and R_f used were those reported in Table C.1 for Tartrazine dye.

The differences between the experimental (Figs. C.2A and C.2B) and the numerical (Figs. C.2C and C.2D) prototypes can be explained due to the uncertainties presented by the porous medium regarding the macroscopic parameters that globally describe its microstructure. Despite this, it can be said that the shapes obtained at each stage are similar and consequently that the computer-aided design was very useful, considerably decreasing the development time and the number of experimental prototypes. The computational cost of the simulations was 45 minutes total for the injection and focusing stages and 600 and 100 seconds of simulated time respectively, in serial runs. In the electrophoretic stage, 565 minutes of running in parallel with 20 cores were needed to simulate 400 seconds.

C.4.2. Paper-based electrophoresis

Once the injection and focusing stages were completed, a voltage difference was applied between the ends of the reservoirs in the detection zone. Due to the device's symmetry, it is possible to analyze molecules that have both negative and positive surface charges. A total of five dyes were measured and analyzed using both the paper-based device presented and CE. Obtained values and the corresponding uncertainties of these measurements are reported in Table C.1. The reproducibility of the device was tested at least 5 times with the same dye (Tartrazine) at pH=5.5. The dispersion in the measurements was found to be less than 7%, which is consistent with typical reproducibility of e-μPADs [Schaumburg et al., 2018a]. The uncertainties reported in Table C.1 are the standard deviation of measured values for each dye (10% dispersion was assigned for dyes measured only once). In order to provide an example of these measurements and analyzing processes, the dynamic of a Tartrazine dye in paper-based electrophoresis is shown. Fig C.3A presents the image of the whole device during the electrophoretic run at 300 seconds. When processing such a picture, the red curve in Fig C.3B is obtained. In this picture, the blue curve is the initial state obtained when processing the picture at time $t = 0$, following the protocol reported in the supplementary material.

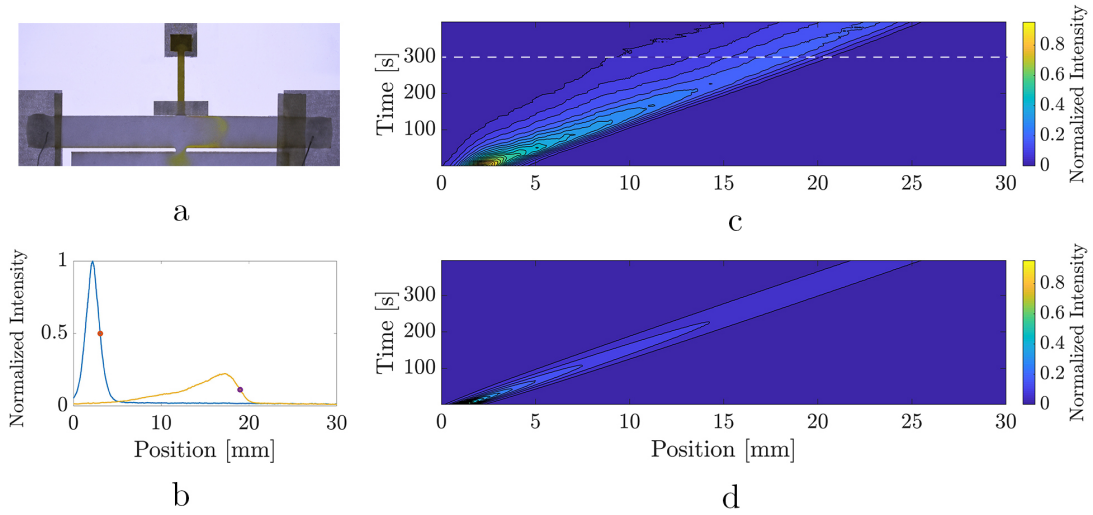

Figure C.3: Experimental and numerical results for the electrophoretic run of Tartrazine. a) Device operating at $t = 300$ s; b) Processed data curves for $t = 0$ s (blue) and $t = 300$ s (yellow). Marked points denote the spatial position, determined with the H-Cut method. c) 2D reconstruction of the processed information (position vs. time). The dashed line indicates the time when the image in a) was taken. d) Numerical counterpart of c).

The normalized concentration of the dye (colour scale) gives an indication of where it is located (horizontal axis) and time (vertical axis) as it is presented in Fig C.3C for the experimental run of Tartrazine, and its numerical counterpart shown in Fig C.3D. It is observed that the dispersion of the analyte in the experimental run is broader than the simulated one. This effect may be associated with the different effective mobilities obtained for the same molecule in the porous substrate. The dispersion can occur due to a variety of factors, including molecule affinity to paper fibres, electric and mechanical dispersion, and border effects. These factors may not have a significant impact on the open channel electrophoretic mobility either in capillaries or microfluidic chips. In order to give a description of this observed discrepancy, is necessary first to mention that the original numerical model includes all the aforementioned effects, with the only exception of the affinity of the molecules to fibres that results in a chromatographic process. In the next section, a quantitative analysis of the chromatographic behaviour of the dyes is presented.

C.4.2.1. Paper-based chromatography

In order to quantify the effect of the affinity of the dye molecules to the paper fibres, samples and buffers of the same concentrations as in the electrophoretic measurements were considered. Fig. C.4A shows 13 strips where dyes and control (buffer in strips 1 and 2) were measured (at least) in duplicate.

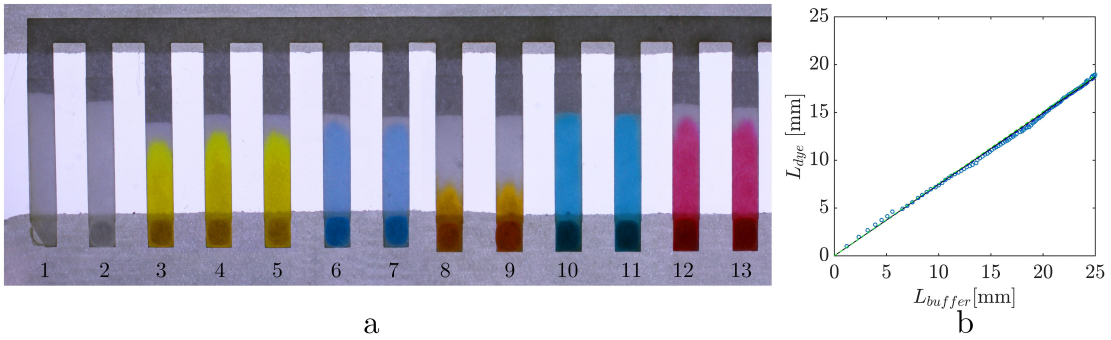

Figure C.4: Paper-based chromatography of multiple dyes a) Screenshot of the chromatography experiment for selected dyes at t=180 s and pH=5.5. 1-2 are control strips, filled with buffer. 3-5 Tartrazine, 6-7 Brillant Blue, 8-9 Methyl Orange, 10-11 Fast Green, and 12-13 Red Ponceau. b) Linear fit of Tartrazine and buffer front positions. The slope of this line is the retardation factor R_f.

Slightly irregular coloured patterns were observed for some colourants as the advance at the edges is slower than at the centre of the strip due to evaporation effects. The value of L_{dye} was taken at exactly half the width of the strip. Fig. C.4B presents the results of the measurement of R_f for Tartrazine, where it can be seen that the relationship between L_{buffer} and L_{dye} is completely linear in Whatman #1 substrates. Values of R_f were measured for the two different BGEs at pHs 5.5 and 9.0, finding some differences for the same dyes at different pHs. Such results are reported in Table C.1. A detailed description of the processing and analysis of the images can be found in the supplementary information.

C.4.3. Model validation

To evaluate the influence of the porous medium on the electrophoretic mobilities of the dyes, the paper and capillaries mobilities were compared in Fig. C.5. A least-squares linear fit was made for the values obtained for each dye at both pHs, following the linear relationship between μ_p^{eff} and μ_e presented in eq. (C.3). It is important to emphasize here that for the linear regression, a single free parameter (the slope of the intercept-free linear function) was considered, this parameter is $\frac{\phi}{c_f}$, as far as all the other terms of eq. (C.3) were measured in this work or taken from literature [Franck et al., 2021].

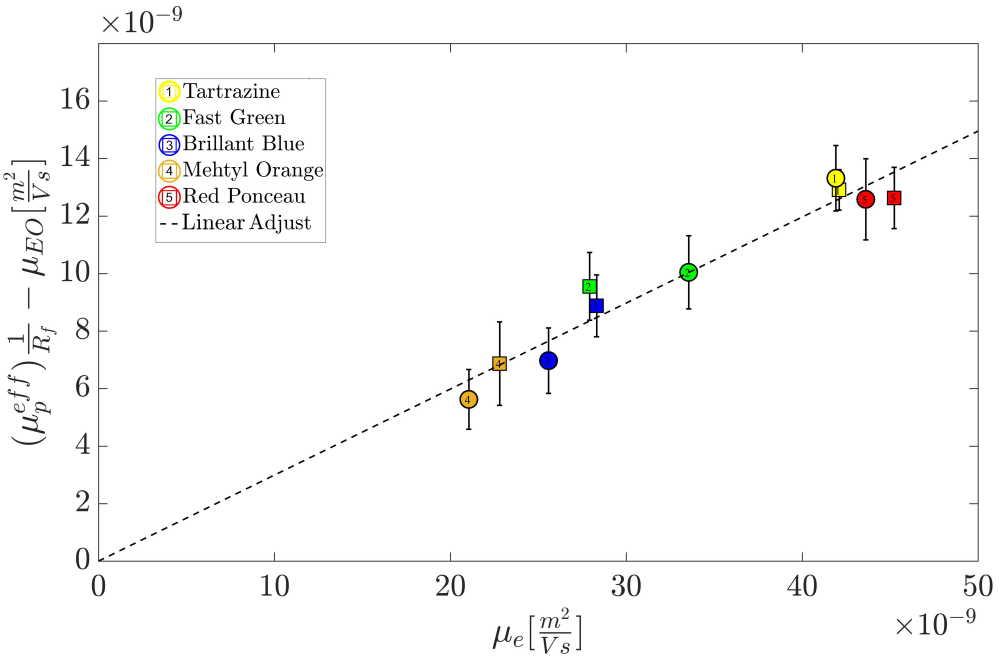

Figure C.5: Experimental validation of the electrophoretic mobilities model in porous substrates (eq. (C.3)). Open channel and paper mobilities were measured for different dyes at two pH values. Squares correspond to values measured at pH=5.5 and circles to pH=9.0. The dashed line is the least-squares linear fit to all the data with a single free parameter.

The results shown in Fig. C.5 clearly corroborate the hypothesis of the model correlation condensed in eq. (C.3), proposes that a linear relationship exists between the effective mobility measured in the paper (μ_p^{eff}) and the open channel mobility (μ_e) and such relationship depends only on the characteristics of the porous medium (i.e. $\frac{\phi}{c_f}$). A very important practical consequence of the validation of the model is that μ_p^{eff} can be obtained directly from μ_e, when ϕ and c_f are known for the substrate (for example as it is reported in [Franck et al., 2022]), and R_f is measured for the particular dye on such substrate. Another important comment is that the pk_a values are not affected by the porous media due to the fact that the porous microstructure and the ionic strength of the BGE enable full development of the electric double layer and the electroneutrality hypothesis remains valid, as it is the case of Whatman #1 paper [Novotnỳ and Gaš, 2021]. Consequently, the proposed correlation is valid if the BGE remains the same in both open-channel and porous media conditions.

Finally, it is important to mention that for the linear regression shown, the obtained value of c_f is 2.3 ± 0.1, which is similar to values previously obtained with independent experiments based on water imbibition, pressure-driven flow, and electrical conductivity [Franck et al., 2022].

Substance	$\mu_e\ 10^{-9}\frac{m^2}{Vs}$		$\mu_p^{eff}\ 10^{-9}\frac{m^2}{Vs}$		R_f	
	pH=5.5	pH=9.0	pH=5.5	pH=9.0	pH=5.5	pH=9.0
Tartrazine	42.1 ± 0.2	41.9 ± 0.3	9.2 ± 0.6	8.6 ± 0.9	0.75 ± 0.02	0.68 ± 0.03
Fast Green FCF	27.8 ± 0.1	33.5 ± 0.2	8.8 ± 1	9.4 ± 1	0.98 ± 0.03	1 ± 0.07
Brillant Blue	27.6 ± 0.1	25.6 ± 0.2	7.6 ± 0.8	5.7 ± 0.6	0.92 ± 0.02	0.93 ± 0.04
Methyl Orange	21.9 ± 0.1	21 ± 0.2	1.6 ± 0.2	1.7 ± 0.1	0.27 ± 0.02	0.35 ± 0.03
Red Ponceau	45.3 ± 0.2	43.6 ± 0.2	10 ± 1	11.4 ± 1.1	0.83 ± 0.03	0.97 ± 0.1

Table C.1: Electrophoretic mobilities, in open channel and paper substrates, and retention factor of different dyes at two pH values.

C.5. Conclusions

In this work, we performed a numerically-assisted design of a prototype for measuring the electrophoretic mobilities of anions and cations in paper-based substrates. The measurements made with this device enabled the validation of a proposed correlation between open-channel and porous media electrophoretic mobilities. To our knowledge, this is the first attempt for a systematic studio of this physicochemical property for its application on e-μPADs. The numerical tools selected were suitable for the selected task, offering an optimal platform for the optimization of the geometrical design as well as the operational parameters, including a novel two-step injection process that delivers a uniform and thin line of dye. The computational costs of the numerical prototypes were reasonable and compatible with the manufacturing and experimental stages. We are convinced that the combination of `porousMicroTransport` and `electroMicroTransport` can help the community develop more robust and efficient e-μPADs with shorter turnaround times.

The final design for the experimental setup showed to be robust in terms of offering good repeatability for the results enabling reliable measurements within reasonable experiment times. The measured values for electrophoretic mobility in the paper could be correlated with the open

channel values with a simple model, allowing developers to easily obtain paper mobilities. Despite the fact that the EOF in fused-silica capillaries is higher than in paper and relatively unstable at pH 5.5, reported results in electrophoretic mobilities were consistent for all the experiments.

Moreover, these measurements both in paper and in open channels, will contribute to decreasing the level of uncertainty due to the high dispersion of such values in the current literature. Having demonstrated the robustness of the device, other alternative detection methods can be used for the determination of non-stained components. The design method, the experimental setup, the validation of the correlation, and also the values obtained for the electrophoretic mobilities will undoubtedly contribute in the near future to the development of instrument-free e-μPADs for health care or environmental applications.

Acknowledgments

This work was supported by CONICET [grant number PIP-2020-1049], Agencia I+D+i [grant number PICT-2018-02920], UNL [grant number CAI+D 2020] and UTN [grant numbers PID8132, PID8685], Argentina. We thank Dr. Ignacio Niizawa for his advice and provision of dye samples, and Dr. Federico Schaumburg for his assistance with laser cutting.

Conflicts of interest

The authors declare no financial/commercial or academic conflict of interest.

Data availability

The datasets generated during and/or analysed during the current study are available from the corresponding author upon reasonable request.

Supporting information

Supporting information providing technical details about the image processing steps and software, as well as the protocols and results for the measurements of retention coefficients can be found in the on-line version of the article.

References

I. Ali, O. M. L. Alharbi, and M. M. Sanagi. Nano-capillary electrophoresis for environmental analysis. *Environ Chem Lett*, 14:79–98, 2015. doi: 10.1007/s10311-015-0547-x.

G. Álvarez, L. Montero, L. Llorens, M. Castro-Puyana, and A. Cifuentes. Recent advances in the application of capillary electromigration methods for food analysis and foodomics. *Electrophoresis*, 39:136–159, 2017. doi: 10.1002/elps.201700321.

D. A. Bikos and T. G. Mason. Band-collision gel electrophoresis. *Nat Commun*, 10, 2019. doi: 10.1038/s41467-019-11438-9.

F. A. Casado-Carmona, M. del Carmen Alcudia-León, R. Lucena, and S. Cárdenas. Portable stir membrane device for on-site environmental sampling and extraction. *J Chromatogr A*, 1606: 360359, 2019.

S. M. Damián, F. Schaumburg, and P. A. Kler. Open-source toolbox for electromigrative separations. *Comput Phys Commun*, 237:244–252, 2019.

J. M. de los Santos-Ramirez, P. G. Boyas-Chavez, A. Cerrillos-Ordoñez, M. Mata-Gomez, R. C. Gallo-Villanueva, and V. H. Perez-Gonzalez. Trends and challenges in microfluidic methods for protein manipulation—a review. *Electrophoresis*, 2023.

M. Dovhunová, M. Malỳ, P. Dubskỳ, G. S. Gerlero, and P. A. Kler. Generalized model of the linear theory of electromigration and its application to electrokinetic chromatography: Capillary zone electrophoretic systems with complex-forming equilibria. *J Chromatogr A*, 1610:460595, 2020.

E. Elizalde, R. Urteaga, and C. L. A. Berli. Rational design of capillary-driven flows for paper-based microfluidics. *Lab Chip*, 15:2173–2180, 2015. doi: 10.1039/C4LC01487A.

E. Elizalde, R. Urteaga, and C. L. A. Berli. Precise capillary flow for paper-based viscometry. *Microfluid Nanofluid*, 20:135, 2016. doi: 10.1007/s10404-016-1800-8.

N. Franck, F. Schaumburg, P. A. Kler, and R. Urteaga. Precise electroosmotic flow measurements on paper substrates. *Electrophoresis*, 42:975–982, 2021. doi: 10.1002/elps.202000271.

N. Franck, C. L. Berli, P. A. Kler, and R. Urteaga. Multiphysics approach for fluid and charge transport in paper-based microfluidics. *Microfluid Nanofluid*, 26:87, 2022.

G. S. Gerlero, S. M. Damián, and P. A. Kler. electromicrotransport v2107: Open-source toolbox for paper-based electromigrative separations. *Comput Phys Commun*, 269:108143, 2021a.

G. S. Gerlero, S. M. Damián, F. Schaumburg, N. Franck, and P. A. Kler. Numerical simulations of paper-based electrophoretic separations with open-source tools. *Electrophoresis*, 42:1543–1551, 2021b.

G. S. Gerlero, A. R. Valdez, R. Urteaga, and P. A. Kler. Validity of capillary imbibition models in paper-based microfluidic applications. *Transport Porous Med*, 141:359–378, 2022. doi: 10.1007/s11242-021-01724-w.

G. S. Gerlero, C. L. A. Berli, and P. A. Kler. Open-source high-performance software packages for direct and inverse solving of horizontal capillary flow. *Capillarity*, 6:31–40, 2023.

GNU Octave Online. 2022. Accessed: 2022-08-01.

A. M. Haines, S. S. Tobe, H. J. Kobus, and A. Linacre. Properties of nucleic acid staining dyes used in gel electrophoresis. *Electrophoresis*, 36:941–944, 2015. doi: 10.1002/elps.201400496.

S. Hennig, Z. Shu, L. Gutzweiler, P. Koltay, F. Stetten, R. Zengerle, and S. M. Früh. Paper-based open microfluidic platform for protein electrophoresis and immunoprobing. *Electrophoresis*, 43: 621–631, 2021. doi: 10.1002/elps.202100327.

T. Hirokawa, M. Nishino, N. Aoki, Y. Kiso, Y. Sawamoto, T. Yagi, and J.-I. Akiyama. Table of isotachophoretic indices: I. simulated qualitative and quantitative indices of 287 anionic substances in the range ph 3–10. *J Chromatogr A*, 271:1–106, 1983.

P. Horgue, F. Renard, G. S. Gerlero, R. Guibert, and G. Debenest. porousmultiphasefoam v2107: An open-source tool for modeling saturated/unsaturated water flows and solute transfers at watershed scale. *Comput Phys Commun*, 273:108278, 2022.

A. V. Jager, F. G. Tonin, and M. F. M. Tavares. Optimizing the separation of food dyes by capillary electrophoresis. *J Sep Sci*, 28:957–965, 2005. doi: 10.1002/jssc.200500039.

S. Jaitpal, P. Naik, S. Chakraborty, S. Banerjee, and D. Paul. Exploring the concentration-dependent transport and the loss of rhodamine b, tartrazine, methylene blue, and amaranth dyes in common paperfluidic substrates. *Res Surf Inter*, 6:100034, 2022. doi: 10.1016/j.rsurfi.2021.100034.

T. K. Khurana and J. G. Santiago. Preconcentration, separation, and indirect detection of nonfluorescent analytes using fluorescent mobility markers. *Anal Chem*, 80:279–286, 2008.

C.-T. Kung, C.-Y. Hou, Y.-N. Wang, and L.-M. Fu. Microfluidic paper-based analytical devices for environmental analysis of soil, air, ecology and river water. *Sensor Actuat B-Chem*, 301: 126855, 2019.

K.-S. Lee, M. J. A. Shiddiky, S.-H. Park, D.-S. Park, and Y.-B. Shim. Electrophoretic analysis of food dyes using a miniaturized microfluidic system. *Electrophoresis*, 29:1910–1917, 2008. doi: 10.1002/elps.200700556.

V.-T. Nguyen, S. Song, S. Park, and C. Joo. Recent advances in high-sensitivity detection methods for paper-based lateral-flow assay. *Biosens Bioelectron*, 152:112015, 2020.

T. Novotnỳ and B. Gaš. Mathematical model of electromigration allowing the deviation from electroneutrality. *Electrophoresis*, 42:881–889, 2021.

T. Rosenfeld and M. Bercovici. Amplification-free detection of dna in a paper-based microfluidic device using electroosmotically balanced isotachophoresis. *Lab Chip*, 18:861–868, 2018.

F. Schaumburg, P. A. Kler, and C. L. A. Berli. Numerical prototyping of lateral flow biosensors. *Sens Actuat B-Chem*, 259:1099–1107, 2018a.

F. Schaumburg, R. Urteaga, P. A. Kler, and C. L. A. Berli. Design keys for paper-based concentration gradient generators. *J Chromatogr A*, 1561:83–91, 2018b.

F. Schaumburg, P. A. Kler, C. S. Carrell, C. L. Berli, and C. S. Henry. USB powered microfluidic paper-based analytical devices. *Electrophoresis*, 41(7-8):562–569, 2020. doi: 10.1002/elps.201900273.

F. Schaumburg, J. P. Vidocevich, G. S. Gerlero, N. Pujato, J. Macagno, P. A. Kler, and C. L. A. Berli. A free customizable tool for easy integration of microfluidics and smartphones. *Sci Rep-UK*, 12:8969, 2022.

A. Sena-Torralba, R. Alvarez-Diduk, C. Parolo, H. Torné-Morató, A. Müller, and A. Merkoçi. Paper-based electrophoretic bioassay: Biosensing in whole blood operating via smartphone. *Anal Chem*, 93:3112–3121, 2021. doi: 10.1021/acs.analchem.0c04330.

R. Urteaga, E. Elizalde, and C. L. A. Berli. Transverse solute dispersion in microfluidic paper-based analytical devices (μPADs). *Analyst*, 143:2259–2266, 2018. doi: 10.1039/c8an00149a.

Z.-Y. Wu, F. Zhang, Z. Kuang, F. Fang, and Y.-Y. Song. Fast and sensitive colorimetric detection of pigments from beverages by gradient zone electrophoresis on a paper based analytical device. *Microchem J*, 179:107499, 2022.

L. Zhu, M. Wu, R. Li, Y. Zhao, Y. Lu, T. Wang, L. Du, and L. Wan. Research progress on pesticide residue detection based on microfluidic technology. *Electrophoresis*, 44:1377–1404, 2023.

A. A. Zukas and A. P. Breksa III. Extraction methods for analysis of citrus leaf proteins by two-dimensional gel electrophoresis. *J Chromatogr A*, 1078:201–205, 2005.

Anexo D

Paper-based isotachophoretic preconcentration technique for low-cost determination of glyphosate

El artículo presentado a continuación ha sido publicado en la revista **Analytical and Bioanalytical Chemistry**.

N. Franck, P. Stopper, L. Ude, R. Urteaga, P. A. Kler, C. Huhn. Paper-based isotachophoretic preconcentration technique for low-cost determination of glyphosate. *Analytical and Bioanalytical Chemistry*, 416(29), 6745–6757, 2024. https://doi.org/10.1007/s00216-024-05544-x.

Paper-based isotachophoretic preconcentration technique for low-cost determination of glyphosate

Nicolás Franck[1,2], Pascal Stopper[4], Lukas Ude[4], Raul Urteaga[2], Pablo A. Kler[1,3], Carolin Huhn[4]

[1] CIMEC (Universidad Nacional del Litoral–CONICET), Colectora RN 168 Km 472, S3000GLN Santa Fe, Argentina

[2] Instituto de Física del Litoral (IFIS Litoral, UNL–CONICET), Güemes 3450, S3000GLN Santa Fe, Argentina

[3] Departamento de Ingeniería en Sistemas de Información, Facultad Regional Santa Fe, Universidad Tecnológica Nacional, Lavaisse 610, Santa Fe, Argentina

[4] Chemistry Department, Eberhard Karls Universität, Auf der Morgenstelle 18, 72076 Tübingen, Germany

Abstract

Electrophoretic microfluidic paper-based analytical devices (e-μPADs) are promising for low-cost and portable technologies, but quantitative detection remains challenging. In this study, we develop a paper-based isotachophoretic preconcentration and separation method for the herbicide glyphosate as a model analyte. The device, consisting of two electrode chambers filled with leading and terminating electrolytes and a nitrocellulose strip as the separation carrier, was illuminated by a flat light source and operated with a voltage supply of 400 V. Detection was accomplished using a simple camera. Colorimetric detection was optimized through competitive complexation between glyphosate, copper ions, and pyrocatechol violet as a dye. The buffer system was optimized using simulations, (i) ensuring the pH was optimal for the demetallation of the blue pyrocatechol violet-copper complex [PV] to the yellow free dye and (ii) ensuring the electrophoretic migration of

glyphosate into the slower [PV] for the colorimetric reaction. A new data evaluation method is presented, analyzing the RGB channel intensities. The linear range was between 0.8 and 25 µM, with a LOD of approximately 0.8 µM. The ITP separation preconcentrated glyphosate by a factor of 820 in numerical simulations. The method may be applied to control glyphosate formulations, especially in developing countries where herbicide sales and applications are poorly regulated.

Keywords: Glyphosate, e-µPAD, Paper-based devices, Point-of-need devices, Isotachophoresis.

D.1. Introduction

Glyphosate (GLY) is the world's most heavily applied herbicide. Usage worldwide has increased by a factor of 260 since its introduction in the agricultural market in 1974 [Benbrook, 2016]. GLY is widely used in agriculture, forestry, and urban applications [Huhn, 2018]. Its overuse and abuse are discussed to evoke environmental problems [Bruggen et al., 2018]. Mobilization into surface water may pose a threat to ecosystems [Gill et al., 2017], however, not all countries monitor GLY systematically [Oltramare et al., 2022]. For monitoring, liquid chromatography (LC) coupled to mass spectrometry (MS) after derivatization of GLY with 9-fluorenyl methyl carbonyl chloride (FMOC) is frequently used for quantification, making its analysis costly and time-consuming [Okada et al., 2018]. Alternative methods have been published based on spectroscopic methods, electrochemical sensors, or capillary electrophoresis [Valle et al., 2018]. Other analytical methods with lower demand for instrumentation have also been published, the most relevant ones are colorimetric methods. These methods reached limits of detection compatible with environmental monitoring e.g., by using a fluorescent probe and competitive complexation with copper, requiring only a UV lamp as equipment [Wei et al., 2023]. Furthermore, a colorimetric method with naked-eye detection was recently reported, where the complexation of Cu^{2+} with pyrocatechol violet (PV) leads to a blue complex. In contrast, GLY, has a higher complex formation constant to Cu^{2+} than PV, thus upon competitive complexation, GLY induces a shift in absorption wavelength upon forming the yellow uncomplexed PV. A limit of detection of 20 µM GLY in tap water by naked eye was demonstrated, and quantification by smartphone analysis with a limit of detection as low as 2.66 µM [Yadav and Zelder, 2021] was reported. Two main constraints are related to these approaches: first, surface waters have concentrations often below 6 nM [Ulrich and Ferguson, 2021, Schwientek et al., 2024]. Second, matrix effects, i.e. the presence of other complexing agents such as EDTA, which interfere by complexing copper with a higher complex formation constant than PV, will impair GLY analysis. To improve the limits of detection of these

colorimetric techniques, sample preconcentration, and matrix removal have to be implemented before the colorimetric detection of GLY. In this study, we examine the applicability of paper-based isotachophoresis for both tasks: sample preconcentration and electrophoretic removal of matrix compounds.

Paper-based colorimetric assays have been applied for more than one hundred years, but more recently, microfluidic paper-based analytical devices have developed rapidly because of their advantages, such as small sample volume, rapid detection rates, low cost, and portability. They can be coupled with various detection methods including colorimetric, electrochemical [Ferreira et al., 2021], or optical detection, with simple detectors such as scanners, cameras in mobile phones, or more specialized devices [Zheng et al., 2021]. The images taken can be analyzed using computer programs, and, depending on the color and hue of the image, the total value or just one channel of the color space can be used for quantification [Nery and Kubota, 2013].

Most paper-based methods rely on capillary imbibition or diffusion phenomena to bring the sample into contact with the reactants of the specific colorimetric detection. However, these transport modes do not separate the analyte of interest from disturbing matrix compounds. This can be achieved using principles of active mobilization by using electric fields for charged compounds such as GLY.

Particularly, electrophoretic microfluidic paper-based analytical devices (e-µPADs) became attractive in recent years for analytical applications [Salentijn et al., 2018], often with the integration of smartphones and mobile devices for detection [Schaumburg et al., 2020b, 2022]. For example, different types of human and bovine serum proteins were preconcentrated and separated quickly and with good resolution [Niu et al., 2018]. Biomarkers such as lipids, small molecules, carbohydrates, nucleic acids, and cells [Pagaduan et al., 2015] were analyzed using e-µPADs. e-µPADs have also been studied to improve the limit of detection (LOD) of lateral flow immunoassays in diagnostic devices. High preconcentration factors of up to 900 were achieved by using isotachophoresis (ITP) [Moghadam et al., 2014], an electrophoretic method based on electrolyte systems with concentration gradients or discontinuous concentrations profiles. ITP was successfully integrated into microfluidics and paper-based chemical and biochemical assays [Ramachandran and Santiago, 2022]. ITP can concentrate trace amounts of substances into a narrow boundary region which improves limits of detection as shown in various applications [Malá and Gebauer, 2018]. Also, ITP is versatile in analyzing virtually any ionogenic analyte, making it broadly applicable in many analytical applications, especially in biomedical and environmental analyses [Malá and Gebauer, 2023].

This work aims to develop a simple, low-cost paper-based isotachophoretic device for GLY

detection. Additionally, we seek to address current limitations in sensitivity for environmental monitoring and explore potential applications in developing countries where herbicide regulation is lacking.

D.2. Materials and Methods

D.2.1. Chemicals

Glyphosate standard (analytical grade, 98.1%) was purchased from Merck, Darmstadt, DE. The pyrocatechol violet dye was bought from Carl Roth, Karlsruhe, DE and copper(II) chloride dihydrate was delivered by Sigma Aldrich, Steinheim, DE. 2-(*N*-morpholino)ethanesulfonic acid (MES, anhydrous, high purity grade) was purchased from Amresco (Darmstadt, Germany). HEPES (Lobov Cientifica, Buenos Aires, AR) was used to prepare background electrolytes (BGE) and terminating electrolytes (TE). HCl (Laboratorios Cicarelli, San Lorenzo, AR) was used as the leading electrolyte (LE); ε-aminocaproic acid, and TRIS (Merck, Darmstadt, DE) were used as counter-ions (CI). Polyvinylpyrrolidone (MW 1.000.000) was purchased from Polysciences, Warrington, USA. All solutions were prepared with ultrapure water from an inverse osmosis purifier (Osmoion, Apema SRL, Villa Dominico, AR). The pH of solutions was set by modeling the concentrations using pK_a-values and the pH was confirmed with a pH meter (Adwa A12, Szeged, HU). The chemicals used for the BGE in CE-MS analysis were aqueous ammonia solution (LC-MS grade, 25%) and formic acid (FA) for LC-MS (98%). As well as aqueous HCl (32%) for preconditioning were purchased from Thermo Fisher Scientific (Schwerte, Germany). Isopropanol (LC-MS grade), and phosphonic acid (H_3PO_3) (99%) were purchased from Merck, Darmstadt, DE. All chemicals were used without further purification. The water (H_2O) used as solvent was deionized and purified by an ELGA LabWater water purification system (Celle, Germany).

D.2.2. Optimization of the colorimetric detection

The spectral analyses were carried out using a Lambda 19 UV/Vis spectrometer (PerkinElmer, Waltham, MA, USA) with LambdaSPX software (Version 1.7, ascanis OHG, Überlingen, Germany) and with UV transparent semi-micro cuvettes, width: 10 mm (UV-Polymer, Brand, Wertheim, Germany). Cu(II)-GLY ([GLP]) stability constants were found to be 11.8 [Daniele, 1997] and 11.9 [Madsen et al., 1978, Popov et al., 2001]. For the copper-PV complexes ([PV]), no stability constant was found in the literature. Still, results by Yadav and Zelder indicate a similar stability constant as for [ZnZCN] at pH 7.4 based on its sensitivity for GLY [Yadav and Zelder,

2021], with a reported stability constant at pH 7.4 of 5.7 [Kocyła et al., 2017]. It is important to note, that the stability constants of the complexes depend on pH, temperature, ionic strength of the solution, and concentration of the metal ions and ligands, so these log(β) values do not always match the conditions of the assay but can be used as an estimate of a cut-off value for competitive complexation.

D.2.2.1. Testing porous substrates

Different substrates for e-µPADs were investigated: three solid supports were used in the experiments: cellulose filter paper MN615 (Macherey-Nagel, Düren, DE), Nitrocellulose Hi-Flow HFC13504 (Merck, Darmstadt, DE) and ALUGRAM RP-18W/UV_{254} (Macherey-Nagel, Düren, DE). To investigate the applicability of different porous substrates for electrophoretic experiments with colorimetric detection, sheets of 5 mm x 5 mm in size were cut from the solid supports. Aqueous solutions of [PV] at a concentration of 75 µM were prepared by mixing the pyrocatechol violet dye and copper chloride at a stoichiometric ratio of 1:2 in solutions of MES (10 mM) adjusted to pH 6.5 with KOH. Aqueous GLY solutions with a concentration range of 0-500 µM were tested. Six sheets were prepared for each substrate.
After some optimization steps, the test procedure added 20 µL of the GLY samples with five different concentrations to five sheets. The sixth sheet was used as blank. The papers were allowed to dry at ambient temperature. Then, 10 µL of the colored complex were added. Photographs were taken at each stage.

D.2.3. CE-MS analysis

ITP-UV analysis was conducted with an A 7100 CE instrument from Agilent Technologies (Waldbronn, Germany). The separations were performed in a bare fused silica capillary with 50 µm inner diameter and 75 cm in length. Before the first use, capillaries were conditioned by flushing the surface with 0.05 M aqueous NaOH and H_2O for 180 s, each at 1 bar. Before ITP measurements, the capillary was dynamically coated by flushing the surface with 90 mM aqueous polyvinylpyrrolidone (PVP) solution for 600 s at 1 bar. Separations were conducted with an internal pressure support of 40 mbar and a voltage of -10 kV. For detection, the built-in diode array detector was used at a wavelength of 596 nm for the [PV] complex and 444 nm for free PV.

CE-MS analyses were conducted with a 7100 CE coupled to a 6150 single quadrupole mass spectrometer from Agilent Technologies (Waldbronn, Germany) via a coaxial sheath liquid electrospray interface equipped with a platinum needle. The sheath liquid consisted of a mix of 50% H_2O and 50% isopropanol with 0.1% formic acid added. The sheath liquid was supplied via a

splitter by a 1200 series isocratic pump from Agilent Technologies (Waldbronn, Germany) at a flow rate of $5\,\mu L/min$. The drying gas temperature was $150\,°C$, with a gas flow of $11\,L/min$ and a nebulizer pressure of 3 psi. The MS was operated in selected ion monitoring mode, with $100\,V$ fragmentor voltage and a capillary voltage of $4000\,V$. Molecular ions monitored were $[M\text{-}H]^-$. The separations were performed in a bare fused silica capillary with $50\,\mu m$ inner diameter and $75\,cm$ in length. Before the first use, capillaries were conditioned by flushing the surface with $0.05\,M$ aqueous NaOH and H_2O for $180\,sec$ each at 1 bar. The separations were conducted at an internal pressure support of $50\,mbar$ and a voltage of $-15\,kV$ increasing over two minutes to $-30\,kV$ after injection. The injection was conducted via hydrodynamic injection at $50\,mbar$ for $10\,s$, followed by an injection of background electrolyte at $100\,mbar$ for $10\,s$.

D.2.4. Computational Tools

Numerical simulations were performed using OpenFOAM v2212. Meshing processes were made with blockMesh integrated into the solver. The number of cells for all cases was kept approximately constant in the range of 15.000 with a uniform spatial distribution. The solvers selected within the OpenFOAM environment was the `electroMicroTransport` solver for electrophoretic separations [Gerlero et al., 2021a]. All the simulated cases were run on an AMD Ryzen 5 3400G 3.70 GHz (1 CPU, 4 cores), 16 GB Micron 16 GB-DDR3-1600 MHz. A Whatman #1 model was used for the simulations. `electroMicroTransport` used two parameters: the porosity, measured by weighting dry and wet substrates with known geometries; and the tortuosity (τ), related to the constriction factor C by $C = \tau^2$. This factor was calculated using the experimental setup of the electrical model [Franck et al., 2022]. The simulation geometry was a rectangular paper strip, originally of $80\,mm$ length and $10\,mm$ width, but with an effective electric field application distance of $65\,mm$. Electrolyte electrophoretic mobilities were taken from PeakMaster, except GLY taken from previous CE measurements [Graf et al., 2022]. Initial conditions included the TE + GLY located $18\,mm$ from the TE reservoir, with the remainder filled with LE. The solver considers the reagent species' electrophoretic transport and a null electroosmotic flow (EOF). Boundary conditions for LE and TE were set to no flux anywhere. Dirichlet boundary conditions at the reservoirs imposed a prescribed potential difference for the electric potential.

D.2.5. Paper-based electrophoresis

A new low-cost device for e-µPAD was developed and schematically shown in Fig. D.1a. It consists of a 3D-printed housing with a separation chamber with anode and cathode reservoirs, each equipped with platinum electrodes. A nitrocellulose strip of $80\,mm$ length and $10\,mm$ width

were cut with a paper cutter and placed on a glass support bridging the two reservoirs with its ends being immersed in the buffers. A flat backlight lamp (Rollei Lumis Key Light LED streaming light, Rollei, DE) was used for illumination.

D.2.5.1. Paper-based capillary electrophoresis

Based on our results for the colorimetric analysis reaction detection, we developed a paper-based capillary electrophoresis (pCE), using MES as a BGE adjusted to pH 6.5 with KOH. For the colorimetric complex solution, 175 µM of PV were mixed with 2 equivalents of $CuCl_2$ salt in the BGE buffer solution. GLY solutions at different concentrations (100, 150, 400, and 1200 μM) were prepared in the background electrolyte. In all electrolyte solutions, 3% m/v of PVP were added to suppress the EOF.

D.2.5.2. Paper-based ITP

Isotachophoresis experiments used 2.5 mM aqueous HEPES solution as TE with 5 mM ε-aminocaproic acid as counter-ion, 26 mM aqueous HCl solution was used as the LE with a mixture of ε-aminocaproic acid and TRIS (26 mM each) used as a CI. All electrolytes were chosen and optimized to ensure a pH value of 6.5 optimal for the colorimetric detection, using PeakMaster [Gaš, 2023] and numerical simulations, as described in Section D.2.4. In the protocol for ITP experiments, hydrophobic double-sided adhesive tape was placed at the ends of the glass slide to fix the nitrocellulose strips and keep an air gap between the glass avoiding edge effects that could alter imbibition flow [Schaumburg and Berli, 2019]. The anode reservoir was initially filled with a solution of the [PV] colorimetric complex at a constant concentration of 175 µM in the LE. After 150 s, the cathode reservoir was filled with GLY solutions dissolved in the TE. During the imbibition process, GLY and the [PV] complex moved towards each other through diffusional transport, eventually achieving the configuration displayed in Fig. D.1b.

Once the nitrocellulose sheet is completely wetted, ions start electrophoretic migration upon application of the electric field. This configuration leads to a semi-infinite sample loading of GLY and thus a continuous sample focusing by ITP (i.e. the amount of sample focused in an ITP stack increases with time) [Ramachandran and Santiago, 2022]. The color change occurs when preconcentrated GLY is separated from the TE, and reaches the [PV] complex, which has a lower electrophoretic mobility (see Fig D.1c), as determined by CE-UV, see Section D.3.3. A 400 V electric potential is provided by a Picoammeter/Voltage Source (Keithley 6487, Cleveland, OH, USA), which also measures the applied current. Color changes are recorded on a high-resolution digital camera (Canon EOS 1000D), placed vertically at a distance of 30 cm, connected to a PC,

and set to burst mode.

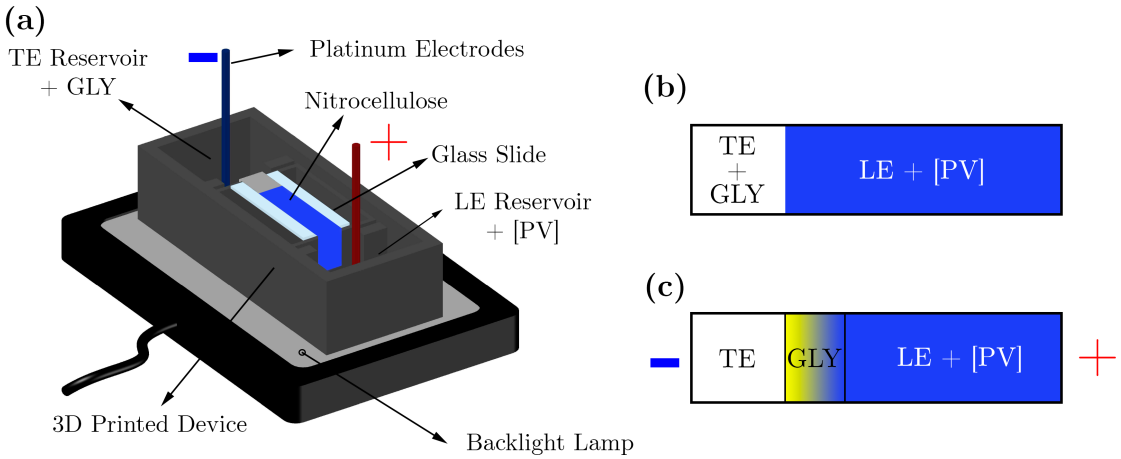

Figure D.1: **(a)** Schematic of the low-cost e-µPAD device, featuring a 3D-printed housing with platinum electrodes and nitrocellulose strips bridging the anode and cathode reservoirs. **(b)** Configuration after filling reservoirs and before starting electrophoretic migration. **(c)** Glyphosate preconcentration and color change upon applying an electric field for some minutes.

The spatial resolution was 36 µm and the time resolution was 12 frames per minute. Images obtained from experiments are analyzed with an ad-hoc algorithm developed in the MATLAB software framework.

D.3. Results and discussion

D.3.1. Optimization of the colorimetric detection

The colorimetric detection was based on the work of Yadav and Zelder [Yadav and Zelder, 2021]. Pyrocatechol violet forms complexes with copper. Upon the addition of GLY, which has a higher complex formation constant with Cu^{2+} than PV, the [PV] complex dissociated and changed color from blue to yellow, indicating the formation of free PV. Yadav and Zelder already tested many analytical parameters of the reaction of GLY with the [PV] complex. In the final protocol, the authors used a pH of 6.5 in HEPES buffer to be suitable for GLY detection. However, as HEPES with a pK_a of 7.41 at 20 °C [Sokołowska and Bal, 2005] is not well suited as a buffer for pH 6.5, we preferred MES ($pK_a \simeq 6.15$ at 20 °C) [Ewing and Robson, 1991].

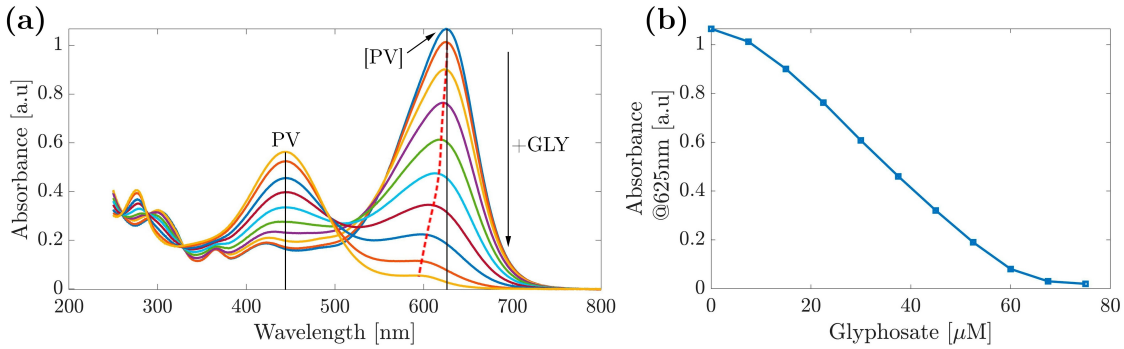

Figure D.2: Colorimetric GLY analysis in solution: **(a)** UV/Vis spectra of PV (30 µM) in the presence of two equivalents Cu^{2+} at pH 6.5 (aqueous MES buffer) with increasing concentration of GLY **(b)** absorbance at 625 nm in MES buffer at pH 6.5 depending on the GLY concentration.

To minimize risks of complex decomposition, we stored aqueous solutions of the reaction partners PV, $CuCl_2$, and MES separately at 4 °C. The [PV] complex in MES buffer (pH 6.5) was prepared directly before it was applied for GLY analysis upon mixing these solutions. Concentration series with increasing equivalents of GLY were conducted for the complexes in the MES buffer to obtain calibration curves, define the linear range, and calculate the LOD. As depicted in Fig. D.2a, the light blue color of [PV] (absorbance maximum at 625 nm) with a stoichiometry of PV:Cu^{2+} of 1:2 turns yellow upon the addition of GLY, as added GLY competes with [PV] for the Cu^{2+} ions.

Copper complexation by GLY thus releases free PV (absorbance maximum at 444 nm). When using 30 µM of the copper [PV] complex (2 equivalents Cu^{2+}), the calibration curve in Fig. D.2b reveals a linear range from 1-60 µM. The limit of detection was ∼1 µM using the lower end of the linear range for UV/Vis analyses and ∼15 µM for naked-eye detection.

D.3.1.1. Testing porous substrates

The transfer of the batch method for colorimetric detection faced three major challenges: sorption of reaction partners, especially GLY on the solid substrate, complex dissolution and strong diffusional broadening of spots. Therefore, three solid supports were chosen providing orthogonal surface chemistries. In regular filter paper, composed of hydrophilic cellulose (cellulose filter paper MN 615), [PV] complex solutions spread evenly (see Fig. D.3a), and the blue color remained, which indicated that the complex remained intact. However, when adding GLY solution at high concentrations, no visible color change from blue to yellow occurred, as observed in Fig. D.3a. We hypothesize, that despite the high stability constant of the [GLP] complex, a strong interaction of GLY with the cellulose substrate was present as can be expected from GLY's interaction with –OH and O^- groups, simulated in theoretical studies [de Aguiar Filho et al., 2021, Graf et al., 2022] and

well known from sorption to soil mineral oxides [Wimmer B. and C., 2022].

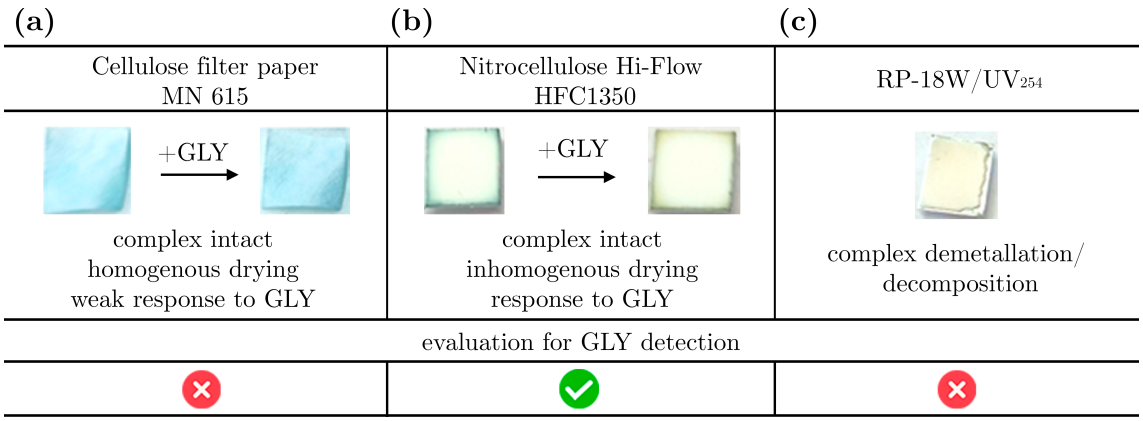

Figure D.3: Investigation of solid supports after applying solutions of [PV] complex and GLY. **(a)** Cellulose filter paper did not show a visible color change at high GLY concentrations. **(b)** Nitrocellulose shows a color change but suffers from the coffee ring effect. **(c)** The yellow color of RP-18 W TLC plates after the addition of [PV] indicates the decomposition of [PV] complexes.

Using nitrocellulose, we expected GLY adsorption onto the solid support to be reduced by electrostatic repulsion. Looking at the photographs in Fig D.3b, [PV] complexes stayed intact on the nitrocellulose substrate and a color change from blue to yellow occurred when GLY was added. However, the interaction of copper complexes ([PV] and [GLP]) and free GLY with nitrocellulose was lowered to such an extent, that the components diffused to the edges of the sheets upon drying. This phenomenon, named the coffee ring effect, is due to the solvent evaporating faster in the middle of the strip, evoking a concentration gradient [Zheng et al., 2021]. Moreover, the EOF in nitrocellulose is considerably higher than the EOF in other paper substrates [Franck et al., 2021], which generates distortions in the electrical profile of electrophoretic separations. Consequently, PVP was added to buffer solutions to suppress such flow. For the "RP-18 W" TLC plates, the surface was well wetted with aqueous solutions of the complexes due to residual –OH groups of the SiO_2 particles, but decomposition or demetallation of [PV] complexes can be deduced from the loss of the blue colors upon drying the [PV] solution and the formation of the free yellow PV colorant, as can be seen in Fig. D.3c. We proceeded with nitrocellulose as a solid support for paper-based electrophoresis and ITP.

D.3.2. Numerical electrolyte optimization for ITP

To identify the most suitable buffers for paper-based ITP experiments, we conducted numerical simulations using a system with three different counter-ions and three different terminating electrolytes. The primary factors considered were: i) optimal pH for the colorimetric reaction of

[GLP], ii) preconcentration factors reached for GLY in the ITP system, iii) electromigration behavior of GLY and [PV] to assure that competitive complexation takes place, and iv) influence of the buffer components on the stability of the [PV] complex.

Combination	TE [mM]	CI (LE) [mM]	LE pH	C/C_i (t=900s)
1	HEPES - 2.5	Creatinine - 60	5	635
2	HEPES - 2.5	Histidine - 60	6.2	700
3	HEPES - 2.5	TRIS/ε-aminocaproic acid - 26	6.5	820
4	Glycine - 2.5	TRIS/ε-aminocaproic acid - 26	6.5	725
5	MES - 2.5	TRIS/ε-aminocaproic acid - 26	6.5	365

Table D.1: Electrolyte combinations used in numerical simulations, displaying the concentrations, pH values, and preconcentration factors (C/C_i), calculated as the ratio between GLY concentration at 900 s (C) and the initial concentration (C_i).

Given the challenges involved in modelling nitrocellulose particularly due to the lack of data on its tortuosity and the effects of PVP on suppressing the EOF, we utilized a Whatman #1 paper model for the numerical experiments [Franck et al., 2023]. The TE and LE electrolyte concentrations were derived from the work of Moghadam et al., who explored the integration of ITP onto nitrocellulose-based paper microfluidic devices to enhance the detection limits of lateral flow immunoassays and reported 900 fold increase in initial sample concentration [Moghadam et al., 2014]. For all simulations, we used 26 mM HCl as LE and 5 mM ε-aminocaproic acid as the CI in TE. Glyphosate sample concentration was set to 1 µM, and pH calculations were done numerically [Damián et al., 2019].

Exemplarily, Fig. D.4a shows the results for GLY preconcentration after 900 seconds in an ITP using electrolytes of Combination 3: LE: HCl, TE: HEPES with the counterions TRIS and ε-aminocaproic acid. Glyphosate is well preconcentrated from 1 µM to ∼820 µM behind chloride as the LE into a sharp peak at a position of 30 mm. From this, we calculate a preconcentration factor of 820. Between 20 mm and 30 mm, the GLY concentration is ∼11 µM, not yet fully adapted. Using longer separation times, higher concentrations are reached. The dependence of the preconcentration factor on the simulation time is shown in Fig. D.4b for all buffer combinations tested. Similar slopes and thus similar preconcentration factors were observed for Combinations 1-4 with glycine and HEPES as TE. Electrolyte Combination 5 was inferior in preconcentration and the limited performance with MES as the TE is evident. However, further aspects have to be considered for GLY analysis: for instance, using creatinine as a CI did not meet the pH requirements of the colorimetric detection (pH range 6.5–7.4) with a pH of 5 in the LE solution. Additionally, when we experimentally tested histidine as CI and glycine as TE, a strong interaction with the [PV] was observed, resulting in a color change before the addition of GLY when the zone of the [PV] and

TE met (data not shown). Thus, further optimization was focused on electrolyte Combination 3. In environmental samples, we may expect other complexing agents such as oxalic acid or citric acid, which we know from colorimetric batch testing to disturb the glyphosate analysis. While compounds such as glycine and other ampholytes are not included in the ITP stack due to too low mobilities, oxalic and citric acid would disturb the analysis with the buffer system chosen. We thus conducted further simulations and found methylsulfonic acids as a suitable LE ion for samples with complexing agents as matrix constituents.

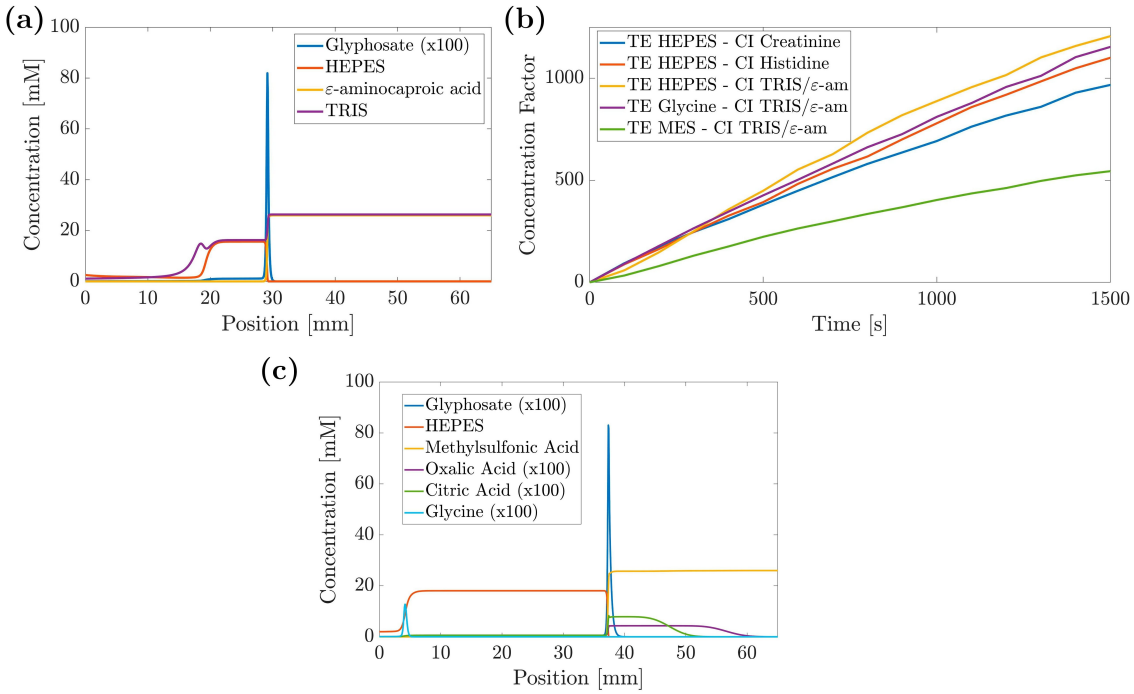

Figure D.4: Results of numerical simulations for optimizing electrolyte combinations in paper-based ITP. **(a)** Glyphosate sample and electrolyte arrangement (Combination 3 in Table D.1) at 900 s for counter-ions TRIS and ε-aminocaproic acid and TE HEPES. **(b)** Preconcentration factors for different combinations of counter-ions and terminating electrolytes (see Table D.1) depending on the time used for preconcentration. **(c)** Matrix effects with glycine, oxalic and citric acid. HCl in the LE was replaced by 26 mM methylsulfonic acid.

Figure D.4c shows the results of the simulation demonstrating that glycine is not included in the ITP stack and oxalic acid and citric acid are well separated from glyphosate. However, it is important to note that with methylsulfonic as LE, the theoretical preconcentration factor is slightly smaller than when using HCl. For this reason, we chose HCl as LE for the experimental work. The buffer system based on methylsulfonic acid can be implemented in the future for complex matrices without modifying the experimental setup.

D.3.3. Verification of the separation by ITP-UV analysis

To verify the relative migration of GLY, [PV] and the free PV the system established in the paper-based ITP was adapted to be reproduced in a classical capillary electrophoresis setup. For this, PVP in the electrolytes was substituted by a dynamic PVP coating [Kaneta et al., 2006] applied to the capillary surface before measurements. Additionally, the separation voltage was set to $-10\,\mathrm{kV}$ with a constant pressure support of 40 mbar for mobilization. To start the measurement the capillary was initially flushed with LE consisting of the buffer system with the [PV] complex. Subsequently, the TE was introduced by the pressure support, and a voltage was applied, leading to the formation of an ITP in the capillary.

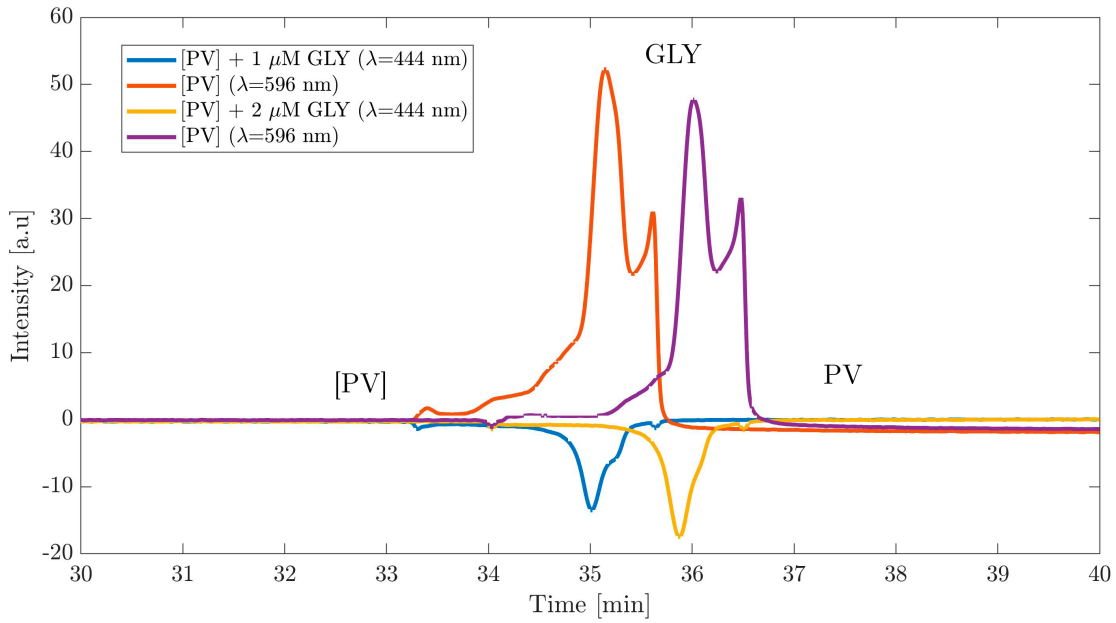

Figure D.5: ITP-UV measurement of [PV] (596 nm) and free PV (444 nm) in a commercial CE instrument. Measurements were conducted in a capillary with 50 µm inner diameter at a separation voltage of $-10\,\mathrm{kV}$ and 40 mbar with a LE consisting of 26 mM ε-aminocaproic acid, 26 mM HCl, 26.3 mM TRIS and 175 µM [PV]. The TE consisted of 2.5 mM HEPES, 5 mM ε-aminocaproic acid and 1 and 2 µM GLY.

The ITP-UV electropherograms displayed in Fig. D.5 show the successful reproduction of the ITP for 1 and 2 µM GLY in the TE when using ITP-UV analysis. GLY was detected indirectly by the UV absorption of free PV after dismantling the [PV] in the presence of GLY [Yadav and Zelder, 2021]. For detection, the absorption maximum of the complex 596 nm was chosen while the free PV was detected at 444 nm. A preconcentration of GLY from the TE can be seen in front of the ITP stack although GLY is constantly preconcentrated from the TE. The separation was susceptible to varying EOF due to the dynamic coating but no attempts were made for optimization. The steady decline of the baseline intensity is associated with the low stability of the complex in

the buffer medium. A reduction in the signal can be seen at both observed wavelengths in the electropherograms as impurities are also preconcentrated in the ITP stack before GLY.

D.3.4. Paper-based electrophoresis

D.3.4.1. Paper-based capillary electrophoresis

The experimental protocol consisted of first placing a nitrocellulose strip on the glass support bridging the two reservoirs. We added 20 µL of [PV] solution to the right of an imaginary line in the middle of the nitrocellulose strip. Then, further bands were added to the left: 10 µL BGE and 20 µL GLY (see scheme in Fig. D.6a). Afterwards, both cathode and anode reservoirs were filled with BGE solutions. Upon electric field application (1500 V m^{-1}), GLY will migrate to the cathode with a higher velocity than [PV], reaching the colorimetric complex band which evoked the formation of the yellow free dye and the glyphosate-copper complex (see Fig. D.6b).

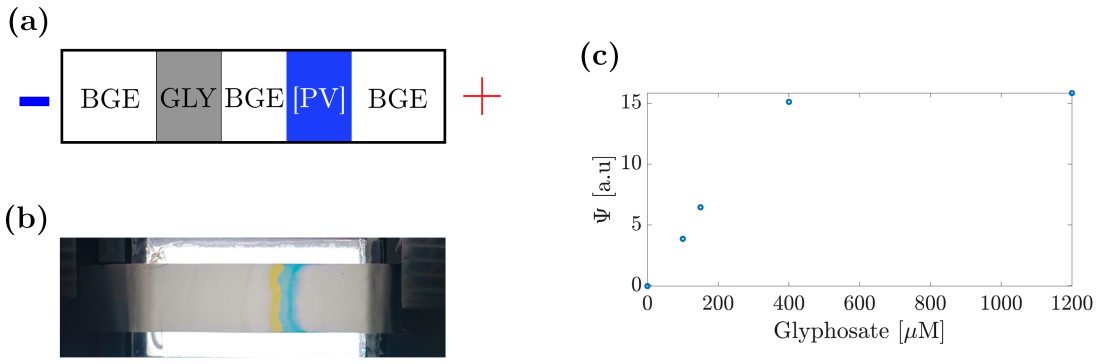

Figure D.6: Initial setup and results of paper-based capillary electrophoresis (pCE) using MES buffer (pH 6.5) and PV complex for GLY detection. **(a)** Configuration of the nitrocellulose strip with [PV], BGE, and GLY solutions before voltage application. **(b)** Experiment photograph at t=8 min upon electric field application, with GLY having reached the [PV] band **(c)** Absorbance changes indicating GLY concentration with a detection range from 100 µM to 400 µM.

The calibration curve (Fig. D.6c) showed a saturation starting at about 400 µM of GLY forming the upper end of the linear range. Differences to the 1200 µM sample are negligible, so the optimal detection range for pCE was 100 µM -400 µM of GLY when using a starting concentration of 175 µM of [PV]. Image analysis was identical to the ITP experiments, described in Section D.3.4.2. Lower GLY concentrations were tested, but already 50 µM was below the LOD. We estimated the LOD to be ∼100 µM, not suitable for environmental samples.

D.3.4.2. Paper-based ITP

Using the pCE technique, a high LOD of 100 µM for GLY was reached while the LOD of batch experiments was 2.66 µM for smartphone detection [Yadav and Zelder, 2021] and 1 µM with our high-end UV/VIS spectrometer. Thus, the pCE technique was replaced by paper-based ITP to enable preconcentration. For ITP experiments, we used four different GLY concentrations (1, 2, 5 and 25 µM) along with a plain buffer as a blank. Each experiment was repeated at least twice. Electrolyte Combination 3 (see Table D.1) was used as the electrolyte system. The nitrocellulose was prepared as described in Section D.2.5.2. To mitigate the EOF, 3% m/v of PVP were added to TE and LE solutions. We chose a rectangular area in the photograph to process the images taken during each experiment. Its size was set to the length of the nitrocellulose strip and one-third of its width (34 mm x 3.3 mm) as shown in Fig. D.7a at time 0 of an experiment with a GLY concentration of 5 µM. Figure D.7a shows the LE containing the blue [PV] complex before applying voltage. A sharp blue zone is visible on the left, where the TE with GLY added meets the [PV], due to the coffee ring effect during the capillary imbibition of the strip. The effective preconcentration of GLY by ITP was well visible in the second image of Fig. D.7a, after 15 min time of separation applying a voltage of 400 V. A video summary of this entire experimental run is linked in suplementary information. After 15 min upon applying the electric field, intense colors are visible in the center of the nitrocellulose strip. As indicated in Fig D.1c, different zones can be expected (discussing only the anions): i) a zone of GLY in TE, ii) a zone with a mixture of the [GLP] complex and free PV and iii) a zone of [PV] in the LE. Due to continuous separation and the mixing of blue and yellow compounds, different mixed colors evolve, making it difficult to achieve a direct naked-eye evaluation of the results.

For a complete analysis of the images, we constructed time-space matrices for all (RGB) channel intensities. For this, a vertical average of the images in the rectangular analysis area was calculated at each time point and all lines and stacked over time (Fig. D.7b). Thus, the length coordinate is represented on one axis, while time is represented on the other, as depicted in Fig D.7b. This method visualizes the system's dynamics of the entire experiment in a single image, showing the main colorimetric complexes involved.

The intensity of each channel (RGB) of the matrix can be written using the Beer-Lambert's law:

$$I^{RGB}(x,t) = I_0^{RGB}(x)e^{-(\alpha_0+\alpha_{[PV]})d} \tag{D.1}$$

where $I_0^{RGB}(x)$ represents the intensity of the backlight lamp. α_0 and $\alpha_{[PV]}$ are the porous substrate's and [PV]'s absorption coefficients, respectively, while d is the thickness of the porous layer. The absorption coefficient of the colorimetric complex can be linearly related to its respec-

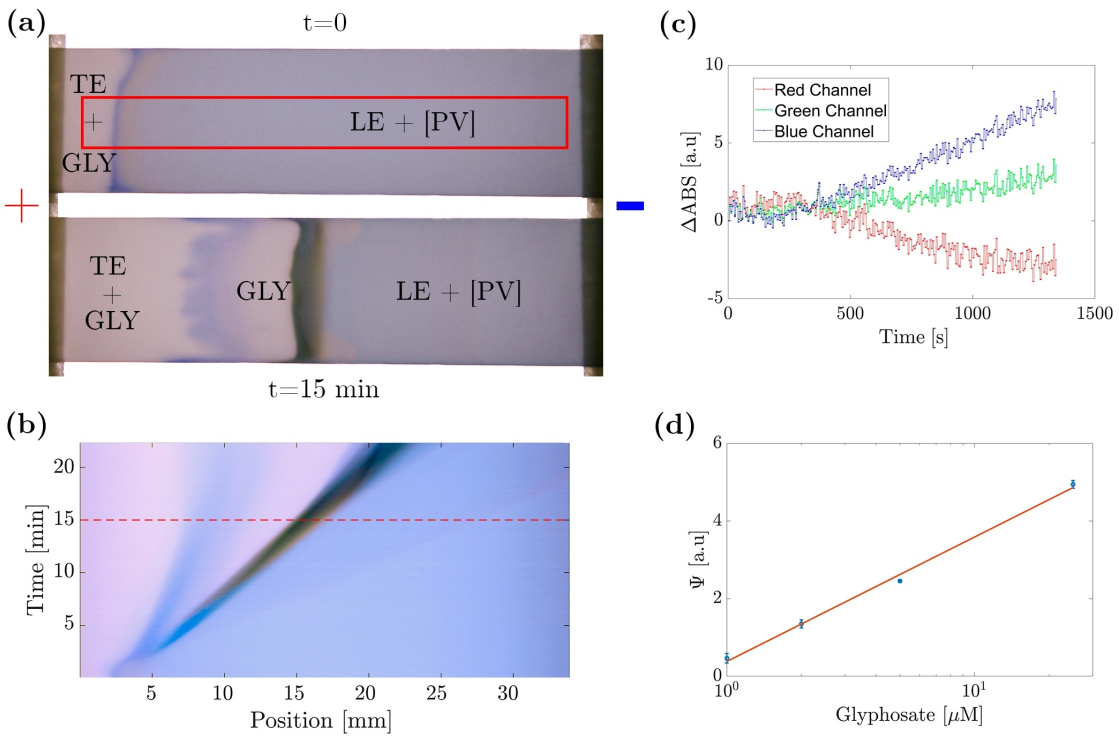

Figure D.7: Results of GLY detection with an e-µPAD by ITP technique with colorimetric detection. **(a)** Initial and 15-minute photographs with the analysis area marked in red. **(b)** Time-space matrix showing the system's dynamics. The dotted line contains information from the vertically averaged photograph (a), at t=15 min **(c)** ΔABS values integrated along the spatial coordinate, for each channel over time. **(d)** Calibration curve for multiple GLY concentrations (1, 2, 5 and 25 µM) of integrated absorption difference index (Ψ).

tive concentration, i.e $\alpha_{[PV]}d = \beta^{RGB}[C]_{[PV]}(t)$, where β^{RGB} represents a variable that depends on the wavelength of the incident light, as measured spectra suggest (see Fig D.2a) and $[C]_{[PV]}(t)$ is the concentration of the [PV] at time t. Applying logarithm and separating the terms yields:

$$log(I(x,t)) = log(I_0(x)) - \alpha_0 d + \beta^{RGB}[C]_{[PV]}(t) \tag{D.2}$$

If the left term of the above equation for a photo at a given time t is subtracted from a photo at the initial time t_0, we find an expression that eliminates the influence of the incident light and simplifies the terms related to nitrocellulose and only depends on the concentrations of the [PV] complex:

$$\Delta ABS^{RGB}(x,t) = log(I(x,0)) - log(I(x,t)) = \beta^{RGB}([C]_{[PV]}(t) - [C]_{[PV]}(0)) \tag{D.3}$$

Given that the [PV] complex preferentially absorbs in the wavelength range corresponding to the red channel of the image and the uncomplexed PV preferentially absorbs in the blue channel (see Fig D.2a), ΔABS^R for the red channel will be directly proportional to the amount of [PV],

and ΔABS^B for the blue channel to the concentration of PV. In the presence of GLY, we will thus observe an increase in ΔABS^B and a decrease in ΔABS^R. In Fig D.7c, the values of ΔABS for each channel integrated along the spatial coordinate are shown as a function of time for a GLY concentration of $5\,\mu$M. It can be seen that after an initial period, ΔABS^R increases linearly, while ΔABS^B decreases consistently. Additionally, it can be noted that the green channel does not show significant changes, which is consistent with the fact that the PV present in the experiment has similar absorption in that wavelength range (see Fig. D.2a). Considering the above, a calibration curve was constructed from an integrated absorption difference index (Ψ), which integrates the difference between absorbance deltas between 0 and t_{ref}: Ψ=$\int_0^{t_{ref}} (\Delta ABS^B - \Delta ABS^R)\, dt$, with a chosen t_{ref} of $900s$. In Fig. D.7d, this index is shown with a point for the average value of all measurements and an error bar for the standard deviation. A linear relationship between the logarithm of GLY concentrations and Ψ was adjusted: $y = 1.24x + 0.38$, $R^2 = 0.996$. The LOD for this technique was $0.8\,\mu$M and the linear range of application was 0.8-25 µM.

D.3.4.3. Validation of the preconcentration

We validated the preconcentration factor of GLY in paper-based ITP in two steps. First, we performed a calibration for GLY concentrations on nitrocellulose. For this, $40\,\mu$L of an aqueous solution of GLY at concentrations of 0.6, 3, 6, 12 and $30\,\mu$M were dropped on sheets of nitrocellulose (10 mm x 10 mm) and the solution was allowed to dry at ambient conditions. Glyphosate was then extracted by inserting the nitrocellulose sheets into a microreaction vial with $250\,\mu$L of an aqueous solution of 37 mM H_3PO_3 and 112 mM NaOH. The extraction was accomplished under sonication for 1 hour. Quantification was achieved using CE-MS (see Section D.2.3) [Wimmer et al., 2022]. Extracted concentrations of GLY were determined using the isotope-labelled GLY standard glyphosate-2-^{13}C (≥99.9%, Sigma Aldrich, Steinheim Germany) added to the vial after extraction and before CE-MS measurements at a concentration of $6\,\mu$M. Comparing the concentrations of the GLY extracted from the nitrocellulose with the concentration of the internal standard, we see a slope of 0.5 for the regression line, indicating an extraction efficiency of about 50% (see Fig. D.8a). Finally, a paper-based ITP experiment on nitrocellulose was conducted as before with a GLY concentration of $1\,\mu$M in the reservoir, but without using PVP to avoid impairments of extraction or downstream CE-MS analysis. After the ITP separation was complete, the paper strip was uniformly cut into 5 segments of about 10 mm length excluding the sections immersed in the reservoirs (see inset in Fig. D.8b). Each segment was analyzed for GLY by CE-MS using the internal standard. Afterwards, the extracts for each paper zone and also the standard (in the same way as described above) were analyzed by CE-MS with the electropherograms shown in Fig. D.8b.

We estimated a preconcentration factor by comparison with the internal standard. For the zone in the centre of the nitrocellulose strip, Zone III, the highest peak area was obtained with a ratio of ∼15 between GLY and the internal standard indicating a concentration of (15*6)=90 µM. With the extraction efficiency of 50%, a preconcentration factor of 180 was calculated for the starting concentration of GLY of 1 µM. This factor is not fully comparable to the one in the ITP experiment, as the effective preconcentration factor at the GLY front visible by colorimetric detection can be expected to reach considerably higher local values.

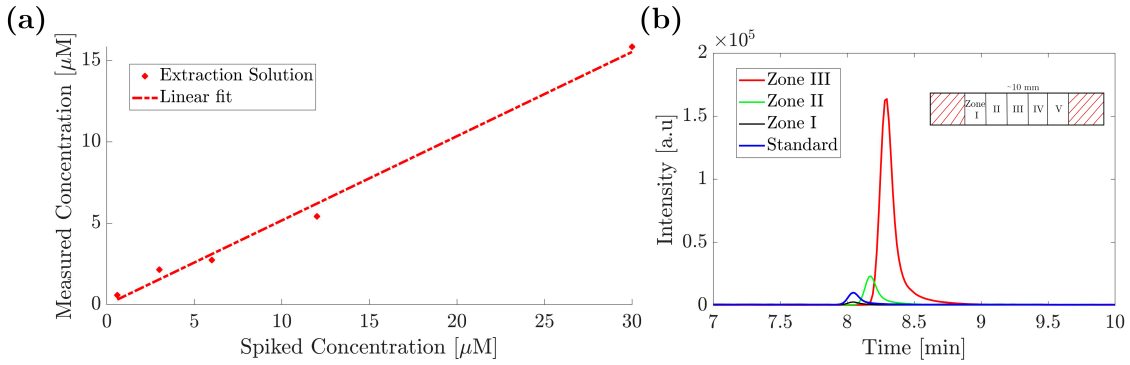

Figure D.8: Results of the validation of the preconcentration: **(a)** Calibration of the extraction solution with an efficiency of ∼ 50% **(b)** Nitrocellulose zones analyzed by CE-MS with a preconcentration factor of 180 for GLY in paper-based ITP.

D.4. Conclusions

Our study demonstrates that with a simple electrophoretic microfluidic paper-based device using ITP, preconcentration factors of up to 820 can be expected from simulation results and meet the requirements such as pH and effective electrophoretic mobilities of reaction partners in colorimetric detection.A preconcentration factor of about 180 was determined by offline analysis in segments of the nitrocellulose strips after ITP analysis. The instrumental setup was a simple 3D-printed device with two electrode chambers and filter paper, here we used nitrocellulose to reduce sorption of the analyte GLY and decomposition of the colorimetric complex of pyrocatechol violet and copper ions. The electrophoretic mobilities and starting conditions were chosen to have preconcentrated GLY in the terminating electrolyte migrating to a zone of the blue [PV] complex to evoke a demetallation and the formation of yellow free PV. A simple camera followed the color change. Our new evaluation method proved very efficient using the RGB channels of the images. With this, a calibration curve was obtained with a relatively wide linear range from 0.8 to 25 µM. Using the lower limit as an estimate for the LOD, it is clear that environmental monitoring is not yet possible with concentrations often below 1 µg L^{-1} (<6 nM) [Schwientek et al., 2024]. Further optimization is required to preconcentrate GLY from an even larger reservoir or prolong the

preconcentration times.

Our method seems promising to detect GLY in herbicide formulations and for visualizing spray drift, though the current detection limits are not yet adequate for surface water analysis. Isotachophoretic preconcentration provides the advantage of separating interfering compounds with different electrophoretic mobilities from GLY, such as glycine and certain carboxylic acids. Future research will explore potential matrix effects, including the influence of ionic strength and complexing agents like EDTA or humic acids, which may competitively complex copper ions. Additionally, the device can be adapted for other applications, such as analyzing GLY in (old) formulations in developing countries, where sales and applications are hardly regulated [Oltramare et al., 2022], or for detecting other ionic analytes and simplified copper analysis.

Acknowledgments

This work was supported by a scholarship of the Division of Analytical Chemistry of the Gesellschaft Deutscher Chemiker (GDCh), German Research Foundation [grant number 507290570], CONICET [grant number PIP-2020-1049], Agencia I+D+i [grant number PICT-2021-0651], UNL [grant number CAI+D 2020] and UTN [grant numbers PID8685, PID100015], Argentina.

Author contribution statement

Nicolás Franck: Conceptualization, Methodology, Formal analysis and investigation, Writing - original draft preparation, Writing - Review & Editing, Visualization. **Pascal Stopper**: Methodology, Formal analysis and investigation, Writing - Review & Editing. **Lukas Ude**: Methodology, Formal analysis and investigation, Writing - Review & Editing. **Raul Urteaga**: Methodology, Formal analysis and investigation, Writing - Review & Editing, Funding acquisition, Resources. **Pablo A. Kler**: Conceptualization, Formal analysis and investigation, Writing - Review & Editing, Funding acquisition, Resources. **Carolin Huhn**: Conceptualization, Methodology, Formal analysis and investigation, Writing - Review & Editing, Funding acquisition, Resources, Supervision.

Conflicts of interest

The authors declare no financial/commercial or academic conflict of interest.

Suplementary Information

The online version of this paper includes a video. Such video summarizes a complete ITP experiment on paper, first filling the nitrocellulose strip with the blue [PV] + LE complex from the cathode (right) and then with TE + GLY from the anode (left). A concentration of 5 µM of GLY aqueous solution was used. 400 V were then applied between the electrodes. The photos that make up the video were taken every 5 s and the video is at 24 fps. It can be found on the website of the journal.

References

C. M. Benbrook. Trends in glyphosate herbicide use in the United States and globally. *Environmental Sciences Europe*, 28(3), Feb. 2016. ISSN 2190-4715. doi: 10.1186/s12302-016-0070-0. URL http://dx.doi.org/10.1186/s12302-016-0070-0.

A. V. Bruggen, M. He, K. Shin, V. Mai, K. Jeong, M. Finckh, and J. Morris. Environmental and health effects of the herbicide glyphosate. *Science of The Total Environment*, 616-617:255–268, Mar. 2018. doi: 10.1016/j.scitotenv.2017.10.309. URL https://doi.org/10.1016/j.scitotenv.2017.10.309.

S. M. Damián, F. Schaumburg, and P. A. Kler. Open-source toolbox for electromigrative separations. *Comput Phys Commun*, 237:244–252, 2019. doi: 10.1016/j.cpc.2018.11.015.

P. Daniele. Copper(II) complexes of N-(phosphonomethyl)glycine in aqueous solution: a thermodynamic and spectrophotometric study. *Talanta*, 45(2):425–431, Dec. 1997. ISSN 0039-9140. doi: 10.1016/s0039-9140(97)00156-2. URL http://dx.doi.org/10.1016/S0039-9140(97)00156-2.

S. Q. de Aguiar Filho, A. M. F. Costa, A. K. dos Santos Pereira, G. S. Cavallini, and D. H. Pereira. Interaction of glyphosate in matrices of cellulose and diethylaminoethyl cellulose biopolymers: theoretical viewpoint of the adsorption process. *Journal of Molecular Modeling*, 27(9), Sept. 2021. ISSN 0948-5023. doi: 10.1007/s00894-021-04894-y. URL http://dx.doi.org/10.1007/s00894-021-04894-y.

M. A. Ewing and A. D. Robson. The use of MES buffer in early nodulation studies with annual Medicago species. *Plant and Soil*, 131(2):199–206, Mar. 1991. ISSN 1573-5036. doi: 10.1007/bf00009449. URL http://dx.doi.org/10.1007/BF00009449.

F. T. Ferreira, K. A. Catalão, R. B. Mesquita, and A. O. Rangel. New microfluidic paper-based analytical device for iron determination in urine samples. *Analytical and Bioanalytical Chemistry*, 413:7463–7472, 2021. doi: 10.1007/s00216-021-03706-9.

N. Franck, F. Schaumburg, P. A. Kler, and R. Urteaga. Precise electroosmotic flow measurements on paper substrates. *Electrophoresis*, 42(7–8):975–982, Jan. 2021. ISSN 1522-2683. doi: 10.1002/elps.202000271. URL http://dx.doi.org/10.1002/elps.202000271.

N. Franck, C. L. A. Berli, P. A. Kler, and R. Urteaga. Multiphysics approach for fluid and charge transport in paper-based microfluidics. *Microfluidics and Nanofluidics*, 26(11), Oct. 2022. ISSN 1613-4990. doi: 10.1007/s10404-022-02590-8. URL http://dx.doi.org/10.1007/s10404-022-02590-8.

N. Franck, L. Vera Candioti, G. S. Gerlero, R. Urteaga, and P. A. Kler. A simple method for the assessment of electrophoretic mobility in porous media. *Electrophoresis*, 45(7–8):589–598, Oct. 2023. ISSN 1522-2683. doi: 10.1002/elps.202300180. URL http://dx.doi.org/10.1002/elps.202300180.

B. Gaš. Peakmaster and Simul – Software tools for mastering electrophoresis. *TrAC Trends in Analytical Chemistry*, 165:117134, Aug. 2023. ISSN 0165-9936. doi: 10.1016/j.trac.2023.117134. URL http://dx.doi.org/10.1016/j.trac.2023.117134.

G. S. Gerlero, S. Márquez Damián, and P. A. Kler. electromicrotransport v2107: Open-source toolbox for paper-based electromigrative separations. *Computer Physics Communications*, 269:108143, Dec. 2021. ISSN 0010-4655. doi: 10.1016/j.cpc.2021.108143. URL http://dx.doi.org/10.1016/j.cpc.2021.108143.

J. P. K. Gill, N. Sethi, A. Mohan, S. Datta, and M. Girdhar. Glyphosate toxicity for animals. *Environmental Chemistry Letters*, 16(2):401–426, Dec. 2017. doi: 10.1007/s10311-017-0689-0. URL https://doi.org/10.1007/s10311-017-0689-0.

H. G. Graf, S. M. Biebl, L. Müller, C. Breitenstein, and C. Huhn. Capillary electrophoresis applied for the determination of acidity constants and limiting electrophoretic mobilities of ionizable herbicides including glyphosate and its metabolites and for their simultaneous separation. *Journal of Separation Science*, 45(5):1128–1139, Jan. 2022. ISSN 1615-9314. doi: 10.1002/jssc.202100952. URL http://dx.doi.org/10.1002/jssc.202100952.

C. Huhn. More and enhanced glyphosate analysis is needed. *Analytical and Bioanalytical Chemistry*, 410(13):3041–3045, Mar. 2018. doi: 10.1007/s00216-018-1000-3. URL https://doi.org/10.1007/s00216-018-1000-3.

T. Kaneta, T. Ueda, K. Hata, and T. Imasaka. Suppression of electroosmotic flow and its application to determination of electrophoretic mobilities in a poly(vinylpyrrolidone)-coated capillary. *Journal of Chromatography A*, 1106(1–2):52–55, Feb. 2006. ISSN 0021-9673. doi: 10.1016/j.chroma.2005.08.062. URL http://dx.doi.org/10.1016/j.chroma.2005.08.062.

A. Kocyła, A. Pomorski, and A. Krężel. Molar absorption coefficients and stability constants of Zincon metal complexes for determination of metal ions and bioinorganic applications. *Journal of Inorganic Biochemistry*, 176:53–65, Nov. 2017. ISSN 0162-0134. doi: 10.1016/j.jinorgbio.2017.08.006. URL http://dx.doi.org/10.1016/j.jinorgbio.2017.08.006.

H. E. L. Madsen, H. H. Christensen, C. Gottlieb-Petersen, A. F. Andresen, O. Smidsrød, C.-O. Pontchour, P. Phavanantha, S. Pramatus, B. N. Cyvin, and S. J. Cyvin. Stability constants of copper(II), zinc, manganese(ii), calcium, and magnesium complexes of N-(phosphonomethyl)glycine (glyphosate). *Acta Chemica Scandinavica*, 32a:79–83, 1978. ISSN 0904-213X. doi: 10.3891/acta.chem.scand.32a-0079. URL http://dx.doi.org/10.3891/acta.chem.scand.32a-0079.

Z. Malá and P. Gebauer. Recent progress in analytical capillary isotachophoresis. *Electrophoresis*, 40(1):55–64, Aug. 2018. ISSN 1522-2683. doi: 10.1002/elps.201800239. URL http://dx.doi.org/10.1002/elps.201800239.

Z. Malá and P. Gebauer. Analytical isotachophoresis 1967–2022: From standard analytical technique to universal on-line concentration tool. *TrAC Trends in Analytical Chemistry*, 158:116837, Jan. 2023. ISSN 0165-9936. doi: 10.1016/j.trac.2022.116837. URL http://dx.doi.org/10.1016/j.trac.2022.116837.

B. Y. Moghadam, K. T. Connelly, and J. D. Posner. Isotachophoretic preconcenetration on paper-based microfluidic devices. *Analytical Chemistry*, 86(12):5829–5837, May 2014. doi: 10.1021/ac500780w. URL https://doi.org/10.1021/ac500780w.

E. W. Nery and L. T. Kubota. Sensing approaches on paper-based devices: a review. *Analytical and Bioanalytical Chemistry*, 405(24):7573–7595, Apr. 2013. ISSN 1618-2650. doi: 10.1007/s00216-013-6911-4. URL http://dx.doi.org/10.1007/s00216-013-6911-4.

J.-C. Niu, T. Zhou, L.-L. Niu, Z.-S. Xie, F. Fang, F.-Q. Yang, and Z.-Y. Wu. Simultaneous pre-concentration and separation on simple paper-based analytical device for protein analysis. *Analytical and Bioanalytical Chemistry*, 410(6):1689–1695, Jan. 2018. ISSN 1618-2650. doi: 10.1007/s00216-017-0809-5. URL http://dx.doi.org/10.1007/s00216-017-0809-5.

E. Okada, T. Coggan, T. Anumol, B. Clarke, and G. Allinson. A simple and rapid direct injection method for the determination of glyphosate and AMPA in environmental water samples. *Analytical and Bioanalytical Chemistry*, 411(3):715–724, Dec. 2018. doi: 10.1007/s00216-018-1490-z. URL https://doi.org/10.1007/s00216-018-1490-z.

C. Oltramare, F. T. Weiss, P. Staudacher, O. Kibirango, A. Atuhaire, and C. Stamm. Pesticides monitoring in surface water of a subsistence agricultural catchment in Uganda using passive samplers. *Environmental Science and Pollution Research*, 30(4):10312–10328, Sept. 2022. ISSN 1614-7499. doi: 10.1007/s11356-022-22717-2. URL http://dx.doi.org/10.1007/s11356-022-22717-2.

J. V. Pagaduan, V. Sahore, and A. T. Woolley. Applications of microfluidics and microchip electrophoresis for potential clinical biomarker analysis. *Analytical and Bioanalytical Chemistry*, 407(23):6911–6922, Apr. 2015. ISSN 1618-2650. doi: 10.1007/s00216-015-8622-5. URL http://dx.doi.org/10.1007/s00216-015-8622-5.

K. Popov, H. Rönkkömäki, and L. H. J. Lajunen. Critical evaluation of stability constants of phosphonic acids (IUPAC Technical Report). *Pure and Applied Chemistry*, 73(10):1641–1677, Oct. 2001. ISSN 0033-4545. doi: 10.1351/pac200173101641. URL http://dx.doi.org/10.1351/pac200173101641.

A. Ramachandran and J. G. Santiago. Isotachophoresis: Theory and microfluidic applications. *Chemical Reviews*, 122(15):12904–12976, June 2022. doi: 10.1021/acs.chemrev.1c00640. URL https://doi.org/10.1021/acs.chemrev.1c00640.

G. I. Salentijn, M. Grajewski, and E. Verpoorte. Reinventing (bio) chemical analysis with paper. *Analytical Chemistry*, 90(23):13815–13825, 2018. doi: 10.1021/acs.analchem.8b04825.

F. Schaumburg and C. L. Berli. Assessing the rapid flow in multilayer paper-based microfluidic devices. *Microfluid Nanofluid*, 23(8):1–10, 2019. doi: 10.1007/s10404-019-2265-3.

F. Schaumburg, P. A. Kler, C. S. Carrell, C. L. Berli, and C. S. Henry. USB powered microfluidic paper-based analytical devices. *Electrophoresis*, 41(7-8):562–569, 2020. doi: 10.1002/elps.201900273.

F. Schaumburg, J. P. Vidocevich, G. S. Gerlero, N. Pujato, J. Macagno, P. A. Kler, and C. L. A. Berli. A free customizable tool for easy integration of microfluidics and smartphones. *Scientific Reports*, 12(1), May 2022. doi: 10.1038/s41598-022-13099-z. URL https://doi.org/10.1038/s41598-022-13099-z.

M. Schwientek, H. Rügner, S. Haderlein, W. Schulz, B. Wimmer, L. Engelbart, S. Bieger, and C. Huhn. Glyphosate contamination in European rivers not from herbicide application? Preprint (Version 3) available at Research Square, June 2024. URL http://dx.doi.org/10.21203/rs.3.rs-3917957/v3.

M. Sokołowska and W. Bal. Cu(II) complexation by "non-coordinating" N-2-hydroxyethylpiperazine-N-2-ethanesulfonic acid (HEPES buffer)□. *Journal of Inorganic Biochemistry*, 99(8):1653–1660, Aug. 2005. ISSN 0162-0134. doi: 10.1016/j.jinorgbio.2005.05.007. URL http://dx.doi.org/10.1016/j.jinorgbio.2005.05.007.

J. C. Ulrich and P. L. Ferguson. Development of a sensitive direct injection LC-MS/MS method for the detection of glyphosate and aminomethylphosphonic acid (ampa) in hard waters. *Analytical and Bioanalytical Chemistry*, 413:3763–3774, 2021. doi: 10.1007/s00216-021-03324-5.

A. L. Valle, F. C. C. Mello, R. P. Alves-Balvedi, L. P. Rodrigues, and L. R. Goulart. Glyphosate detection: methods, needs and challenges. *Environmental Chemistry Letters*, 17(1):291–317, Sept. 2018. ISSN 1610-3661. doi: 10.1007/s10311-018-0789-5. URL http://dx.doi.org/10.1007/s10311-018-0789-5.

P. Wei, L. Xiao, P. Hou, Q. Wang, and P. Wang. A novel Cu(II)-assisted peptide fluorescent probe for highly sensitive detection of glyphosate in real samples: real application in test strips and smartphone. *Analytical and Bioanalytical Chemistry*, 415(24):5985–5996, July 2023. doi: 10.1007/s00216-023-04869-3. URL https://doi.org/10.1007/s00216-023-04869-3.

B. Wimmer, H. Neidhardt, M. Schwientek, S. B. Haderlein, and C. Huhn. Phosphate addition enhances alkaline extraction of glyphosate from highly sorptive soils and aquatic sediments. *Pest Management Science*, 78(6):2550–2559, Apr. 2022. ISSN 1526-4998. doi: 10.1002/ps.6883. URL http://dx.doi.org/10.1002/ps.6883.

B. C. Wimmer B. and H. C. Alternative Wege in der Glyphosatanalytik. *GIT Labor-Fachzeitschrift*, 4(66):28, June 2022. ISSN 0016-3538. URL https://analyticalscience.wiley.com/content/magazine-do/wiley-analytical-science-magazine---june-2022.

P. Yadav and F. Zelder. Detection of glyphosate with a copper(II)-pyrocatechol violet based GlyPKit. *Analytical Methods*, 13(38):4354–4360, 2021. doi: 10.1039/d1ay01168e. URL https://doi.org/10.1039/d1ay01168e.

W. Zheng, K. Wang, H. Xu, C. Zheng, B. Cao, Q. Qin, Q. Jin, and D. Cui. Strategies for the detection of target analytes using microfluidic paper-based analytical devices. *Analytical and Bio-*

analytical Chemistry, 413(9):2429–2445, Mar. 2021. doi: 10.1007/s00216-021-03213-x. URL https://doi.org/10.1007/s00216-021-03213-x.

Doctorado en Ingeniería
mención Mecánica computacional

Título de la obra:

Desarrollo de dispositivos electroforéticos basados en papel para análisis cuantitativos

Autor: Nicolás Franck

Lugar: Santa Fe, Argentina

Palabras Claves:

microfluídica en papel, electroforesis, simulaciones numéricas, medios porosos, flujo electroosmótico, isotacoforesis, movilidad electroforética, OpenFOAM, caracterización experimental, mecánica computacional